Università degli studi di Padova
Facoltà di Ingegneria

MCCXXII

Aalto University
School of Electrical Engineering

Corso di Laurea Magistrale in Ingegneria Elettronica

Reduction of light-induced degradation caused by copper contamination in silicon solar cells

Relatore:
Prof. Roberta Bertani

Controrelatore:
Prof. Andrea Cester

Host university supervisor:
Docent D.Sc. Hele Savin

Assistant supervisor:
D.Sc. Yacine Boulfrad

Presentata da:
Alessandro Inglese

Anno Accademico 2012-2013

Aalto University
School of Electrical Engineering

ABSTRACT OF
MASTER'S THESIS

Author: Alessandro Inglese
Title: Reduction of light-induced degradation caused by copper contamination in silicon solar cells

Date: September 20, 2012

Supervisor(home university): Prof.Roberta Bertani
Supervisor(host university): Docent D.Sc.Hele Savin
Instructor(host university): D.Sc. Yacine Boulfrad

Pages: x+120

Abstract: Copper is widely known as a metal with very good physical and electrical characteristics. The main disadvantage that has strongly limited its use for the deposition of the metal contact in silicon solar cells is represented by its high diffusivity in the silicon bulks. Several studies revealed that defects introduced by copper diffusion, as well as other latent complexes, are activated by the incident light causing the formation of traps and recombination centres in the band gap that strongly affect the performance of the solar cell in terms of efficiency and long-term reliability.

The purpose of this thesis is to study this phenomenon of light-induced degradation and investigate the effectiveness of a method consisting of the deposition of a certain amount of negative charge on both surface sides of the wafer in order to attract positively charged interstitial copper towards the surface. Several experiments were carried out on samples provided by two different suppliers varying various parameters, such as the amount of charge, the thickness and the material of the passivation layer. The results clearly showed that negative charge provided beneficial effects on suppression of the light-induced degradation phenomenon. Moreover some publications revealed that, after the degradation, the initial performance can be recovered by means of an annealing step. These experiments also showed that the presence of this charge strongly influences the effectiveness of this recovery procedure.

Keywords:
Silicon solar cells, copper contamination, LID, Lifetime measurement, Aluminum-oxide passivation, boron-oxygen complexes, Herguth method

Language: English

Autore: Alessandro Inglese
Titolo:
Reduction of light-induced degradation caused by copper contamination in silicon solar cells

Data: 20 Settembre 2012

Relatore: Prof.Roberta Bertani
Relatore(universitá ospitante): Docent D.Sc.Hele Savin
Correlatore(universitá ospitante): D.Sc. Yacine Boulfrad

Pagine: x+120

Sommario:

Il rame é un metallo comunemente conosciuto per le sue ottime proprietá elettriche e fisiche. Il principale svantaggio che ha fortemente limitato il suo utilizzo per la deposizione dei contatti metallici sulle celle solari é rappresentato dalla sua elevata diffusivitá nel substrato di silicio.
Diversi studi hanno mostrato che i difetti introdotti dal rame, cosí come altri gruppi latenti, vengono attivati dalla luce solare incidente causando la formazione di trappole e centri di ricombinazione nel *band-gap* del semiconduttore e portando ad una forte riduzione delle prestazioni della cella solare in termini di efficienza complessiva e di affidabilitá a lungo termine.
Lo scopo di questa tesi é di studiare il fenomeno di degradazione alla luce solare e analizzare l'efficacia di un metodo che consiste nella deposizione di un fissata quantitá di carica su entrambi le superfici del wafer in modo da attrarre verso la superficie gli ioni interstiziali di rame caricati positivamente. Diversi esperimenti sono stati eseguiti variando numerosi parametri, tra cui la quantitá di carica, lo spessore e il materiale dello strato di passivazione. I risultati hanno chiaramente mostrato che la presenza di questa carica negativa produce effetti benefici sulla riduzione del fenomeno di degradazione. Inoltre alcune pubblicazioni hanno riportato che in seguito alla degradazione le prestazioni iniziali della cella solare possono essere recuperate mediante una breve fase di annealing. Gli esperimenti riportati in questa tesi hanno anche evidenziato che la presenza di questa carica superficiale influenza notevolmente l'efficacia di questa procedura di *recovery.*

Parole chiave:

Silicon solar cells, copper contamination, LID, Lifetime measurement, Aluminum-oxide passivation, boron-oxygen complexes, Herguth's method

Lingua: Inglese
Note:
Questo lavoro di tesi é stato eseguito presso i laboratori di Micronova(Centre for micro- and nanotechnology, Espoo, Finlandia) nel periodo compreso tra Febbraio 2012 e Ottobre 2012 nell'ambito del programma LLP-Erasmus.

Preface

The present thesis is submitted as fulfillment of the prerequisites for obtaining the M.Sc. in Electronic Engineering(Ingeneria Elettronica) at the University of Padova, Italy (Universitaá degli Studi di Padova). The experimental activity included in this thesis was carried out at Aalto University, particularly at Micronova(centre for Micro and Nanotechnology) located in Otaniemi(Espoo, Finland) under the supervision of D.Sc. Hele Savin and Roberta Bertani, professor of Chemistry at the Department of Chemical processes of the University of Padova.

First of all I would like to thank my supervisor Docent Hele Savin for giving me the opportunity to work in the *Electron physics* research group. Furthermore my deep gratitude goes to my instructor, Dr.Yacine Boulfrad for his willingness and for his fundamental support. I wish also to thank all the members of the group for their direct and indirect help.

A special acknowledgement goes to my family, Francesca, Arianna and Riccardo, who helped me throughout my studies...really thanks!Without their support, I would have never reached this goal.

I wish to thank Ville and Virginio who participated actively in the awesome discussions of room 4154, also called *the Lounge.* Thanks also to Heidi, Elsa, Lotta and Evi who, unbeknown to them, gave us nice discussion topics during our recreational time in *the Lounge.*

Finally I want to thank my bestfriends Gloria, Marco, Gabriele, Alessio, Michael and Maria Chiara who are anxiously waiting for my return to the hometown. Be patient!

Espoo, September 2012
Alessandro Inglese

Contents

Introduction and Thesis overview

Nowadays solar cells are fabricated with silver contacts; unfortunately silver is a very expensive material and it has a very strong impact on the final price of the solar panel. In order to reduce the production costs, the replacement of silver with copper represents one of the most promising solutions, since copper is widely known as a metal with very good electrical and physical characteristics. Furthermore copper metal contacts result to be extremely thin, so that the loss of efficiency due to the deposition of metal fingers on the top of every single cell is considerably reduced. The image below shows the cost per watt of silver metal contacts compared to copper ones.

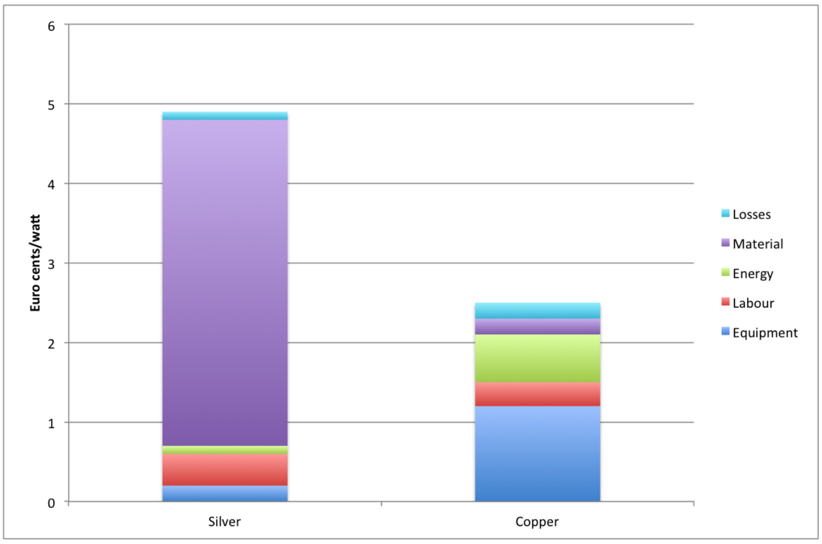

Figure 1: Cost per watt of silver metallization compared to copper metal contacts; the cost of the equipment for the deposition of copper is compensated by the material[2]

As illustrated by the stacked histogram of figure 1, the cost of the equipment and energy with copper metallization is higher than the counterparts with silver but these costs are more than compensated by the material; copper results about one hundred times cheaper than silver so that the final price of copper metallization results to be 2.4 eurocents/watt, whereas the average cost of silver metallization is

around 5 eurocents/watt. Thus the use of copper metal contacts allows the reduction of the final cost up to one half compared to silver counterparts. Furthermore copper represents the best choice in terms of physical characteristics, performance and reliability thanks to the absence of many parasitic phenomena(e.g. electromigration that will be briefly presented further on). However the very low cost of the material is undoubtedly the most interesting characteristic that attracted the photovoltaic research.
This thesis work is primarily related to the realization of copper contacts on silicon solar cells in order to reduce the fabrication costs and improve at the same time the conversion efficiency.

The first commercially available solar cell with copper metal contacts was presented in October 2011[1]; it was fabricated on monocrytalline silicon and it showed very good performances in terms of reliability and conversion efficiency.
The main disadvantage that has strongly limited the usage of copper in the metal contacts is due to its high diffusivity in the semiconductor; as a matter of fact, the diffusion of copper causes the creation of traps and recombination centres that limit appreciably the capability of extracting electron-holes couples. Thus the improvement of the series resistance by using copper metal contacts is compensated by the introduction of these defects in the silicon bulk. In order to reduce the contamination introduced by copper, research has been focussing on the testing of new materials that should act as barriers for the copper diffusion into the silicon substrates. A review on the state-of-art of these barrier materials that should reduce copper diffusion will be presented in chapter 3.
The detrimental effect of copper on the performance of the solar cells can be avoided employing different approaches; the present experimental work will investigate the role of copper on the performance of solar cells and the various techniques aimed at the reduction of its negative impact on the base of some experimental results.

Chapter 1

Solar cells

A solar cell (also called photovoltaic cell or photoelectric cell) is an electrical device which is able to convert the energy of solar radiation into electrical energy. In order to increase the electrical power, a photovoltaic panel is usually made up of long and complex arrays of solar cells; this chapter will focus primarily on the operation principle of a single silicon solar cell and the most important parameters that define the overall efficiency of a solar cell with a particular stress also on the parasitic phenomena that affect the performance of these devices. Indeed in a solar cell only a small part of the incident radiation can be converted into electrical energy: in the case of monocrystalline silicon the maximum efficiency is usually around 20-21%, 16% with polycrystalline silicon and much below 10% using amorphous silicon. The main reasons at the basis of this low efficiency are principally due to the losses caused by the non-idealities which are inevitably present in every manufactured solar cell. Since this thesis is mainly aimed at improving the efficiency of solar cells, a brief introduction to the operation principle is needed for a complete understanding of the objectives of this work.

1.1 Solar cells: structure and operation principle

A good, although not ideal, realization of the structure of a solar cell is characterized by the presence of a moderately doped p-region(the doping concentration is usually around 10^{15}-10^{16} cm^{-3}) which is sandwiched between a thin highly n-doped layer on the illuminated side and another p-doped layer on the the rear side, as the hole membrane. The basic structure of a solar cell is shown in figure 5.1.

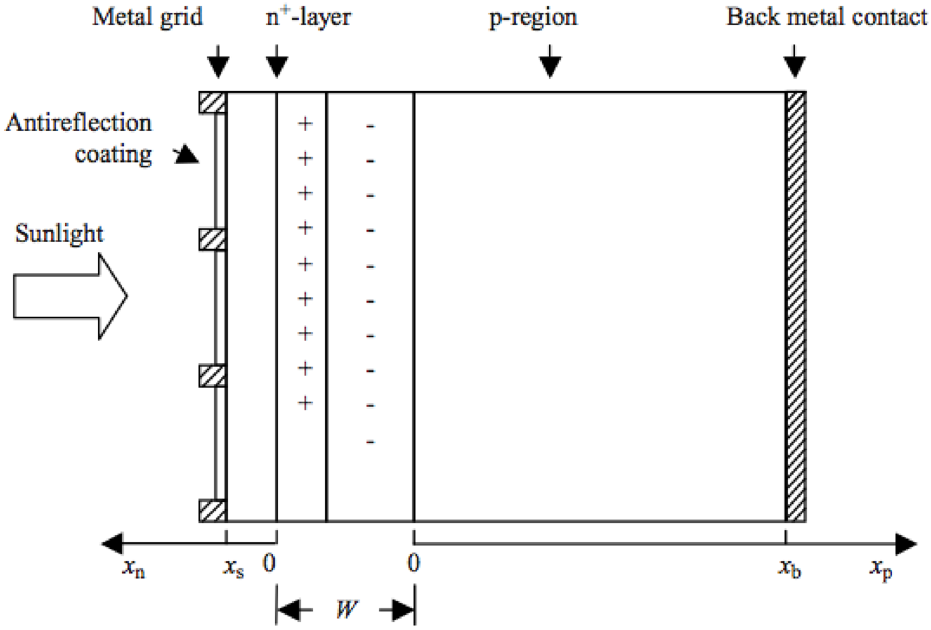

Figure 1.1: Typical structure of a solar cell[3]; note the presence of the p-n junction and the formation of space-charge region

When a p-doped silicon region and a n-region are put together, a depletion region is formed between the two layers, so that the holes in p-region tend to diffuse into the n-region, as well as the electrons in the n-region which move towards the p-region. This movement of electrons and holes causes the generation of a fixed charge in the depletion region, which results to be negative in the p-region and positive in the n-region. These fixed charges generate an electric field which opposes the diffusion of these carriers; in other words, the drift component pulls these carriers in an opposite direction compared to the diffusion component so that a stationary condition, in which the diffusion is perfectly balanced by the drift counterpart, can be reached.

When a photon reaches the depletion region, an electron is promoted to the conduction band forming an electron-hole couple; subsequently the electric field in the depletion region avoids the recombination and pulls the electrons and holes respectively in the n- and p-regions. The potential difference across the depletion region acts as a barrier for the diffusion of both the two charge carriers, as can be seen from the band diagram shown in figure 1.2.

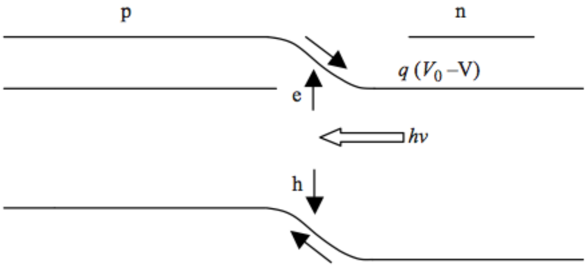

Figure 1.2: Absorption of the incident photon and separation of the electron-hole pair[3] along the p-n junction

If an inversely biased p-n junction is illuminated, the reverse current notably increases because of generation of the electron-hole pairs. Without optical generation, the available electrons and holes that comprise reverse saturation current are thermally generated, resulting in a very low concentration. In forward bias, instead, the reverse current still flows but it is usually smaller than diffusion current. In a solar cell, however, the optically generated current is much larger than diffusion current so that in these conditions the current flow is still dominated by illumination until stronger forward bias conditions are present. The current-voltage diagram is shown in figure 1.3.

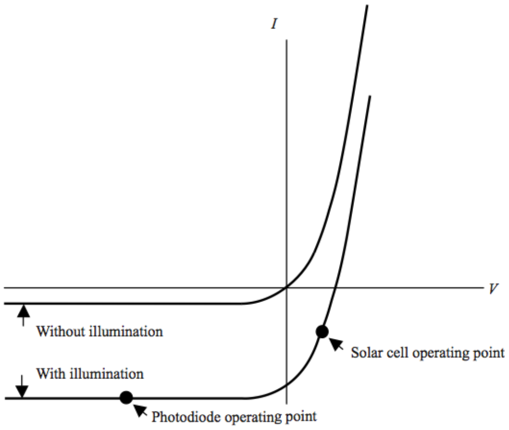

Figure 1.3: Current-Voltage characteristic[3]: in absence of illumination the solar cell behaves as a normal p-n junction; under illumination the photogenerated current causes a downward shift of the curve. The solar cell operating point is the forth quadrant - where the device works as an active component - i.e. a generator

We can notice that the curve representing the operation of the solar cell is shifted downwards compared to the p-n junction. Furthermore the appropriate operating point for a solar cell is always in the forth quadrant of the IV characteristic; under these conditions current flows out of the positive terminal of the p-n junction (p-side). Thus the resulting current flows from the positive terminal towards the negative so that the cell acts as current generator. However at this operating point the current flow is still dominated by optically generated carrier drift rather than by majority carrier diffusion. Although the current-voltage characteristic of a solar cell is the same as that of a photodiode, the operation regions of these two devices are different. Indeed the photodiode usually works in the third quadrant where the junction is inversely biased and it is dominated by photogenerated carriers. On the contrary, in a solar cell the photocurrent is generated in forward direct bias conditions, i.e. when a positive bias is applied to the junction(we have assumed that the positive terminal is on the p-side of the junction).

1.1.1 Equivalent electric circuit

In order to reproduce an electric circuit whose IV characteristic has been presented in figure 1.3, several equivalent models have been developed. As we have already stated in the previous chapter, solar-cells are based on the operation of p-n junctions which represent the basic structure of diodes. Thus the simplest model presents an ideal diode connected to a shunt current generator which accounts for the photogenerated current. However this model does not take into account several parasitic factors which affect quite a lot the performance of the solar cell. In particular both a shunt and series resistance must be included in the model; the series resistance accounts for the non-ideal metallic contacts that always exhibit a finite resistance, while the shunt resistance usually arises from leakage of current through the cell due to manufacturing defects. The current-voltage characteristic calculated so far is based on the assumption that all the carrier generated by illumination are collected by the contacts and transmitted to the load. In real solar cells, however, recombination via impurities in the silicon bulk usually predominate, so that another component must be added to the circuit. The recombination rate is usually expressed through an exponential relation, thus another shunt diode can be added to the circuit introduced before. These three equivalent electric models are sketched in figure 1.4.

The total current flowing on the load is given by the following relation[3]

$$J = J_{sc} - J_1(e^{\frac{q(V+JAR_s)}{kT}} - 1) - \frac{V + JAR_s}{R_{sh}} - J_2(e^{\frac{q(V+JAR_s)}{2kT}} - 1) \qquad (1.1)$$

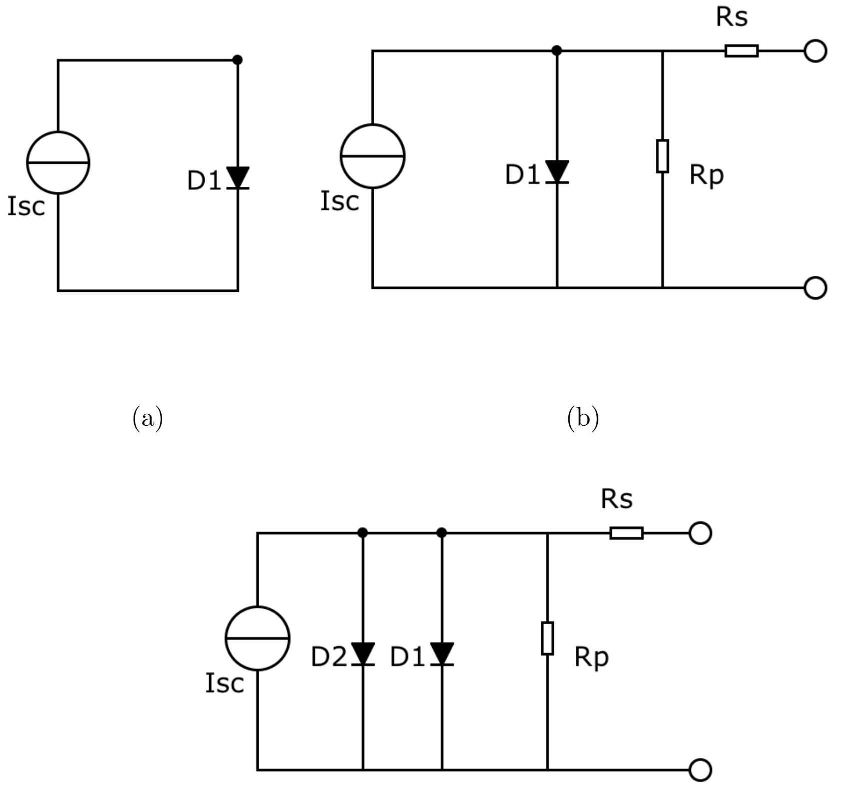

(a) (b)

(c)

Figure 1.4: Equivalent electric circuits: the simplest model is presented in figure a; model b is obtained from model a with the addition of the series resistance(that accounts for the nonideality of the metal contact) and a shunt resistance. Finally the presence of the shunt diode D2 accounts for the recombination of the photogenerated charge through impurities and defects in the substrate

where R_s and R_{sh} represent the parasitic resistance of the equivalent electric model, A indicates the cross sectional area of the device and J_1, J_2 are the saturation currents of the two equivalent diode that were introduced in the model. We can notice that part of the photogenerated current is absorbed by two parasitic shunt diodes of the electric network and the shunt resistance R_p. Note that the equation contains the unknown quantity(the load current J) in both the two sides of the equation, thus an iterative method or alternatively some approximations are usually required to find a solution of the equation.

Consequently we can define several parameters characterising the performance of solar cells. In particular if we consider the circuit sketched in figure 3.13a and we make a short-circuit on the output terminals of the solar cell we can evaluate the photogenerated current I_{sc}. If we take into account the other two models(figure 1.4b and 1.4c) the short-circuit current is the maximum current generated by the solar cell but it does not correspond to the photogenerated current I_{ph}. Moreover if we connect the output terminals of the cell to an infinite impedence, we can ideally measure the open-circuit voltage V_{oc}; again in the simplest model the output voltage is determined exclusively by the drop on diode D1. In more accurate models, the open-circuit voltage is determined also by the voltage drop on resistance R_p, imposed by the current flowing through diodes D1 and D2. Looking at figure 1.3, the short-circuit current can be found on the intercept of the IV curve with the y-axis, while the open-circuit voltage is given by the intersection with the x-axis.

1.1.2 Derivation of the electrical parameters

In order to maximize the output power of the solar cell, the optimal operating conditions V_M and I_M must be evaluated. We can write

$$\frac{d}{dV}P = \frac{d}{dV}[V \cdot I] = 0 \tag{1.2}$$

and find the values of V_M and accordingly I_M to evaluate the maximum output power. Once we have evaluated these optimal working conditions, we can calculate the *fill-factor* defined as follows

$$FF = \frac{V_M I_M}{V_{oc} I_{sc}} \tag{1.3}$$

The meaning of this parameter is well explained by figure 1.5, where we can notice that the rectangle representing the maximum output power is always included in the bigger one, obtained by the product between the short circuit current and the open circuit-voltage(in other words, $FF < 1$).

A solar-cell with a small fill-factor presents a small output power, thus a low conversion efficiency. Particularly the overall efficiency of the cell is defined as follows

$$\eta = \frac{P_{out}}{P_S} = \frac{FF \cdot V_{oc} I_{sc}}{P_S} \tag{1.4}$$

where P_S indicates the solar radiated power. Therefore we can immediately notice from equation 1.4 that a low fill factor reflects directly on the overall efficiency.

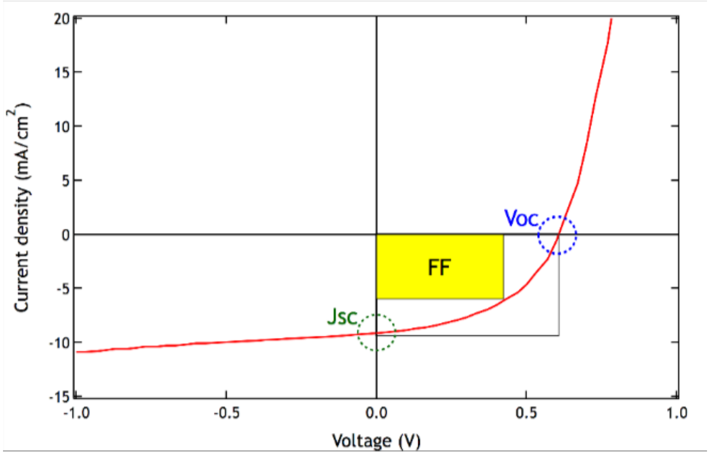

Figure 1.5: Graphical representation of fill-factor: it represents the coverage factor of the yellow rectangle compared to the bigger one obtained by the product between the open-circuit voltage and the short-circuit current

1.1.3 Physical efficiency limitations

1.1.3.1 Effect of parasitic resistances

The series and shunt resistances presented in figure 1.4 affect significantly the efficiency of the solar cell. Therefore the materials which constitute the electric contacts should be good electrical conductors, i.e. they should be able to conduct the charge to the external circuit; perfect conduction means that carriers must not recombine with defects or impurities, and should not give energy to the medium. In other words there should be no resistive loss (no series resistance) or current leakage (shunt resistance) and the material around the junction should be highly conducting and make good ohmic contacts to the external circuit. The effect of the parasitic resistances R_{series} and R_{shunt} on the current-voltage characteristic is shown in figure 1.6. We can immediately notice that both the series and the shunt resistances reduce drastically the fill factor and consequently the overall efficiency. While the shunt resistance is directly related to the design of the pn junction, the series resistance is mainly caused by non-ideal contacts and the finite conductivity of the metallic materials. Thus the reduction of the series resistance is one of the main objectives on which research is currently focussing; nowadays the most widely used material for metal contacts is silver; in order to reduce the power losses at the electric contacts of solar cells, several attempts of replacing silver with other materials represent one of the most promising methods aimed at the reduction of the production costs and the enhancement of the solar cell performance.

It was reported that a solar cell with 18% power conversion efficiency was manufactured with copper backside metallization[1]. Other metallization techniques on silver-free heterojunction silicon solar cells have led the maximum efficiency up to 21%[4]. Along with the improvement of the series resistance through the introduction of copper, other parasitic effects must be taken into account, e.g. the interaction between the metal contact and the underlying substrate. As it will be demonstrated in the next chapters, copper represents one the best candidates for the substitution of silver metal contacts; nevertheless the main issue that has strongly limited its employment in metal contact is due to its high diffusivity into the silicon bulk causing the contamination of the substrate. Therefore the enhancement of the electrical properties of the electric contact must be accompanied by an effective limitation of all the parasitic effects caused by the introduction of these new materials so that the improvement of the electric contacts is not counterbalanced by the worsening of other electrical parameters.

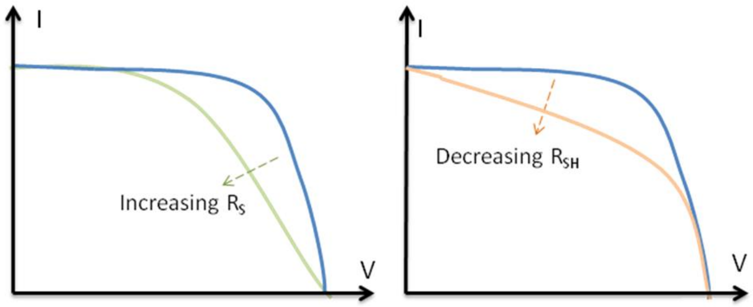

Figure 1.6: Influence of parasitic resistances: the presence of these nonidealites shift downwards the IV curve determining a reduction of the fill-factor - hence of the overall efficiency

1.1.3.2 Semiconductor-Metal contact

Besides the resistivity of the material, metal contacts should also allow an unimpeded charge transport between the solar cell and the external load. A metal is a material with no band gap so that for a metal only the *work function*, which expresses the chemical potential of the material, is usually defined. When a metal and a semiconductor are brought together, two different processes may occur: the formation of a rectifying Schottky junction or an ohmic contact. The formation of a ohmic contact rather than a Schottky contact strongly depends on the energetic position of the Fermi level: if the work function of the semiconductor is higher than that of the metal, the band bending results as sketched in figure 1.7. Thus metals with a small work function usually give rise to good ohmic contacts with n-type semiconductors(see figure 1.7), whereas metals with a large work function make good ohmic contacts with p-semiconductors.

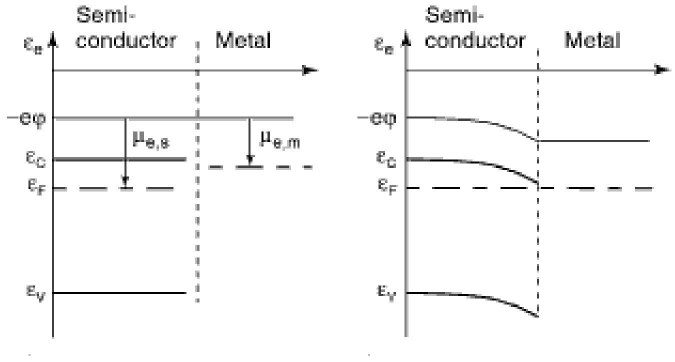

Figure 1.7: The left figure shows the band alignment required for the creation of an ohmic contact where no energetic barrier is formed[3]

Consequently in order to minimize the ohmic parasitic resistance, only few materials result suitable for the formation of a good ohmic contact. The work functions of the most common materials are listed in the table below.

Metal	Work-function
Aluminum	4.28 eV
Gold	5.1 eV
Silver	4.73 eV
Copper	4.75 eV

Table 1.1: Comparison between the work functions of some common metals: copper has quite high work-function which results quite similar compared to silver [3]

We can notice that copper shows a rather high work function, making it suitable with p-type semiconductors. Since solar cells are preferably fabricated starting with p-type substrates, all the metals with a high work function, such as copper, become suitable for the creation of the back contact of the solar cell. Since the solar cell is formed with a p-n junction, two metals with different work functions are usually required in order to ensure a good electric contact(high work function on the p-side and low work function on the n-side).

Contacts with good carrier exchange can also be prepared on the basis of another principle. If the semiconductor is highly doped the depletion layer at surface between the metal and the semiconductor is very thin. Particularly it can be so thin

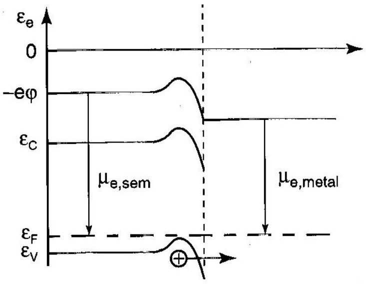

Figure 1.8: Band diagram of a metal-semiconductor junction with a small potential barrier; the thin potential barrier fosters the tunnel effect of the majority carriers at the junction[3]

that the carriers can tunnel through the potential barrier between the semiconductor and the metal; furthermore if we consider that metal usually tends to diffuse into the silicon substrate creating some traps and acceptor states in the semiconductor, that cause a band bending as sketched in figure 1.8.
In a solar cell we have basically two contacts, one exchanging electrons and the other holes; this condition can be fulfilled either by the creation of an ohmic contact for the exchange of majority carriers or an unimpeded flow of the carriers by tunnel effect.

In summary we can conclude that the series resistance of the contact is not dependent only on the intrinsic resistivity of the material but also on the the work function of the material which determines the bending of the bands and the potential barrier encountered by the carriers during the conduction process.

1.1.4 Conclusion

In the previous paragraphs we have seen that the efficiency of a solar solar depends on several factors related to the type of the semiconductor and the quality of the electric contacts. Particularly these factors that influence the performance of the cell can be summarized in few points:

- Crystalline structure of the silicon bulk: the overall efficiency of the solar cell results to be strongly dependent on the inner structure of the substrate(crystalline, multi-crystalline or amorphous).

- Contamination of silicon bulk: the presence of traps and recombination centres affect sensibly the amount of photogenerated charge that can be transferred to the load(see the next chapters).

- Absorption process: in order to improve the efficiency of the cell, the semiconductor should absorb the widest possible spectrum with a low reflection rate of the incident radiation.

- Electric contacts: resistivity of the material and type of electric contact along the junction.
- Shadowing effect: once the single solar-cell has been optimized, the packaging of these cells in a long array becomes one of the main concerns.

This thesis is aimed at reducing the loss of efficiency produced by the metal contact and the contamination of the bulk. These two factor are strictly bound together, since the major drawback related to the use of copper for metallization is represented by the contamination of the underlying substrate.

Chapter 2

Copper metal contacts

Copper has been used in a huge variety of applications for thousands of years; it is a ductile and malleable metal with one of the highest thermal and electrical conductivity. Furthermore it is one of the most common metals in nature, with a natural abundance 60 ppb by weight in the Earth's crust. These characteristics make copper one of the most interesting materials for the conduction of electrical energy. As it was mentioned in the previous chapter, copper tends to diffuse very quickly into the silicon substrate, thus at present it is considered a major insidious impurity in Si devices, unless its contamination level is properly controlled. In the past it was assumed that Cu was similar to other transition metals, so that the critical contamination levels and major defect reactions, established for Fe, Cr, Mn, and Ti, could be applied for Cu as well. Recent studies performed by various groups in the last few years enabled researchers to gain a better understanding of the behavior of Cu in Si and showed how significant is the difference between Cu and other metals in Si. In this chapter we will initially analyse the electronic configuration of copper in silicon substrates; subsequently we will focus primarily on the parasitic effects that affect most of the materials used for the metallization of the electric contacts, such as diffusivity and electromigration, making a comparison between copper and the other metals.

2.1 Physics of copper in silicon

Copper belongs to the group of 3d transition metals, i.e. those elements whose atomic number ranges from 21 to 30. With regard to copper, the atomic number is 29 and in vacuum the electronic structure is as follows

$$^{29}Cu \rightarrow 1s^2 2s^2 2p^6 3s^2 3p^6 3d^9 4s^2 \tag{2.1}$$

Note that copper has an irregular structure because instead of having the $3p^6 3d^9 4s^2$ configuration with an almost full 3d shell, one of the 4s electrons is moved to the 3d shell leaving Cu in an irregular configuration:

$$^{29}Cu \rightarrow 1s^2 2s^2 2p^6 3s^2 3p^6 3d^{10} 4s^1 \tag{2.2}$$

Since a metal atom placed in silicon crystal lattice interacts with the surrounding host atoms, its electron configuration may change compared to its state in vacuum; thus interstitial copper atoms become a single donor in silicon, acquiring an ionized form Cu^+. The presence of a closed shell $3d$ would suggest that the radius of the ion is very small so that it can be considered relatively inactive in the silicon lattice; instead interstitial copper can promote some electrons from 3d into the 4s shell and borrows some electron density from its nearest neighbors. Thus some interactions with the atoms of the lattice are always present so that 3d shell can also be overlapped with the neighbouring Si atoms, giving rise to various complexes, such as Cu silicide(Cu_3Si) whose molecular cell volume results much larger than a single Si atom. In summary the three properties of Cu in silicon: always positive charge state, interaction with silicon lattice and formation of Cu-silicide are the factors that produce the defects in silicon.

2.2 Diffusivity of Copper

Several models have been developed to describe the diffusion of Cu atoms in silicon bulks. A first model was elaborated in 1964 and had been commonly accepted until 1990. Nevertheless studies on the diffusion of copper in heavily $p^+ - Si$ doped wafers stressed the fact that the model did not take into account the effect of pairing of positively charged interstitial copper ions with negatively charged substitutional boron; thus the consequence of this pairing effect is that only a limited fraction of the total Cu concentration is effectively mobile, while the rest is temporarily trapped. Consequently a new model has been developed according

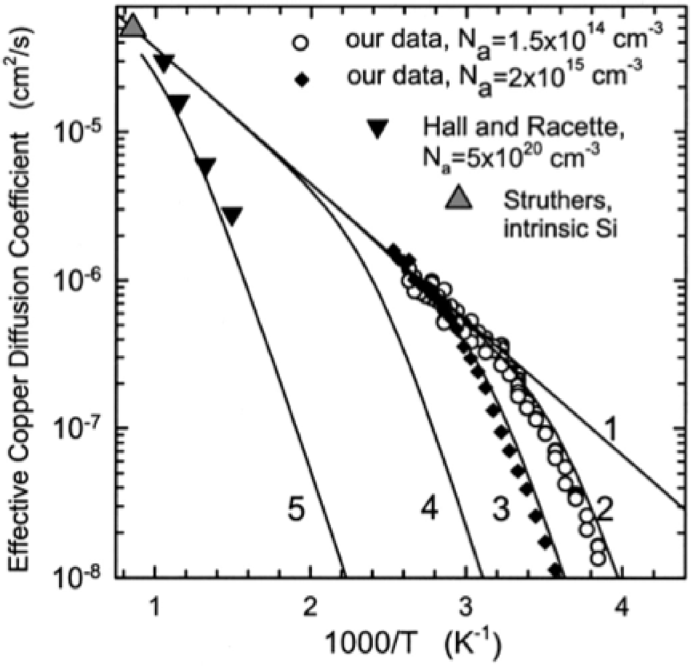

Figure 2.1: Measured diffusion coefficient as a function of temperature and doping; the diamonds show the experimental obtained by Hall and Racette[7] on moderately doped samples whereas the circles represent other experimental results obtained with different doping concentrations; the lines represent the values predicted by eq. 2.3 curve 1. intrinsic silicon; curve 2. $N_a = 1.5 \cdot 10^{14}\ cm^{-3}$; curve 3. $N_a = 2 \cdot 10^{15}\ cm^{-3}$; curve 4. $N_a = 1 \cdot 10^{17}\ cm^{-3}$; curve 5. $N_a = 5 \cdot 10^{20}\ cm^{-3}$[6]

to new experimental results that are illustrated in figure 2.1; we can immediately notice that in the case of intrinsic silicon the relation which expresses the diffusion coefficient as a function of temperature is almost linear; on the contrary as doping increases, the effective diffusion coefficient at low temperatures tends to decrease because of the trapping of Cu atoms with boron ions. Therefore we can also notice that with high doping the curve shifts considerably to the left, so that the diffusion coefficient reduces by several orders of magnitude in respect to intrinsic silicon[6]. An equation that models the effective diffusion coefficient is given as follows

$$D_{eff} = \frac{3 \cdot 10^{-4} \cdot exp(-2090/T)}{1 + 2.584 \cdot 10^{-20} \cdot exp(4990/T) \cdot (N_a/T)} \tag{2.3}$$

Note that equation 2.3 holds only for moderately doped silicon($N_a < 10^{17}\ cm^{-3}$). For intrinsic silicon, the diffusion coefficient becomes

$$D_{int} = 3.0 \cdot 10^{-4} \cdot exp\left(-\frac{0.18eV}{K_b T}\right) \tag{2.4}$$

where the numerator of the fraction included in the argument of the exponential function(0.18 eV) expresses the diffusion barrier which results to be much lower compared to other impurities; the diffusion barrier of some metals, indeed, can be also 0.6-0.7 eV. This low value is primarily due to the small ionic radius of Cu in Si and the weakness of covalent interactions of Cu with the crystal lattice.

As can be seen from equation 2.3, the intrinsic diffusion coefficient in silicon at room temperature is $2.8 \cdot 10^{-7}\frac{cm^2}{s}$, i.e. it implies that copper diffusivity is sufficiently high to enable copper to diffuse significant distances. For example, copper can diffuse at room temperature through a standard 200 μm thick boron-doped silicon wafer in about 15 hours[6].

2.2.1 Diffusion of copper and defects formation

In this paragraph we want to analyse the process that leads to the formation of defects in the silicon bulk after the diffusion of copper atoms. We have already stated that copper usually transforms into an ionized state Cu+; once these ions are formed, they can dissolve and precipitate quickly into the bulk reacting with the silicon lattice and giving rise to different precipitates that can be subdivided into 5 groups(see figure 2.2). These reactions consist of the formation of point defects(see picture A), the formation of copper-silicide agglomerates in the bulk(B), decoration of existing extended defects(e.g dislocations, vacancies, interstitial and substitutional impurities, dislocations)(C), outdiffusion to the surface(D) and segregation to p+-areas(E). It is clear that copper contamination acts in a different way compared to other impurities, e.g. iron or aluminum. For instance it is known that the presence of iron in silicon causes the establishment of stable FeB pairs whose concentration can be determined by means of lifetime measurements. In contrast to the majority of transition metals, instead, the high diffusivity of copper does not allow the formation of electrically active point defects in appreciable densities.

The formation of defect complexes and the diffusion rate of copper atoms is determined by the balance of two opposite reactions, i.e. association and dissociation. In the simplest case, i.e. the formation of point defects(figure 2.2A) with boron substitutional atoms, the kinetic potential barrier that an impurity atom has to overcome to dissociate from a defect is given by the sum of the amount of the diffusion barrier height and the binding energy of the defect complex(analogously to other impurities such as FeB or CuB), so that we can write

$$E_{diss} = E_b + E_d \tag{2.5}$$

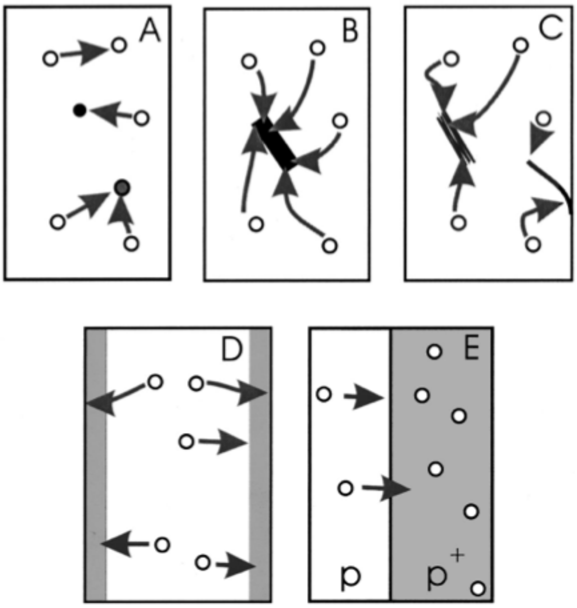

Figure 2.2: Defect reactions of copper[6]: figure a represents the formation of point defects and their complexes; figure b: formation of copper-silicide precipitates in the bulk; figure c:decoration of existing extended defects(dislocations and grain boundaries); figure d: out-diffusion to the surface; figure e: segregation in p+ areas

As already stated, in some common metals the diffusion barrier is much higher than in copper; therefore an estimate for the dissociation energy would be 0.7 eV for CuB pairs and 1.2-1.3 eV for the other metals. Consequently CuB pairs dissociate much faster than the other complexes so that copper atoms cannot be permanently trapped but rather slow down its diffusion until they form agglomerates with a higher bind energy. This explains the reason why copper does not form active CuB point defects in densities higher than 0.1% [9] of its total concentration: the high diffusivity of copper, in fact, enhances the dissociation of its point defects and reduces their stability favouring the diffusion of Cu to thermodynamically sinks. The sinks formed by the diffusion of copper can be extended defects, such as those shown in figure 2.2B and figure 2.2C. However, detailed studies revealed that Cu does not decorate all types of extended defects, but prefers grain boundaries or Frenkel-type dislocations. The effect of lattice strain and electrostatic effects on the precipitation behaviour of copper suggests that preferential Cu precipitation can be associated with either their electrical charge or with local strain fields around them.

The existence of a barrier for nucleation of precipitates is a well-known phenomenon: the driving force, indeed, for precipitation needs to reach a threshold value to start the nucleation and the growth of the precipitates. If the chemical driving force is slightly higher than the nucleation barrier, Cu will form a high density of precipitates in the wafer bulk. Particularly the mathematical equation that binds the chemical driving force and the metal concentration on the wafer surface is as follows

$$\mu = k_B T \cdot ln \left[\frac{C}{C_0(T)} \right] \tag{2.6}$$

where C_0 is the equilibrium solubility of the metal. As soon as a sufficient density of precipitates is formed, the copper concentration on the surface decreases and the value of μ will decrease below the nucleation threshold, so that the diffusion process is stopped. An explanation of the presence of this nucleation barrier can be found if we consider for example the formation of copper silicides(B-type defects in figure 2.2): Cu-silicide complexes, indeed, have a very large molecular volume compared to that of silicon, thus they require the lattice expansion and relaxation. If the energy cost of this lattice strain is higher than the chemical precipitation driving force, no precipitation will occur. Thus it is also clear that the presence of voids, grain boundaries and dislocations in the crystal lattice causes a significant drop of the diffusion barrier(C-type defects in figure 2.2). Out-diffusion process, instead, is the opposite phenomenon that consists of the rejection of copper contaminants towards the surface. An ideal crystal, indeed, tends to repel the impurities that distort its crystal, thus the higher is the silicon crystal quality, the less probable will be the formation of copper agglomerates/precipitates in the bulk and the more likely out-diffusion will be the dominant process. However the process of Cu precipitation is further complicated by the electrostatic interactions between the positively charged interstitial Cu ions and charged precipitates, thus the precipitation barrier could increase if there is an electrostatic repulsion between Cu and the precipitation sites or decrease in the case of electrostatic attraction.

Copper introduced defects, thus, are located in the bandgap and the sign of the net charge corresponding to these defects depends on the position of the Fermi level. Therefore if the defects are positively charged, the electrostatic repulsion between Cu+ defects and positively charged Cu precipitates provides an additional nucleation and precipitation barrier. Another phenomenon that opposes the diffusion of Copper is related to the distortion of the crystal lattice when copper ions diffuse through it. Indeed as already stated, the crystalline structure tends to reject the impurities that distort its lattice.

2.2.1.1 Position of copper introduced defects in the bandgap

In literature some data on the electrical properties of copper related defects have been reported. The defect state levels located at E_c - 0.16 eV and E_c - 0.4 eV have been widely attributed for copper defects in n-type silicon. The level of E_c-0.16 has a small electron capture section σ[1] estimated approximately 3.3 x 10^{-17} cm^2 and has been attributed to interstitial copper. The defect at E_c - 0.4 eV has a large electron capture cross section of $2 \cdot 10^{-15}$ cm^2 and is thought to be a copper precipitate related effect.

The primary copper defect state levels in p-type silicon are four and have been identified as: E_v + 0.1, E_v + 0.22, E_v + 0.44 and E_c - 0.4 eV. Particularly energy levels E_v + 0.44 and E_v + 0.23 act as hole traps and they are are usually associated with extended substitutional defects whose capture cross section results to be $4 \cdot 10^{-16}$ cm^2.[6]

2.2.2 Electromigration phenomenon

One of the main advantages of copper metallization is related to the rejection of the electromigration phenomenon which affects all the devices based primarily on aluminum metallization.

Electromigration is an interconnection reliability problem that can cause the failure of the metal contact after hundreds of hours of successful operation. Particularly electromigration refers to the movement of atoms of the conducting material as a result of momentum exchange between the mobile carriers and the atomic lattice. In practice the movement of electrons and the collision with the atoms of the lattice causes a momentum exchange, thus, as a result, the metal piles up on one side of the electrode, while the opposite side is depleted. This transfer of material causes the formation of voids in the film and a discontinuous interconnection; figure 2.3 shows an ACM image of the effect of Electromigration on an electric contact.

In the picture we can notice that the electromigration has depleted the region to the left and at the same time it has created the accumulation of material on the other region causing the formation of hillocks. The process that leads to the failure of the electric contact can be summarised in few steps: initially the electron flux generates a displacement of the metal atoms; this phenomenon causes the formation of voids first, then the generation of cracks and finally the definitive destruction

---

[1] The capture cross section is an important parameter that defines the effective area of a trap or a recombination center; in practice it is a measure of the effectiveness of the trap and it is directly related to the probability that an electron or a hole is trapped when it traverses the lattice defect. Thus the bigger it is and the higher is the capture probability.

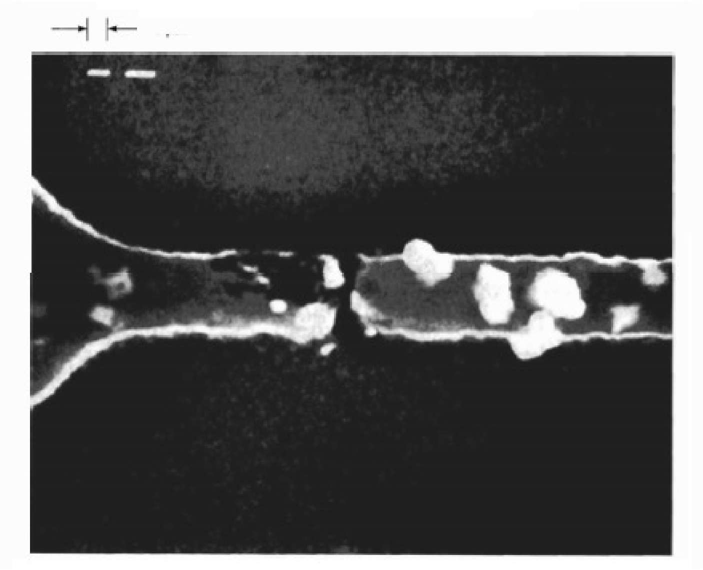

Figure 2.3: Effects of electromigration on an aluminum contact; the image shows the accumulation of material to the left(white hillocks) and the contemporary formation of voids to the right[37]

of the metal contact. Copper metallization is more resistant to electromigration than aluminum counterparts; particularly the rejection to the electromigration phenomenon is usually related to the overall resistivity of the material: indeed the parasitic resistance of the metal is usually due to the lowering of the average drift velocity of the electrons caused by the scattering of the electrons with the metal lattice; when the electrons are pulled by the electric field, the atoms constituting the lattice of the metal act as obstacles for the movement of electrons. This phenomenon increases the resistivity of the metal, leading to an increase of the heat generated by the current flow. Electromigration, as a consequence of a higher resistivity, is therefore one the main factors that restrict the total allowed current flow. A simple mathematical model which leads to a current squared relationship with mass transport is as follows:

$$\frac{1}{MTF} = AJ^2 e^{-\frac{\Phi}{kT}} \tag{2.7}$$

where MTF is the median time to failure expressed in hours, J is the current density, Φ is the activation energy expressed in electronvolts, k is the Boltzmann's constant and T is the temperature in Kelvin. From this mathematical equation we immediately notice that as soon as the current density grows up, the MTF factor shrinks, since its reciprocal must be greater. Moreover the activation energy factor, which accounts for the needed energy for the activation of the electromigration process, is included in the negative argument of the exponential function, thus a decrease of the activation energy implies an increase of the right-hand side of the equation and finally a decrease of the MTF factor. Several experiments showed that the activation energy for electromigration is strongly dependent upon the crystalline structure of the material. Particularly small cristallite aluminum films exhibited an activation energy of 0.48 eV; other well-ordered and large-grained films exhibited an activation energy around 0.9 eV; the increase in activation energy is mainly attributed to the reduction of grain boundaries which represent low energy diffusion paths. In the case of copper a wide range of activation energies have been reported; however the activation energy for copper metallizations usually ranges from 1.1 eV to 1.3 eV, resulting slightly higher than aluminum.

2.3 Why do we choose copper for metallization?

In the previous chapters two important features have been presented: the high diffusivity of copper and its high resistance to electromigration. In practice we have presented either one of the main concerns that has limited the use in the solar cells as front contact material and, on the other hand, a brief description of a feature that makes it one of the most interesting materials for metallization. In addition to electromigration and diffusivity other characteristics must be considered in choosing the metallization material, such as:

- Ability to make good ohmic contacts to p-type substrates;
- Stability in contact with silicon after the cell manufacturing;
- Good Adhesion to both silicon and silicon dioxide;
- Resistance to corrosion by reaction with the environment;
- Low cost compared to gold or silver, as already stated in the previous chapter

Since there is no material that satisfies all these requirements at the same time, a compromise must be found; copper represents one the most interesting alternatives because it meets most of the requirements listed above. Indeed its resistivity is one the lowest among the commonly used materials(only silver resistivity results to be lower than copper) and its rejection to electromigration phenomenon allows a notable improvement of the reliability of metal contact. Moreover the enhanced resistivity of this material reduces the generation of heat when the current flows through the metal contact allowing the conduction of a higher current density without reducing the lifetime and the reliability of the contact.

Furthermore the electrical characteristics of copper are not affected by the different operating conditions so that the behaviour of the material is not altered during the operation of the solar cell; this means that the physical and electrical properties of this material remain substantially stable during the operation of the solar cell. Moreover if we consider also the high melting temperature, the low hardness and the high availability in natural resources, copper represents one of the most interesting materials for the creation metal contacts.

The only disadvantage, that has limited the use of copper thus far, is its high diffusivity into the silicon substrates that causes the formation of traps and recombination centres which reduce the amount of photogenerated electrons. Therefore, the silicon substrate must be protected from the diffusion of copper atoms. This must be accomplished either through preparation of the dielectric layers between the metallization and Si or the deposition of some diffusion barrier. Research on new materials suitable for the creation of these diffusion barriers has been recently carried out. In the next chapter a review on the results achieved using different materials will be presented. Once the diffusion of copper has been successfully limited by the introduction of these barriers, there is still a residual amount of copper, which is represented either by the quantity of copper which is naturally present in the silicon ingot and by the atoms that succeed in overcoming the diffusion barrier. Therefore in the next chapters other techniques for the deactivation of these defects introduced by residual copper will be investigated on the basis of the results of some experiments that were carried out for this purpose.

Chapter 3

Copper diffusion barriers

In order to prevent the diffusion of copper, some barriers made up of inert materials must be deposited on the silicon bulk. Research on new materials has been recently carried out in order to ensure a good performance not only during the operation of the solar cell but also during the fabrication steps. In particular the materials used for the deposition of these barriers must have a high melting point so that even the fastest diffusion mechanism, i.e. grain boundary diffusion, results to be negligible at the typical thermal processes encountered during the fabrication. Numerous materials have been tested, in particular:

- Refractory metals such as chromium, titanium or tungsten
- Ni-based barriers
- W-based barriers
- Co- and TaN- based barriers

The prevention of copper diffusion has become one of the major concerns since copper was introduced in VLSI applications. The introduction of copper metal contacts has recently focussed research not only on the testing of new materials but also on the analysis of the performance on solar cells of those materials that had already been tested for VLSI devices. Recently a solar cell containing a nichel-based copper diffusion barrier was introduced on the market[1] confirming substantially the fact that a material, whose good performance had already been proven in VLSI applications, can also find a successful application in PV devices.

3.1 Barrier failure mechanisms

A barrier is a micro-structure made up of a inert material, which is aimed at preventing the diffusion of materials characterized by a high diffusivity of their atoms. The scaling of this kind of barriers has created several concerns regarding the integrity of these structure in a wide range of temperatures. As a matter of fact the performance of these barriers must be granted also at high temperatures so that copper diffusion is avoided throughout the fabrication process. The main mechanisms that dominate the barrier failure are:

- Diffusion of copper atoms through bulk defects
- Diffusion of copper along grain boundaries
- Loss of the barrier integrity due to chemical reactions with copper atoms

There are two types of defects that contribute significantly to diffusion: vacancy and dislocations. In fact the lack of some atoms constituting the crystal lattice of the material generate some void spaces in which copper atoms can diffuse causing the failure of the barrier. It was experimentally observed that lattice diffusion rates are proportional to the absolute melting temperature of the host material, so that

$$D \sim AT_m \tag{3.1}$$

where A is a proportionality factor depending on a variety of factors, i.e. lattice structure and type of material. However diffusion rates due to atom-vacancy exchange tend to be the slowest diffusion mechanism(thus A should acquire the lowest value), while dissociated dislocations usually exhibit intermediate diffusion rates. On the contrary grain boundaries have the highest diffusion rate representing the main process that causes the failure of the barrier material. Therefore the microstructure of the material plays an important role in the performance of these materials. Particularly film microstructure can be subdivided into several categories: single crystal, polycrystalline, nano-crystalline and amorphous. Figure 3.1 provides a comparison among these categories; generally polycrystalline materials provide the poorest performance, thus they are the least desirable materials for diffusion barrier applications. Particularly the performance results particularly poor when the grain sizes is comparable with the thickness of the film or the film shows a columnar structure. In the latter case grain boundaries extend throughout the film thickness and they are mostly normal to the substrate surface creating an effective pathway for copper diffusion. On the other hand single-crystal diffusion

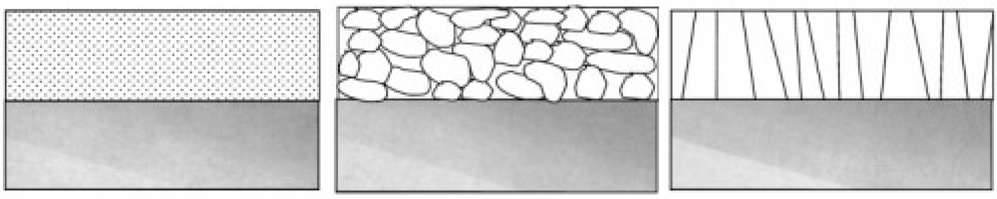

(a) Single crystal (b) Polycrystalline (c) Columnar

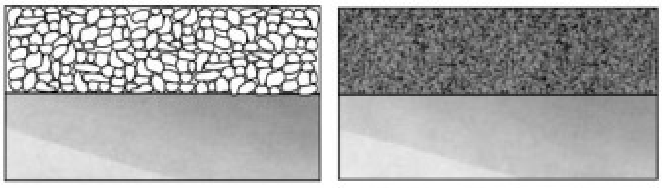

(d) Nano-crystalline (e) Amorphous

Figure 3.1: Inner structure of barrier materials[9]

barriers represent the ideal solution.

However material and process type constraints, along with lattice mismatch with the substrate, make it unlikely for the deposition of these films in single crystal form. Therefore nano-crystalline or amorphous materials represent the best compromise in terms of performance, stability and compatibility with the underlying bulk.

3.1.1 Sheet resistance

One of the main parameters which is usually taken into account to detect the failure of the barrier layer is the sheet resistance of the copper metallization. According to Ohm's law the resistance is defined as

$$R = \rho \frac{L}{Wt} \tag{3.2}$$

where ρ is the resistivity of the material, L is the length, while W and t refer to the cross-sectional area indicating respectively the width and the thickness(see figure 3.2). Equation 3.2 can be rewritten as

$$R = \frac{\rho}{t}\frac{L}{W} = R_s \frac{L}{W} \tag{3.3}$$

where R_s is the sheet resistance. It has been observed that upon barrier failure a steep increase of sheet resistance of the silicon wafer is usually observed. The reason related to this phenomenon can be found if we consider that diffused copper usually

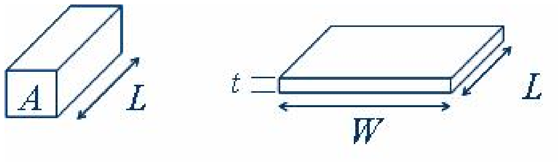

Figure 3.2: Representation of the sheet resistance parameters: from the images we can deduce that the cross-sectional area results $A = W \cdot t$

reacts with silicon atoms giving rise to Cu_3Si crystallite that acts as contaminant in the silicon bulk causing a steep increase of the sheet resistance.

3.2 Titanium and Titanium nitride

These materials are commonly employed in aluminum-based or silver-based metal contacts; their application in solar cells had already been mentioned in various publications(see reference [39]) as a new approach for the production of low-cost and more reliable solar cells with silver contacts.
Several attempts to use them also for copper metallization have been reported in literature[9]. The only disadvantage is represented by the fact that these materials do not provide a satisfactory barrier performance for thickness below 20 nm. Particularly titanium-based barriers fails primarily because of some metallurgical reactions with copper, while TiN loses its barrier function because of grain boundary diffusion. As shown in figure 3.3, the inner structure of these materials exhibits a columnar type morphology, with grain boundaries running along the entire thickness of the TiN film. The inner structure of TiN thus provides a fast diffusion pathway for copper diffusion causing substantially the barrier failure.
It has been observed that the performance of TiN barriers is enhanced through the exposure to air before the metal deposition. This behaviour is attributed to the diffusion of oxygen to grain boundaries so that it subsequently reacts with the metal giving rise to an oxide layer which acts as new barrier for the diffusion process.
Besides the poor performance of TiN with very thin thickness, one of the main concerns that affects the use of this type of barriers is related to the deposition techniques. TiN films grown by CVD techniques, in fact, displayed a low-density, high resistivity and porous micro structure with the presence of high concentrations of carbon, oxygen and hydrogen contaminants. Other efforts to remedy this problem including the use of MOCVD techniques have been carried out but these attempts did not yield the optimized TiN barrier performance.[6]

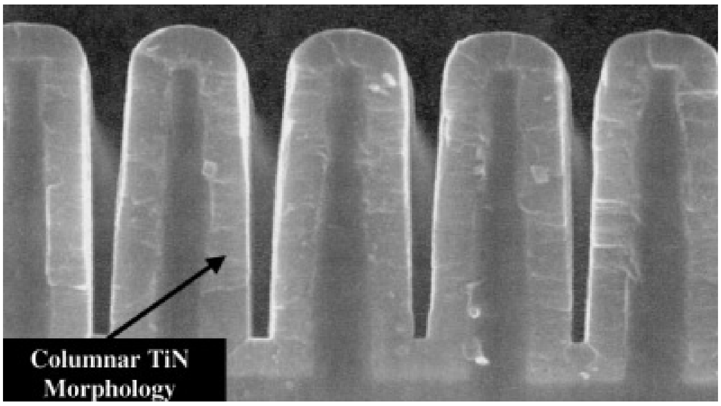

Figure 3.3: Inner structure of TiN[9]: the columnar structure of the barrier material results clearly visible. Particularly it is possible to notice the presence of narrow and long interstitial spaces where copper atoms can freely diffuse

3.3 Electro-plated nickel

The state-of-art of the manufacturing of copper contacts is nowadays focussing primarily on nickel, since the deposition of this material can be accomplished using an electro-plating technique that avoids the metal etching and ensures a good stability of the deposited substance. The electroless nickel can be deposited on the surface of polysilicon without any activation process due to the following displacement reaction[15]:

$$2Ni^{2+} + Si \longrightarrow 2Ni + Si^{4+} \tag{3.4}$$

the displacement reaction proceeds until the surface of polysilicon is covered with an amorphous Ni layer. In order to complete this chemical reaction a reduction agent is usually required; for this kind of application hypophosphite represents the most suitable substance since it presents wide operation parameters and a long solution life.[15]

It is found that electroless nickel barrier exhibits an amorphous structure until heat treatment at 300°C. During the thermal treatment, some interactions between Ni and Si can occur giving rise to complexes such as Ni_2Si, $NiSi$, and $NiSi_2$. However copper was not found to diffuse in the silicon layer, it simply remained at the top of the surface of the Ni layer. It is worth to mention that when Ni is brought into contact with polysilicon, a chemical reaction usually occurs so that Ni silicide is usually formed. The resulting barrier for copper diffusion is thus represented by a Ni silicide layer, as shown in picture figure 3.4.

The picture substantially shows an intact structure after the annealing treatment as a result of a effective barrier function of the material under investigation. Nonethe-

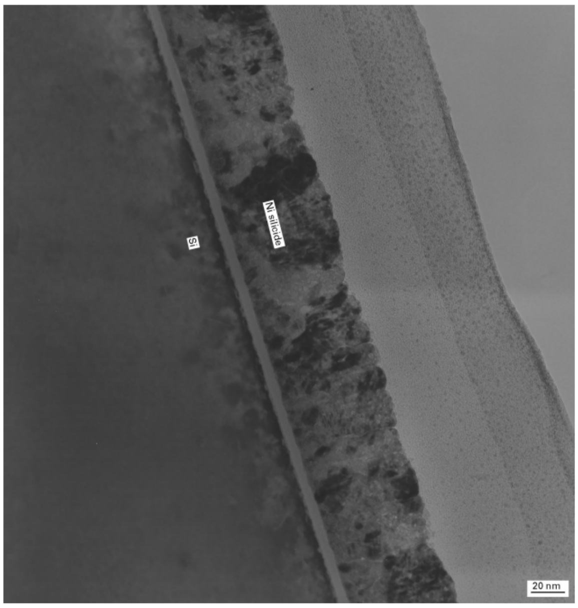

Figure 3.4: Formation of nichel-silicide after annealing treatment; as we can see from the picture the structure of the barrier is still intact and the presence of the silicide does not affect the effectiveness of the barrier[15]

less it is reported that these layers keep their integrity only up to 350°C, a temperature that results considerably lower compared to other materials mentioned in the next paragraphs.

As already stated, it was reported that the first solar cells with copper metal contacts have been recently introduced on the market employing electroplated Ni as diffusion barrier.[1] However it is likely that other solar cells employing barrier materials with improved thermal and electrical characteristics will be presented soon.

3.4 Tantalum-based barriers

Tantalum-based layers present an inherent advantage over their titanium-based counterparts. Copper and tantalum, indeed, are almost completely immiscible up to their melting points and do not react to produce any compounds. In addition, tantalum has a very high melting point, thus the activation diffusion energy Φ, that was introduced in equation 2.7, is considerably higher than Ti counterparts. Indeed its estimated value resulted to be around 2.3 eV for copper diffusion.[6] As already stated, a wide temperature range is usually one of the most important requirements for these barrier materials because copper diffusion must be avoided

throughout the fabrication process. Some other results also showed that tantalum acts as a good diffusion barrier with temperatures up to 550°C with 50-nm thick Ta-films[11].
In order to compare the barriers introduced in the previous paragraph with tantulum-based counterparts in terms of performance as a function of time, some studies were carried out employing test capacitors that consisted of layers with different thicknesses. In figure 3.5 the mean time-to-failure, for an average of 10-16 samples has been reported. The data clearly show that Tantalum is more effective than TiN as a diffusion barrier in copper metallization. The figure 3.5 also reveals that the performance is slightly increased after an annealing step; this behaviour is probably related to the fact that annealing removes some micro-defects in the Ta microstructure.[12]

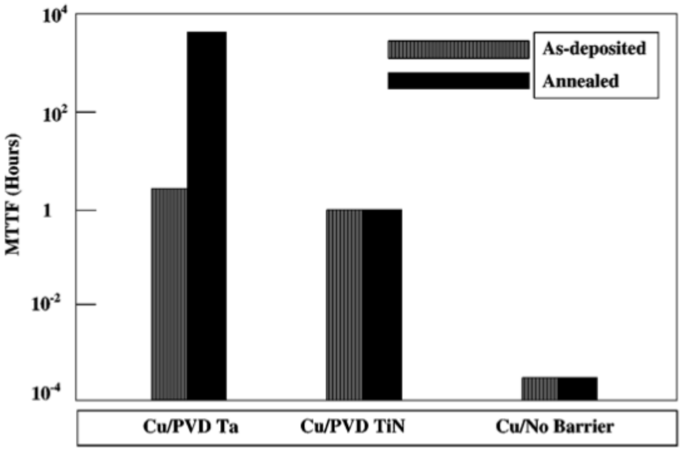

Figure 3.5: Comparison between tantalum and TiN barriers: the performance is evaluated in terms of the mean time to failure(MTTF); note that the annealing step produces beneficial effects only on Tantalum-based barriers [12]

Apart from annealing, one of the most promising attempts to enhance the performance of the barrier is represented by the doping of tantalum in order to form amorphous structure with a very high recrystallisation temperature. Theoretically amorphous layers are expected to be more robust barriers because the ordered structure depicted in figure 3.3 generates some interstitial spaces that allow copper to cross the entire layer causing the failure of the barrier. [9] Although this type of barriers showed a satisfactory performance in terms of the rejection of copper diffusion, there are no available information on their applicability on PV devices, thus their use in solar cells is still under investigation.

3.4.1 Tantalum-nickel barriers

Since nickel barriers showed a good performance on solar cells, other alloys, such as Ta-Ni barriers, are likely to become an interesting alternative for the rejection of copper diffusion. Ta-Ni alloys usually show an amorphous structure which is basically free of grain boundaries. Therefore Ta-Ni presents the usual advantages of amorphous micro-structure while preserving the good conductivity offered by the constitutive materials. However during the deposition of these barriers a certain amount of oxygen is usually incorporated in the inner structure of these liners so that a TaNiO barrier in formed.

The sheet resistance at room temperature and after annealing at temperatures between 500°C and 800°C has been deeply studied. After the samples were annealed at 500°C, we can notice that a drop of resistance which is attributed mainly to the growth of copper crystals; in practice, when the metal layer is deposited on the barrier by sputtering, it usually presents a small crystal size with relatively higher electrical resistivity.[14] At 600°C and 700°C a slight increase of resistance can be observed. This could be related to an interface reaction between neighbouring layers that might take place without the self recrystallisation of the materials; figure 3.6[14] shows the performance of these barriers in which different concentrations of nickel and oxygen have been varied. Particularly Ta tends to react with the underlying silicon bulk at low temperatures, the interfacial reaction between Ta and Si appears to be delayed up to 800°C with a sufficiently high concentration of oxygen. However in figure 3.6 the barrier failure occurred at the same temperature for both the two samples demonstrating that it is mainly caused by the crossing of the copper atoms through the barrier layer rather than the interactions between the neighbouring layers of Ta and Si. This assumption is confirmed by the TEM images of Cu/TaNiO/Si barrier liner at different annealing temperatures(600°C, 700°C and 800°C). Although the variation of the sheet resistance shows that the failure of both the two barriers occurs at the same temperature, TEM images show that with a higher oxygen concentration the failure of the barrier starts with the reaction of Ta with oxygen, whereas the formation of particles containing copper and silicon in a ratio close to 3:1 is the starting failure mechanism for $Ta_{73.25}Ni_{26.1}O_{0.65}$ barriers. In the former case, however, the barrier showed a preferable behaviour since it avoided the reaction of the Cu ions with Si as opposed to the counterpart with a lower oxygen concentration where the formation of Cu complexes demonstrated the substantial failure of the liner. Thus a certain amount of oxygen helps to delay the Cu diffusion and the formation of Cu_3Si particles, leading to an improved performance.

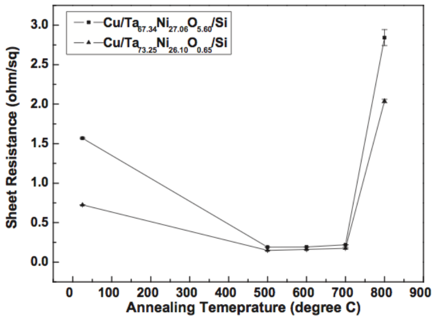

Figure 3.6: Sheet resistance as a function of annealing temperature[14]

Finally at 800°C we can notice that both the two films lost their own integrity, as shown in figure 3.7d, where Cu and Ta-Ni layers are no more distinguishable.

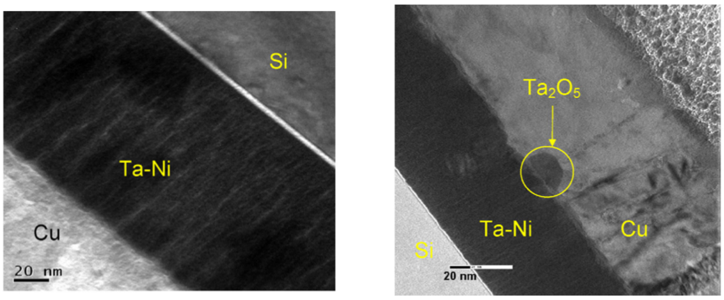

(a) 600° annealing:the structure is still intact

(b) 700°C: reaction of Ta with Oxygen

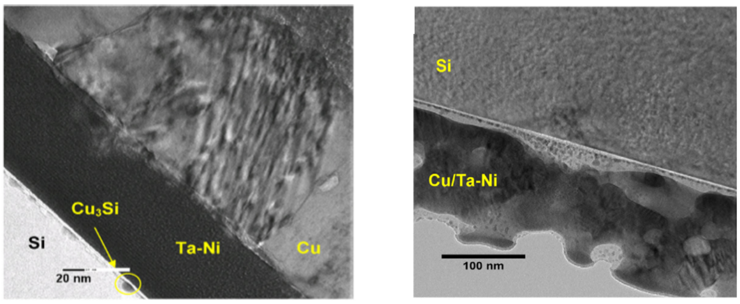

(c) 700°C: formation of Cu-silicides

(d) 800° annealing:Barrier failure

Figure 3.7: Testing of a Ta-Ni liner as a function of the annealing temperature

3.5 Co/TaN bilayers

In order to enhance the adhesion properties of these barriers, a bilayer structure consisting of a thin Co sheet and a TaN barrier represent a promising alternative.

In this paragraph a comparison between the barrier properties of Co/TaN stack and the single Co as barrier layer will be presented. Particularly the former structure is made up of two layers with different functions: the TaN has been employed as effective barrier for copper diffusion while Co acts as an adhesion layer and it is placed in direct contact with copper metallization. The results regarding the sheet resistance variation for Cu/Co(10nm)/Ta(10nm)/Si and Cu/Co(10nm)/Si structures as a function of annealing temperatures are shown in figure 3.8.[13]

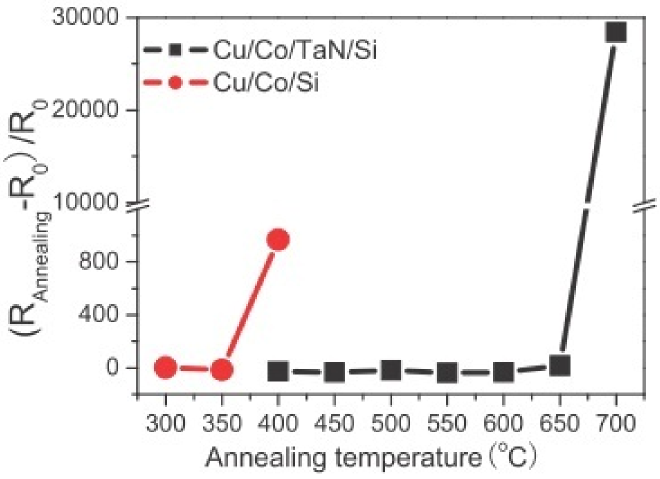

Figure 3.8: Comparison between Cu/Co/TaN/Si and Cu/Co/Si structures in terms of the failure temperature. The performance of the barrier is evaluated measuring the sheet resistance before(R_0) and after annealing($R_{annealing}$)[13]

It can be immediately noticed that the sheet resistance is substantially stable at temperatures included in the range between 400°C and 600°C, then it presents a slight increase around 650°C and abruptly increases after annealing at 700°C indicating the failure of the copper barrier and the formation of Cu_3Si due to the reaction of the copper diffused atoms with the silicon bulk. According to the data shown in the figure, we can also notice that single Co layer(10 nm) is not a good barrier. Indeed from the figure we can also see that the sheet resistance of the Co layer presents a steep increase when the annealing temperature overtakes the threshold of 350°C, resulting much lower in respect to TaN barriers.[13] It is also worth to mention that in order to have a good performance in terms of thermal stability and high resistance to electromigration, the orientation of Cu lattice and the underlying Co layer must be matched. Referring to the samples whose results have been shown in figure 3.8, it has been reported that a highly oriented copper metallization had been deposited on the Co/TaN layer, while that on the Co layer did not have a highly oriented texture. This is a further explanation of the reason why Co layer presented a very poor performance. Furthermore a significant Cu and Co interdiffusion and oxidation has been observed after annealing: the top layer which was initially made up of Co, has become a mixed layer of CuCoO[13]; this is due to the fact that, although copper and cobalt are immiscible, Co can diffuse into the Cu grain boundary, thus this kind of structures usually require other layers aimed at preventing Co diffusion into the Cu lattice.

In conclusion it is possible to affirm that Co/TaN bilayer is an adhesion/diffusion barrier layer that shows good thermal stability and good adhesion with copper at least with annealing temperatures up to 500 °C, although further investigations are required for a complete understanding of their behaviour.

3.6 Mo/MoN bilayer

In this section a new bilayer structure will be analysed. Co/TaN bilayer structures had already been introduced in the previous paragraph; in that case the Co layer was not introduced to enhance the barrier properties of the structure, but rather to improve the adhesion of copper to the barrier structure. Instead Mo/MoN is a structure that provides a double barrier to copper diffusion; it is known that a bilayer structure offers an enhanced barrier performance, as Cu atoms must diffuse through a longer path due to the grain boundary mismatch between the two layers. Many experiments were carried out employing layers with different thicknesses[19]; with a very thin thickness(5 nm) these structures showed an excellent performance with temperatures up to 700°C; figure 3.9[19] shows the performance of a Cu/-Mo/MoN/Si structure annealed at different temperatures. We can immediately notice that for annealing temperatures below 700°C, no Cu silicides are formed. After annealing at 700°C for 10 minutes, some small dots appear in the SEM image indicating the formation of Cu_3Si complexes which result from the diffusion of Cu through the barrier stacks into the Si substrates. The concentration of Cu_3Si complexes significantly increases after annealing at 800°C, suggesting that a larger amount of Cu atoms reacted with Si atoms to form Cu silicide; figure 3.9[19] shows the surface morphology of the sample after annealing at 800°C.

In summary it resulted that rupture of Cu barrier films and formation of crystallites often occurs upon annealing at 700°C. Moreover Cu starts to agglomerate since many pinholes could be observed throughout the film surface(see figure 3.9d). The results shown in figure 3.9d[19] are also confirmed by the sheet resistance measurements. Particularly below 700°C the sheet resistance appears to be stable, whereas after annealing at 700° the image shows a little variation of the sheet resistance,

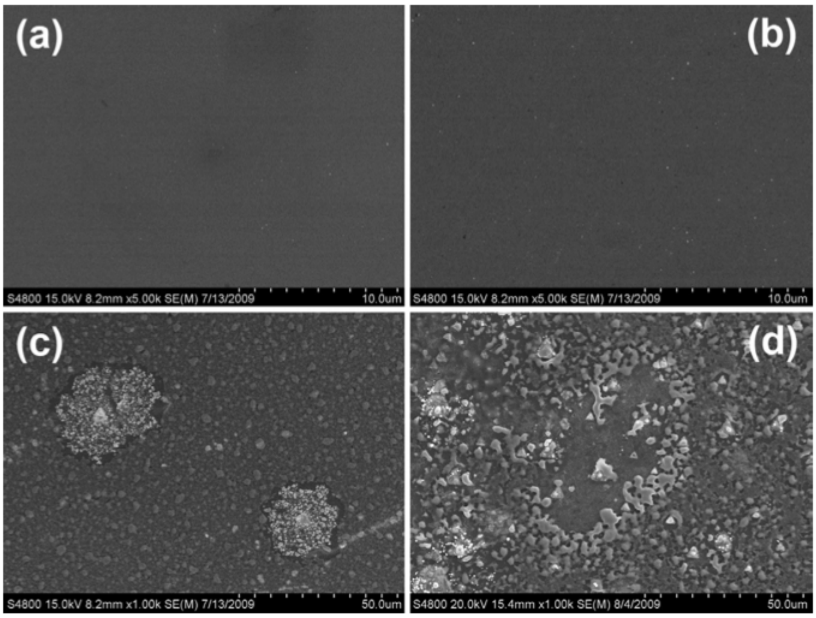

Figure 3.9: SEM images of Cu/Mo(5nm)/MoN(5nm)/Si structure; figure a: barrier at room temperature b.after 600°C annealing c. after 700°C annealing d. after 800°C annealing[13]; the white dots shown in the picture indicate the presence of silicides - hence the barrier failure

which is probably due to the initiation of Cu agglomeration and formation of localized defects. After annealing at 800°C an abrupt increase of the resistance occurs, indicating the formation of highly resistive products, such as silicides.

These bilayer barriers resulted particularly interesting for the VLSI applications since they provided very good performance employing very thin layers(with thickness between 5 and 10 nm). Although these materials have not been tested yet on PV devices, their good performance not only in terms of rejection of copper diffusion but also for their enhanced adhesion properties to the copper layer could make these materials a valid alternative to nichel-based barriers.

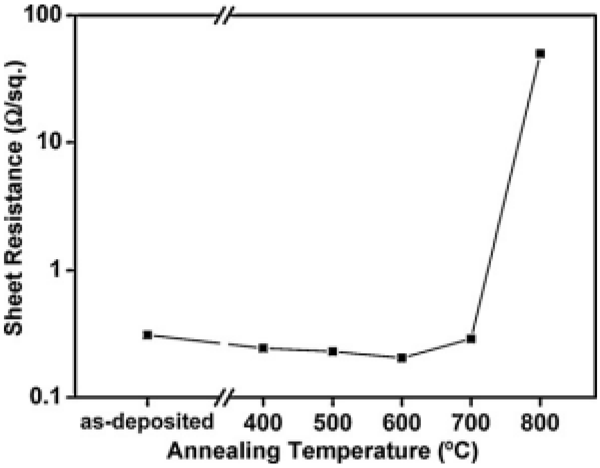

Figure 3.10: Variation of sheet resistance of Cu/Mo(5nm)/MoN(5nm)/Si as a function of sheet resistance[13]; failure occurs around 700°C

3.7 Tungsten carbides

Carbides of refractory metals, such as TiC, TaC and WC films, have been studied as diffusion barriers due to their high melting point and good thermal stability. Particularly many comparative studies on the properties of W and binary W_xC_y films as copper diffusion barriers have been carried out. Tungsten carbides showed a similar performance in terms of sheet resistance and resistance to copper diffusion at high temperatures compared to W barriers. The figure below shows the sheet resistance(R_s) variation as a function of the annealing temperature for four different compounds: W, W_7C_3 and W_5C_5 and W_3C_7.
It can be seen that sheet resistance increases rapidly after annealing at 750°C for all types of barriers. The steep increase of the sheet resistance is due to the fact that copper diffuses through the barrier layer and reacts with the silicon substrate giving rise to Cu_3Si during the annealing process. Although the sheet resistance increases significantly at the same temperature as the other materials, other experiments show the presence of W oxide on the silicon surface only after annealing at 600°C. This indicates that W carbides present a higher resistance against oxidation. Changing the ratio between the concentration of tungsten and carbon atoms the crystalline structure of the material results clearly altered. Particularly for the W_7C_3 film with a high W percentage, a polycrystalline structure has been observed. Increasing further the C content, W_5C_5 and W_3C_7 films resulted to exhibit an amorphous structure that usually provides better results; indeed amorphous liners are generally considered the optimal pattern for the barrier performance because they prevent grain boundary diffusion.

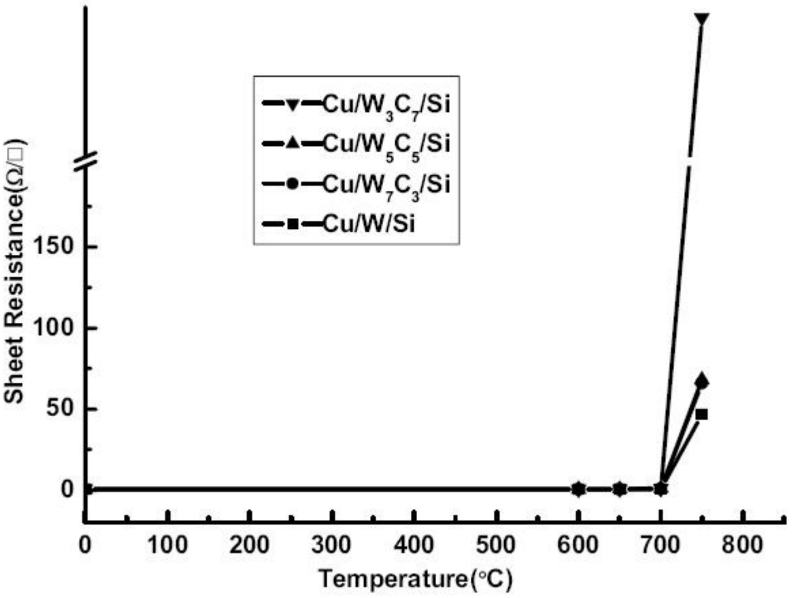

Figure 3.11: Variation of the sheet resistance at different annealing temperatures; a steep increase of the sheet resistance is visible at 700°C for all the barriers in which the ratio between C and W has been varied[16]

Several experiments aimed at the determination of the breaking point of the inner structure of these barriers were carried out.[16] In order to estimate the roughness of the barrier film, laser light scattering measurements were employed and the results are shown figure 3.12; particularly these measurements have been carried out as a function of the annealing temperature with a ramp-rate of 3°C(in other words the temperature is increased with a step of 3°C).

It can be immediately noticed that, although the resistivity of the material remains stable up to 750 °C, the barrier starts to recrystallize at lower temperatures. As a matter of fact, the optical roughness depicted in figure 3.12 presents a steep increase at 570 °C, therefore the inner structure of the material is modified at a lower temperature than the one predicted by the resistance measurements. Other experiments were carried out to find the reason for the rapid increase of the surface roughness of the material. Figure 3.13 shows that at higher annealing temperatures than the failure point, dark holes on the copper films are formed, thus it is assumed that the sudden increase of the surface roughness is mainly due to copper agglomeration. On the basis of the data shown in figure 3.11 and figure 3.12, the activation energy for copper diffusion in this kind of barriers can be estimated by

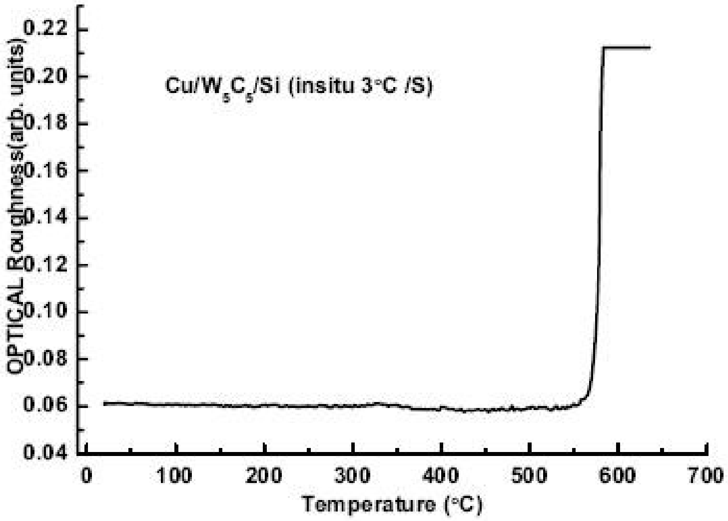

Figure 3.12: Variation of the roughness as a function of temperature[16]

exploiting an equation known in literature as Kissinger equation

$$ln\left(\frac{\Phi}{T^2}\right) = -\frac{E_a}{KT} \tag{3.5}$$

where Φ is the ramp rate, T is the critical temperature, k is the Boltzmann constant and E_a is the activation energy[17]. On the basis of the data provided by the surface roughness measurements, the estimated activation energies resulted 1.42, 0.53, 0.62 and 0.67 respectively for W, W_7C_3, W_5C_5 and W_3C_7[16]. This indicates that the adhesion between copper and tungsten is the strongest.
Therefore it can be concluded that WC film has better resistance against oxidation and comparable barrier performance as pure W film, but on the other hand the adhesion strength between copper and tungsten carbides results to be considerably lower.

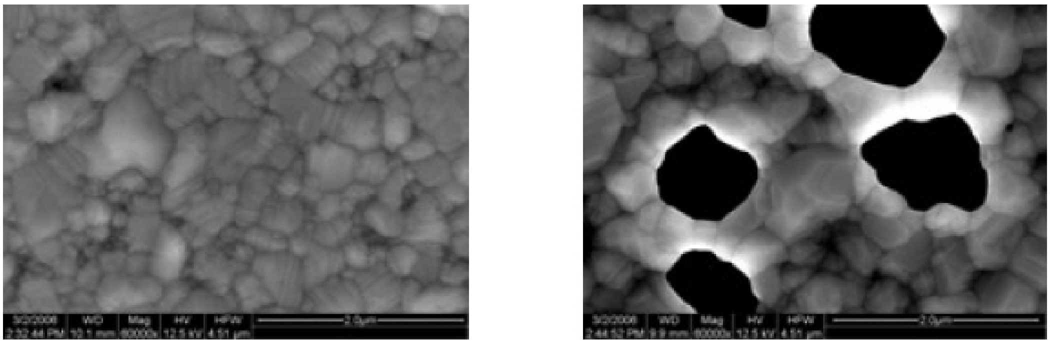

(a) 515° annealing (b) 570° annealing

Figure 3.13: Effects of copper diffusion[16]: we can notice that at high annealing temperatures the barrier loses its functions allowing the formation of copper agglomerates that appear as black spots in the right figure

3.8 Amorphous Ternary Liners

In the previous sections, we have dealt exclusively with single or binary transition metal nitrides. The addition of a third element disrupts the crystal structure of the binary alloy giving rise to the formation of a stable amorphous ternary phase with a higher recrystallisation temperature. Many diffusion barriers belong to this group and they include silicon-, carbon- or boron-doped Ti-, Ta- and W-based nitrides. All these barriers share the same failure mechanism which is grain boundary diffusion after a recrystallization process. Initially these materials did not represent an interesting alternative to the binary counterparts because those barriers fabricated with these materials resulted to be very thick(thicknesses greater than 100 nm). Research on several materials, among which $TaSi_xN_y$, has provided interesting results. Barriers fabricated with this material provided a good performance, even with very thin layers. It has been reported that 5-nm thick PVD layer prevented copper diffusion after annealing at 400°C. As in the case of Tantalum nickel layers, stoichiometry influences appreciably the diffusion barrier properties. Considering that the main barrier failure is usually attributed to thermally induced recrystallization, figure 3.14 shows the barrier failure temperature and the resistivity as a function of the stoichiometry of the material[9]. As we can see from the picture, the barrier failure temperature is directly proportional to the N concentration in the lattice; this result confirms what has already been stated in the previous paragraphs: N atoms prevent the diffusion of copper, since they fill the interstitials and the grain boundaries. On the other hand, we can also notice that a high concentration of nitrogen atoms causes an increase of resistivity of the material.[9]

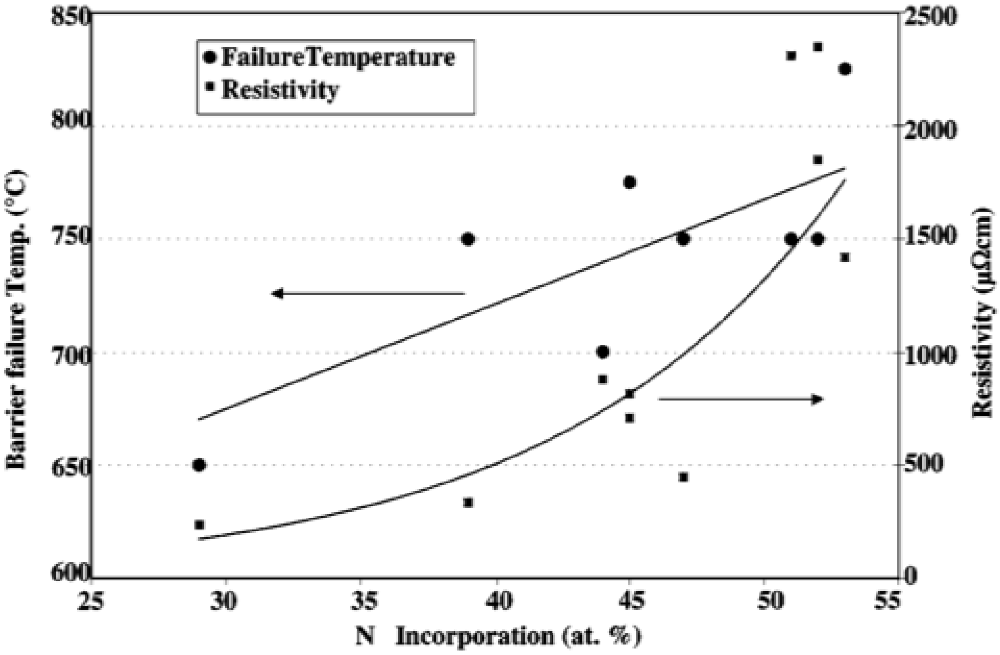

Figure 3.14: Influence of nitrogen incorporation on the barrier failure temperature[6]: the failure temperature follows a linear relationship whereas the resistivity described a quadratic curve as a function of the nitrogen concentration

Since we are dealing with ternary compounds, we have a new degree of freedom represented by silicon concentration; figure 3.15[9] shows the variation of the barrier failure temperature as a function of silicon concentration. We can immediately notice that silicon concentration does not have relevant effects on the resistivity, whereas the barrier failure temperature seems to decrease with very high concentrations. Thus a trade-off between nitrogen and silicon concentration must be found in order to ensure the best performance.

Tungsten-based ternary materials were also examined as diffusion barriers for copper metallization; although most studies employ relatively thick films, these materials appeared to possess barrier properties that resulted to be equivalent to those for titanium and tantalum-based ternary barriers. The deposition of these materials is usually performed through PVD or CVD techniques; more recently, inorganic CVD techniques were developed for the low-temperature deposition of ultrathin $TiSi_xN_y$ and $TaSi_xN_y$ barriers which are characterized by a lower resistivity and a very good performance in terms of temperature failure, which is expected to be around 600-700 °C; however this is still a research topic, thus many results concerning these materials have not been published yet.

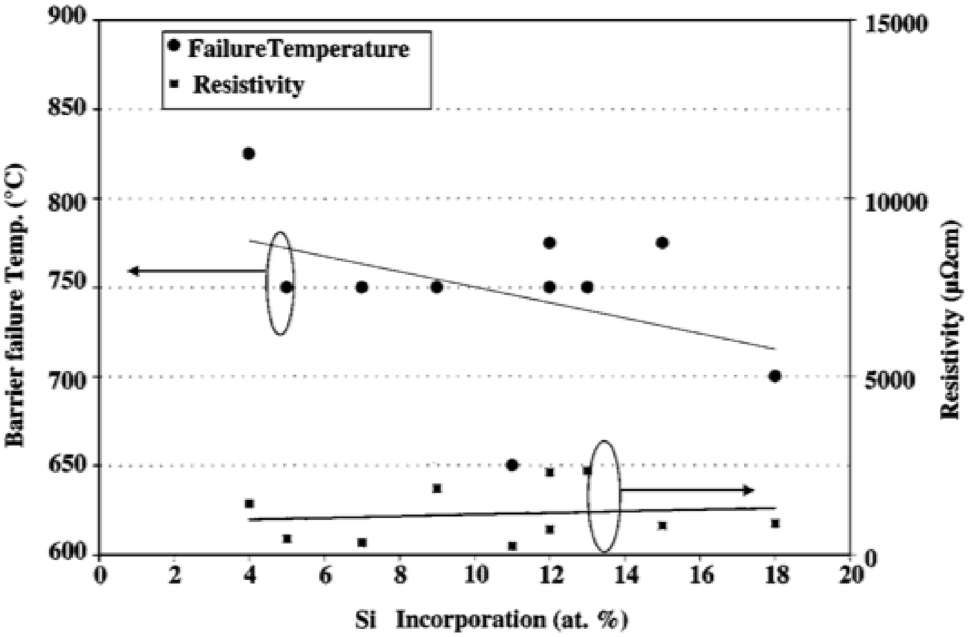

Figure 3.15: Influence of silicon concentration:[6] the barrier temperature failure results a decreasing linear function whereas the resistivity seems to be independent of the nitrogen incorporation

3.9 Conclusion and future improvements

The material that generally showed the best performance was Mo/MoN structure whose barrier failure temperature resulted very high and the bilayer structure allowed the enhancement of the adhesion properties. The fact that these barriers provided very good performances employing extremely thin layers made them particularly interesting for VLSI applications. Nowadays the most widely used material for the realisation of copper contacts on solar cells is nickel and its alloys; nonetheless all the other materials mentioned above might be used for PV devices as well, since the desired features of these materials in terms of resistance and stability at high temperatures could result the same for both the two applications. However the reduction of the production costs requires not only the research on new materials but also the development and optimization of new deposition techniques. As a result, some techniques such as atomic layer CVD and atomic layer deposition(ALD), that were mentioned in the previous paragraphs, represent the most interesting candidates for a large-scale production. These techniques are based on the the growth of single molecular layers of the desired material so that the thickness of the barrier can be controlled with a very high accuracy; in particular thicker films are produced through repeated growth cycles until the desired

target thickness is met. In order to optimize the fabrication processes, the future deposition techniques will combine know-how of atomic scale monolayer growth with predictive modelling using accurate simulators, to grow thin liners with the required properties and performance.
Nowadays research is focussing primarily on the applicability in PV devices of these materials that had already been tested for VLSI applications and on the optimization of the deposition techniques so that the use of these barriers can be introduced in a large-scale production, where the reliability and the reduction of production costs are the main issues.

This chapter was intended to provide a literature survey on the state-of-art of these layers and their effective effectiveness in preventing copper diffusion. All the materials presented in the previous paragraphs presented a common behaviour: when the temperature exceeds a certain threshold, a considerable amount of copper overtakes the barrier, leading to the contamination of the underlying substrate. During the fabrication steps, these temperature limits are usually exceeded, thus an effective method for the reduction of this contamination must be found. The next chapters will focus initially on analysis of the effects of this contamination and subsequently on the development of a technique aimed at its removal from the substrate.

Chapter 4

Lifetime measurements

The presence of defects introduced by copper strongly affects an important parameter, called *lifetime*, which will result fundamental for the understanding of the next chapters. As already stated, these defects cause the establishment of some energetic levels in the band gap which act as traps for the electrons promoted to the conduction band by the incident light. In practice, these electrons receive a certain amount of energy so that the covalent bonds existing among the silicon atoms of the crystal lattice are broken; as soon as these electrons are promoted to the conduction band, they can contribute to the conduction process or alternatively they can be trapped in the defects. As a consequence an average lifetime is usually defined in order to estimate the average elapsed time between the generation of a free carrier and the trapping in one of the defects of the crystal lattice. This chapter will provide a brief *theoretical background* to all these phenomena resulting particularly useful for the understanding of the next chapters where the lifetime will be considered as the reference parameter for the analysis of the experimental results.

4.1 Recombination processes

Various categories of recombination are often present in silicon wafers:

- Recombination through impurities and defects in the bulk, also known as SRH recombination;
- Recombination at the surface;
- Radiative recombination;
- Auger recombination;

The various types of recombination that occur in the bulk of a wafer are usually collected together so that the effective lifetime is represented by the sum of several factors:

$$\frac{1}{\tau} = \frac{1}{\tau_{auger}} + \frac{1}{\tau_{rad}} + \frac{1}{\tau_{SRH}} + \frac{2S}{W} \tag{4.1}$$

where $\frac{2S}{W}$ accounts for surface recombination(S represents the surface recombination velocity and W the wafer thickness), whereas τ_{auger}, τ_{SRH} and τ_{rad} indicate the contributions given by the different recombination mechanisms to the measured lifetime. In the next paragraphs a brief explanation of all these recombination processes will be presented. Note that there are also cases where some of these recombination mechanisms are absent or negligible.

4.1.1 Radiative recombination

Radiative recombination implies that electrons and holes recombine through the emission of a photon. Under equilibrium conditions, the law of mass action states that the product of electrons and holes is constant, i.e.

$$n_0 p_0 = n_i^2 \tag{4.2}$$

The adsorption of light generates an excess carrier concentration so that we can write $n = n_0 + \Delta n$ and $p = p_0 + \Delta p$. The recombination rate is usually given by the following equation

$$-\frac{dn}{dt} = -\frac{dp}{dt} = Bnp \tag{4.3}$$

Assuming that $\Delta n << (n_0 + p_0)$, i.e. a low generation level, the generation rate is expressed as $R = B[n_0 + \Delta_n(t)][p_0 + \Delta_p(t)]$, where B is a proportionality constant called *bimolecular recombination rate*, can be simplified so that equation 4.3 can be rewritten as

$$\frac{d}{dt}\left[\Delta n(t)\right] = -B(n_0 + p_0)\Delta n(t) \tag{4.4}$$

whose solution is

$$\Delta n(t) = \Delta n_0 e^{-B(n_0+p_0)t} = \Delta n_0 e^{-\frac{t}{\tau}} \tag{4.5}$$

where τ is the minority carrier lifetime, defined as the time constant of an exponential function representing the decay of the excited carriers after illumination. In case of high excitation levels, equation 4.4 modifies into

$$\frac{d\Delta n(t)}{dt} = -B\Delta n^2 \tag{4.6}$$

whose solution denotes a non-exponential behaviour($\Delta n(t) = \frac{1}{Bt+\Delta n_0}$) where a time constant, defined as the amount of time required to decrease from Δn_0 to $\Delta n_0 e^{-1}$, can be defined as follows

$$\tau(t) = -\frac{\Delta n(t)}{\frac{d\Delta n(t)}{dt}} = t + \frac{1}{B\Delta n_0} \tag{4.7}$$

4.1.2 Recombination through defects

The recombination of free carriers via deep levels was first analysed by Schockley, Read and Hall(SHR-theory). The non-radiative recombination rate through a deep level is given by the following equation

$$R_{SR} = \frac{p_0\Delta n + n_0\Delta p + \Delta n\Delta p}{(N_T\nu_p\sigma_p)^{-1}(n_0 + n_1 + \Delta n) + (N_T\nu_n\sigma_n)^{-1}(p_0 + p_1 + \Delta p)} \tag{4.8}$$

where ν_n and ν_p are the electron and hole thermal velocities, σ_n, σ_p indicate the capture cross section of the traps, while n_1 and p_1 represent the electron and hole concentration if the Fermi level is located at the trap level, so that

$$n_1 = n_i e^{\frac{E_T - E_f}{kT}}, \quad p_1 = p_i e^{\frac{E_f - E_T}{kT}} \tag{4.9}$$

hence defining $\tau_{n_0} = \frac{1}{N_T\nu_n\sigma_n}$, $\tau_{p_0} = \frac{1}{N_T\nu_p\sigma_p}$ and $R_{SR} = \frac{\Delta n}{\tau}$ equation 4.8 becomes

$$\frac{1}{\tau} = \frac{p_0 + n_0 + \Delta n}{\tau_{p_0}(n_0 + n_1 + \Delta n) + \tau_{n_0}(p_0 + p_1 + \Delta p)} \tag{4.10}$$

Under the assumption that the trap captures electrons and holes are equal, i.e. $\nu_n \sigma_n = \nu_p \sigma_p$ and $\tau_{n_0} = \tau_{p_0}$, equation 4.8 simplifies into

$$\tau_i = \tau_{n_0} \left[1 + \frac{2n_i}{n_0 + p_0} cosh \left(\frac{E_T - E_i}{kT} \right) \right] \tag{4.11}$$

this equation shows the dependence of the lifetime constant as a function of the energetic position of the levels. If $E_T - E_i$ is zero, i.e. the trap level is close to the mid-band gap, the cosh function has a minimum, thus the non-radiative lifetime is minimized. As already stated in paragraph 2.2.1.1, the defects introduced by copper occupy different energetic levels, in particular they introduce traps which result very close to the mid-bandgap. These energy levels act as effective recombination centres, affecting heavily the lifetime constant.

4.1.3 Auger recombination

Another non-radiative recombination mechanism is represented by Auger recombination. In this process the energy that comes from the recombination of an electron-hole couple between the conduction and the valence band is dissipated by the excitation of a free electron into the conduction band, or by a hole deeply into the valence band. The recombination rates due to the Auger processes can be expressed as

$$R_{auger} = C_p n p^2 \quad , \quad R_{auger} = C_n n^2 p \tag{4.12}$$

where C is a proportionality coefficient, called *Auger coefficient*. Thus auger recombination results proportional to the square of the carrier concentration. The former equation is more likely to happen in p-type semiconductors, since the majority carriers are represented by halls, while the latter is more likely in n-type semiconductors. In the high-excitation conditions and under the assumption that $n = p$, the Auger rate introduced in the equation 4.12 reduces to

$$R_{auger} = (C_p + C_n) n^3 = C n^3 \tag{4.13}$$

4.1.4 Surface recombination

One of the main factors that deeply affect the minority carrier lifetime is the surface recombination because near the surface the periodicity of the crystal lattice is suddenly broken and this modification implies the addition of electronic states within the forbidden gap of the semiconductor. In other words, if we analyse the semiconductor surface from a chemical point of view, atoms on the surface cannot form the same amount of chemical bonds as bulk atoms due to the lack of some neighbouring atoms. The presence of these partially filled electron orbitals, also called *dangling bonds*, are electronic states that can be localised in the forbidden gap. These missing bonds can also cause the rearrangement of the atoms that constitute the crystal lattice, giving rise to a locally different atomic structure. From the solution of the continuity equation near the semiconductor surface, the concentration of surface electrons is expressed by the following relation:

$$n(x) = n_0 + \Delta n(x) = n_0 + \Delta n = n_0 + \Delta n \left[1 - \frac{\tau_n S e^{-\frac{x}{L_n}}}{L_n + \tau S} \right] \tag{4.14}$$

where S the parameter introduced in equation 4.1. In particular for $S \rightarrow 0$ the minority carrier concentration at the surface is identical to the bulk value, whereas for $S \rightarrow \infty$ the minority carrier concentration at the surface approaches the equilibrium value.

The typical recombination velocity of silicon is 10 cm/s[20]; this value is usually reduced through the deposition of a passivation layer that restricts the amount of dangling bonds, thus preventing the rearrangement of the atoms in the crystal lattice. The passivation layer can be made up of different materials, such as silicon dioxide or aluminum oxide, and it is one of the most important parameters that must be taken into account for the enhancement of the minority carrier lifetime.

4.2 Lifetime scanning

4.2.1 μ-PCD basic principle

In the previous sections, a theoretical explanation of the different mechanisms that influence the minority carrier lifetime has been presented. This paragraph provides a brief description of the technique employed for the lifetime measurements that will be presented in chapter 7. The most common method for the determination of the carrier recombination lifetime is the photoconductance decay(PCD) technique, where the decreasing concentration of excited electrons is measured through the emission of laser pulses. This is a fast, contactless and non-destructive technique that allows the creation of a precise lifetime map; the lifetime, in fact, is measured along the wafer area so that the output provided by this measurement technique is a map that depicts the lifetime distribution across the sample surface. However, the recombination of the excess carriers occurs not only within the bulk but also at the surfaces, therefore the measured time constant includes all the contributions provided by SRH recombination, as well as surface and Auger recombination. Microwave photoconductive decay technique consists of the measurement of the reflected optical power; particularly when the light pulse hits the silicon surface, the excitation of the free carriers causes an enhancement of the semiconductor conductivity, so that it is possible to write

$$\sigma(t) = e(\mu_n n(t) + \mu_p p(t)) \tag{4.15}$$

where μ_n and μ_p are the electron and hole mobilities. The change of resistivity can also be written as

$$\sigma = \sigma_0 + \Delta\sigma \quad , \quad \Delta\sigma = q(\mu_n \Delta n + \mu_p \Delta p) \tag{4.16}$$

Thus it is well known that the microwave transmission, absorption and reflection properties of these materials strictly depend on their conductivity. In order to explain the change of reflectivity of the silicon wafer as a function of the conductivity, some concepts concerning microwave theory must be recalled. Particularly for an electromagnetic wave the impedance is defined as the ratio between magnetic field and the electric one; in practice the concept of wave impedance considers the description of uniform electromagnetic waves as being analogous to electric transmission lines that are sinusoidally excited; hence electric fields are analogous to voltages, whereas magnetic fields are analogous to currents. For the sample under measurement a complex-valued permittivity can be defined

$$\epsilon = \epsilon_r - j\frac{\sigma}{\omega} \tag{4.17}$$

where ω is the radian frequency of the incident wave. We can immediately notice that the imaginary part of the dielectric constant is directly dependent on the resistivity of the material, so that equation 4.17 can be rewritten as

$$\epsilon = \epsilon_r - j\frac{\sigma_0 + q(\mu_n + \mu_p)\Delta p}{\omega} \tag{4.18}$$

From the theory we also know that for plane waves whose electric field is transverse to the direction of propagation, the wave impedance is expressed as

$$Z_{TE} = \sqrt{\frac{\mu}{\epsilon}}\frac{1}{cos(\theta)} \tag{4.19}$$

where θ is the incidence angle from the axis normal to the surface of the wafer. Substituting equation 4.18 into equation 4.19 the wave impedance is expressed as

$$Z = \sqrt{\frac{\mu}{\epsilon_r - j\frac{\sigma_0+q(\mu_n+\mu_p)\Delta p}{\omega}}} \tag{4.20}$$

The reflectivity is defined as

$$\rho = \frac{Z - Z_c}{Z + Z_c} \tag{4.21}$$

where Z_c is the characteristic impedence of the medium. We can immediately notice from the previous equation that the reflection coefficient depends on the impedance Z, thus on the conductivity of the material. The reflected wave, therefore, presents a phase shift and an amplitude dependent on the variation of either the real and the imaginary part of the reflection coefficient ρ. In figure a sketch of a $\mu-$PCD system is presented and the right hand-side of the picture shows the shape of the power reflectance as a function of the conductivity of the semiconductor.

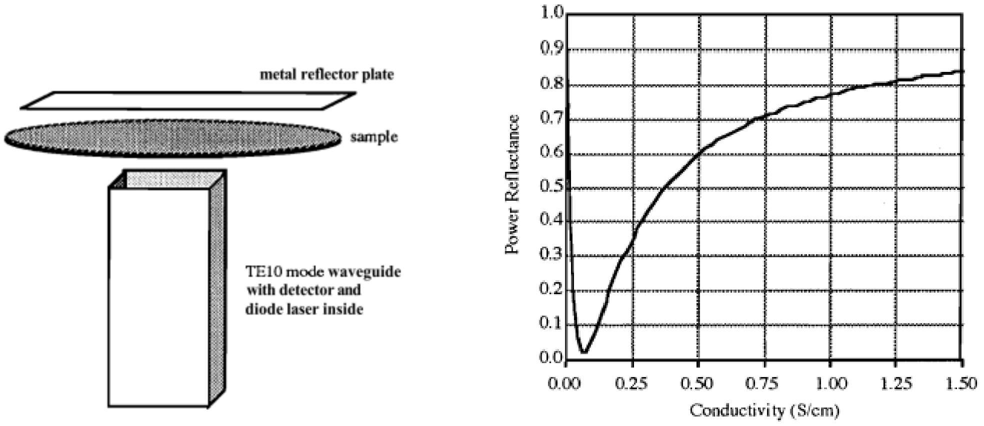

(a) A waveguide brings the radiation emitted by the laser diode; a metal reflection plate is placed behind the sample so that the emitted radiation traverses the air gap between the waveguide and the sample, the sample thickness and finally it is reflected back to the waveguide

(b) Power reflectance as a function of the sheet conductivity; the curve is obtained evaluating the reflectivity(ρ) coefficient whose value is dependent on the conductivity of the sample under measurement; we can notice that the power reflectance becomes a pseudo-linear function in a precise conductivity range

Figure 4.1: $\mu-$PCD measurement system[22]

We can immediately notice that the slope of the curve of the power reflectance(which is evaluated as ρ^2) is pseudo-exponential, but if we consider small deviations from equilibrium conductivities, the reflectance function can be approximated as linear and the amplitude of the reflected wave results exponential, since the time-decay of excess carriers follows an exponential decay law. Particularly the time constant can be evaluated through the following equation[21]

$$\tau_{PCD} = \frac{\Delta\sigma}{-\frac{\partial\Delta\sigma}{\partial t}} = \frac{\mu_n\Delta n(t) + \mu_p\Delta p(t)}{\frac{\partial(\mu_n\Delta n(t)+\mu_p\Delta p(t))}{\partial t}} \tag{4.22}$$

From the previous equation we can notice that the time constant evaluated employing this measurement system is a differential time constant and not an absolute time constant(the actual value is obtained evaluating the derivative of the conductance variation). Therefore it results clear that this measurement system requires two different light sources(sketched in figure 4.2[23]): a steady-state light generates the bias point and a laser pulse determines the increase in the conductivity and the subsequent exponential decay.

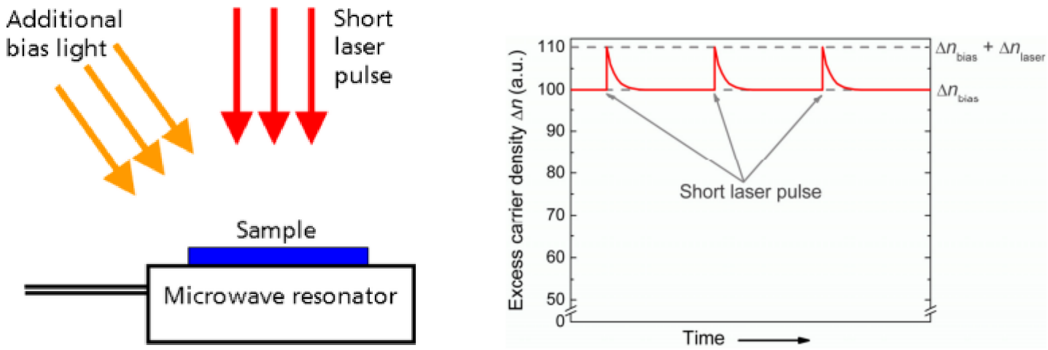

(a) Schematic of the measurement system: an additional bias light increases the conductivity of the sample until the power reflectance becomes a pseudo-linear function of the conductivity, and a pulsed laser light generates the excess photo-generated charge

(b) Time-dependence of the excess carrier density. On top of the steady-state bias illumination a short laser pulse generates additional excess carriers, which recombine subsequently.

Figure 4.2

4.2.1.1 Measurement equipment description

In figure 4.3 a schematic representation of the measurement process has been presented. As already stated in the previous paragraphs, the excess charge carriers are generated by a laser light pulse. The light source is a high power semiconductor laser diode with an appropriate optic to provide both good light collection efficiency and localized excitation of the wafer. Carrier recombination taking place after application of the pulsed light causes a photoconductive decay, which is recorded by time-resolved measurements of the microwave power reflected by the

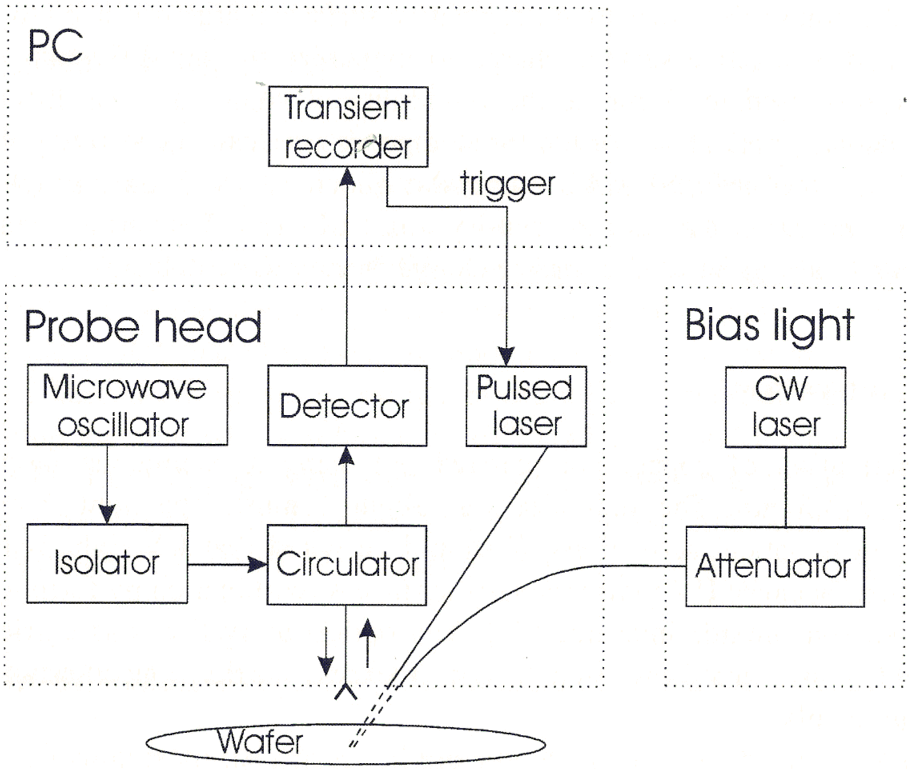

Figure 4.3: μ−PCD measurement scheme [21]: the bias light and the pulsed laser create the excess carrier on the sample; the change of reflectivity is detected by the probe incorporating a microwave oscillator and a specific detector

sample. The reflected wave contains a stationary part and another one dependent on the amplitude and phase of reflection coefficient ρ introduced in equation . In the output voltage of the microwave detector the excess carrier decay is evaluated comparing the stationary part of wave with the excess reflected component. The time constant of the decay is thus determined with a mono exponential fit to the photo-conductive decay and interpreted as being the recombination lifetime.

The pulsed light and bias-light are concentrated on a spot of about 1 mm^2, whereas the injected photons per pulse are equal to $1.2{\cdot}10^{15}$. In order to set the conductivity of the sample in a range where the power reflectance function shown in figure 4.1b has a linear shape, a bias light, whose intensity is adjusted manually by means of an attenuator, is introduced to reach a steady-state excess carrier concentration equal to $\Delta n = (6 \pm 1) \cdot 10^{15}\ cm^{-3}$.
The measurement apparatus is installed in a room temperature of $22°C$; some measurements of the sample temperature revealed that it usually ranges from $23°C$ to $27°C$ during lifetime measurements since the prolonged optical activation increased the sample temperature no more than $3\ °C$.

4.2.2 Quasi-Steady-State photoconductive(QSSPC) method

Another approach to measuring the carrier lifetime consists of a pulse of light that causes a sudden change of the surface conductivity of the sample.

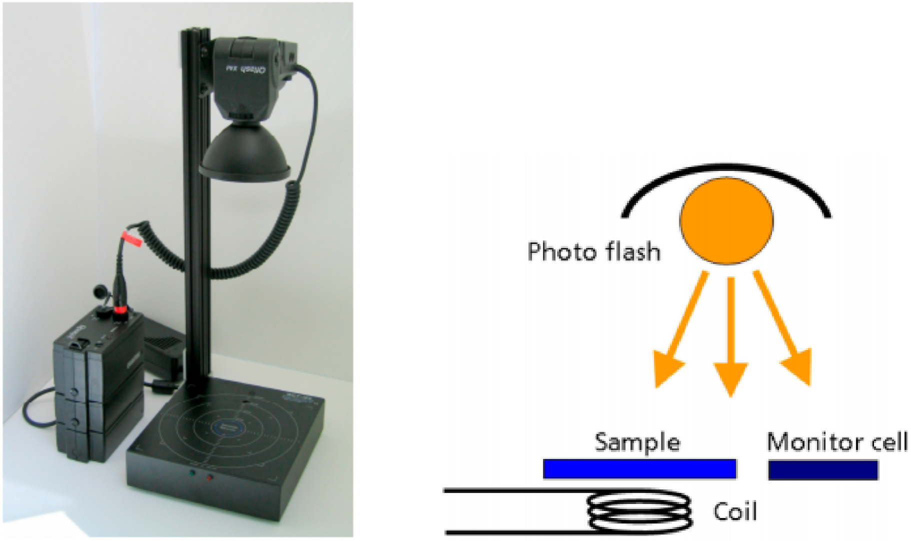

(a) QSSPC measurement system[23]

(b) The photo flash illuminates the sample on the stage and the monitor cell. The generated excess conductance within the silicon sample is measured using an inductively coupled coil and radio- frequency(RF) circuit.

Figure 4.4

This quasi-static approach is based on the following key steps:

- Exposure of the sample to a long, slowly-decaying pulse of light. This means that the excess carrier populations are always in steady-state conditions;
- Measure the sheet conductivity of the sample and the intensity of the flash light at the same time. Each moment corresponds to a different steady-state injection level;
- Convert the sheet conductivity into an average excess carrier density for each moment in time. This can be done using some models for carrier mobilities as functions of doping and injection;
- Convert the measured flash intensity into the generation rate of electron hole pairs for each moment in time;
- The lifetime τ is finally evaluated through the stady-state equation $\Delta n = G\tau$;

This method presents some advantages due to the fact that the lifetime is measured under steady-state conditions. On the other hand, this approach allows the measurement only of the average lifetime of the sample, thus it does not allow the tracing of a map of the lifetime distribution along the sample surface. Furthermore the change of conductivity is measured through a RF coil, which is made up of copper and could cause the contamination of the sample under test. For these reasons all the results, that will be presented in the next chapters, have been obtained through $\mu-$PCD measurements.

Chapter 5

Light-induced degradation

Defects introduced by copper diffusion show a peculiar behaviour: it has been observed that copper acts as a *lifetime killer* upon exposure to illumination. Therefore the effective lifetime suffers a steep decay during the exposure to the illumination; along with these copper introduced defects, other phenomena due to the presence of boron and oxygen in the silicon lattice usually take place determining a further decrease of the lifetime. As a consequence solar cells fabricated from copper contaminated bulks are subjected to a strong reduction of conversion efficiency upon exposure to the illumination; since different phenomena contribute to the degradation process, the development of a technique that allows a complete suppression of all these phenomena is impossible to achieve.

Recent studies have revealed the properties of this metastable defects, such as the electrical characteristics and the major components. In this chapter a detailed explanation of these new defects and all the processes that occur during the degradation will be presented. Based on this knowledge, some strategies will be investigated in the next chapters in order to reduce or even avoid the lifetime degradation.

5.1 Metastable defects behind LID

As already stated, a wide variety of defects are activated along with the copper introduced ones. Particularly some studies[24] revealed that light induced degradation is observed only on boron-doped silicon wafers with a sufficiently high concentration of interstitial oxygen. Indeed boron-doped p-type FZ silicon intentionally contaminated with oxygen showed a behaviour very similar to the degradation observed in Cz silicon, whereas no relevant degradation was observed on gallium-doped, phosphorus doped n-type samples and oxygen-free boron-doped p-type silicon. These achievements justify the hypothesis that boron and oxygen are the major components of the metastable defect that determine the lifetime degradation. Besides boron-oxygen, the lifetime degradation in Czochralski grown (Cz) silicon can also be attributed to various metal atom related defects, e.g. a complex of a lattice defect and a silver atom. Especially iron-boron pairs represent a particular type of defects, that dissociate under illumination and produce interstitial iron acting as a strong recombination centre. However, it is known that iron-boron pairs dissociate also under thermal treatment and they must be stored in the dark at temperatures below 100° C to recover the initial lifetime. Therefore, iron contamination is not the explanation for the degradation/recovery cycle at room temperature observed in boron doped Cz silicon.

5.1.1 Boron-oxygen complexes

Many models were developed in order to explain the light-activated degradation process. One of the first models explained the degradation process through the formation of a defect pair composed of one interstitial boron and one interstitial oxygen atom(B_iO_i) during illumination; other investigations confirmed the strong correlation between LID and the boron as well as the oxygen concentration; particularly they found an approximately linear increase of the lifetime degradation with boron doping concentration and a superlinear relationship(i.e. an increase that results to be much faster than a linear function) as a function of interstitial oxygen[24]. Furthermore other studies revealed that the energy level of light-induced recombination centres is close to the middle of the band gap as opposed to B_iO_i complexes whose energy level is located at $E_c - 0.26eV$. Thus these results gave rise to the suspicion that these recombination centres are probably associated with a defect complex different from B_iO_i pair. On the basis of these results, a new structure consisting of one substitutional boron atom and several other oxygen atoms was introduced. This model includes fast-diffusion oxygen dimers O_{2i} which

are captured by substitutional boron B_s giving rise to a $B_s - O_{2i}$ complex, acting as highly effective recombination center. Hence the defect formation is similar to the process which has already been examined for copper defects: the defect formation process is governed by the diffusion of the oxygen dimer and consequently it is a thermally activated process; according to this model the O_{2i} molecules are captured by other oxygen atoms or clusters to form extended defects, analogously to the processes that were shown in figure 2.2 for copper defects. Once these defects are formed, less O_{2i} molecules are available, therefore this model predicts a decrease in the $B_s - O_{2i}$ concentration and hence a reduced degradation of the minority carrier lifetime after the formation of these complexes. In other words, the decay of the lifetime is very steep during the first hours of illumination and it decreases gradually, reaching a saturation value. This behaviour has been proven by many investigations[30] whose results have shown the existence of two different defects, the former occurring within the first few minutes and the latter generating in several hours. The fast process causes a strong degradation during the initial stages, whereas the long-term process starts to dominate after few hours of illumination. These investigations also showed that these two processes are generated by defects with a similar composition that exist in two different configurations giving rise to these two different recombination activities.[30]
This behaviour will be confirmed through the experimental results that will be shown in chapter 7.

CZ silicon always contains a certain amount of oxygen which is incorporated during the processing of the ingot, therefore LID process due to boron-oxygen complexes is expected to be evident only on CZ wafers. Nevertheless some publications[26] revealed that the LID process was observed also on FZ samples; this degradation process is attributed primarily to the presence of several contaminants, such as copper or iron.

5.1.1.1 Recovery process

After the degradation due to the exposure to the illumination, it was found that the initial lifetime could be recovered through a short annealing treatment at 200°C. In practice the lifetime varies between two different values, corresponding to two different states of the meta-stable defects. State A is associated with a high lifetime, whereas state B corresponds to a low carrier lifetime and is caused primarily by the illumination. Both levels show the tendency to saturate and can reversibly be changed through the application of an appropriate treatment; the enhancement

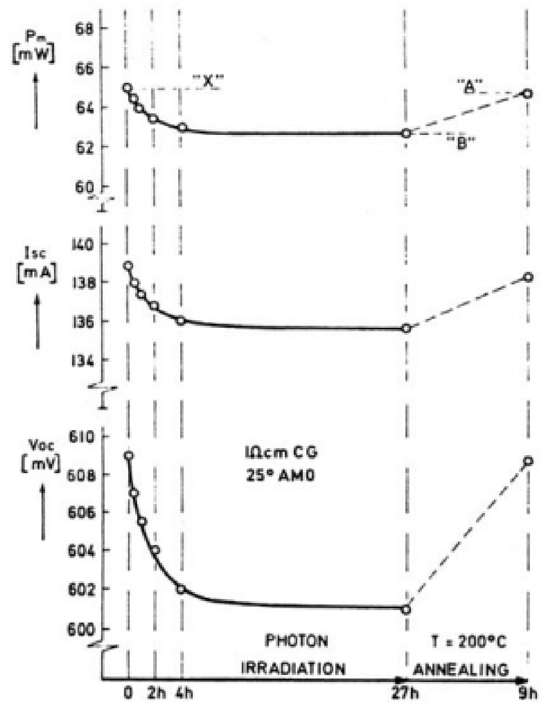

Figure 5.1: Effects of LID and recovery on the generated power short circuit current and open circuit voltage of a solar cell[29]

of the lifetime through this annealing step influences directly the solar cell parameters, as shown in figure 5.1. Thus after light-induced degradation the previous performance of the solar cell can be fully recovered through this annealing step.
In chapter 7 the results of some recovery experiments will be presented. In particular the effect of certain parameters on the recovery process, such as the presence of charge on the surface of the wafer or the passivation type, will be examined on the basis of the experimental results.

5.1.2 Light activated copper defects

Some publications[26] revealed a direct experimental evidence that the minority-carrier lifetime degradation has a clear dependency on copper concentration, regardless of the silicon material and the concentration of boron and oxygen in the bulk, implying that LID can occur solely due to copper. These results have also demonstrated that the saturation value of the lifetime at the end of the process is strictly dependent upon the copper concentration level. In order to estimate the influence of copper concentration on the decay of the lifetime during illumination, various experiments have been carried out obtaining the results summarized in figure 5.2.

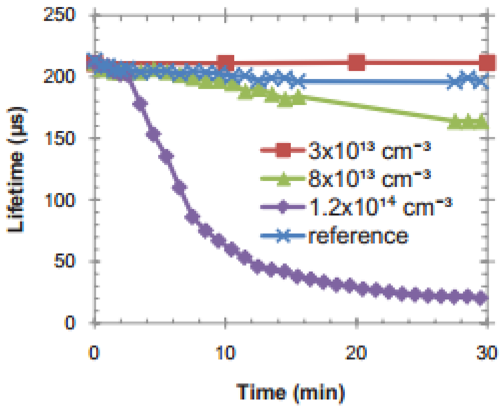

Figure 5.2: LID in a p-type FZ wafer as a function of illumination time. Note that when the copper concentration is below a certain threshold the lifetime does not show any degradation [26]

The figure shows that there is a threshold level for copper contamination: light illumination does not affect the lifetime when the copper concentration is under $3{\cdot}10^{13}\ cm^{-3}$. In addition other experiments showed that in oxygen-free samples the same copper concentration results in a slower defect reaction than in CZ wafers. Furthermore if the copper concentration results to be higher than the threshold, the copper contaminants precipitate causing an initial degradation that takes place prior to the illumination step.

In order to explain the LID process by means of copper, an electrostatic model can be considered; in particular the light activation reduces the electrostatic repulsion between positively charged interstitial copper ions and copper precipitates[26]. The reduction of this repulsion enhanced by illumination allows copper to precipitate in the wafer bulk even at a lower concentration level. As a consequence, the precipitation of additional amounts of copper and the formation of other precipitates increases the recombination activity. Thus the existence of a threshold for LID process is explained through the introduction of the nucleation barrier for the formation of copper precipitates explained in chapter 2. Copper precipitates were shown to be positively charged in p-doped silicon and neutral in n-doped silicon: as soon as the Fermi level exceeds the electroneutrality level for this kind of defects(located at $E_c - 0.2eV$), the charge state of copper precipitates changes from positive to negative so that the electrostatic precipitation barrier disappears or changes sign to attraction; this phenomenon explains the reason why the detrimental effect of copper results to be more evident in n-type samples than in the p-type counterparts.

In summary we can conclude that there are two processes that take place at the same time in CZ wafers: the formation of boron-oxygen complexes and the light-induced precipitation of copper atoms in the bulk. In the next paragraph different strategies for the reduction of LID will be examined; since these techniques can reduce only one of processes that occur during LID, a combination of these different techniques must be employed for the reduction or the complete removal of LID process.

5.2 Reduction of LID

5.2.1 Substitution or reduction of boron

As already stated, boron is one of the major components that gives rise to metastable defects through the generation of boron-oxygen complexes. Boron can be reduced or substituted by using:

1. High-resistivity boron-doped material(reduction of the dopant material);
2. Use of n-type silicon;
3. Gallium-doped silicon;

Unfortunately the first two options do not represent a valid solution since the use of n-type bulks implies that the standard fabrication steps must be changed, whereas a high-resistivity bulk affects the overall efficiency of the solar-cell, since it drastically increases the parasitic resistances of the model shown in the picture. Gallium-doped silicon represents a valid alternative since the solar cells parameters are apparently not affected by the choice of the dopant material. The use of gallium as dopant implies a problem with dopant homogeneity, as the segregation coefficient is very low causing a loss in efficiency potential for some parts of the ingot[30]. Thus instead of changing the dopant, in the next paragraph we have followed another approach consisting in some methods that should prevent the formation of boron-oxygen complexes and at the same time eliminate the defects introduced by the diffusion of copper atoms. This way the doping techniques of the wafers, on which the solar cell will be fabricated, are not modified so that only few steps must be added to the fabrication process in order to reduce the parasitic phenomena that give rise to the LID.

5.2.2 Herguth's method[30]

As already stated, after illumination boron-oxygen defects change from an inactive state to an active state causing an evident decrease of the lifetime. For avoidance of boron-oxygen related degradation, the disadvantageous interaction between boron and oxygen must be prevented. In order to understand this method for the prevention of these boron-oxygen complexes a *three-state model* has been introduced: the formation and annihilation of the complexes responsible for degradation can be described as a chemical reaction of microscopic systems from a recombination inactive state A to a strongly recombination active state B.

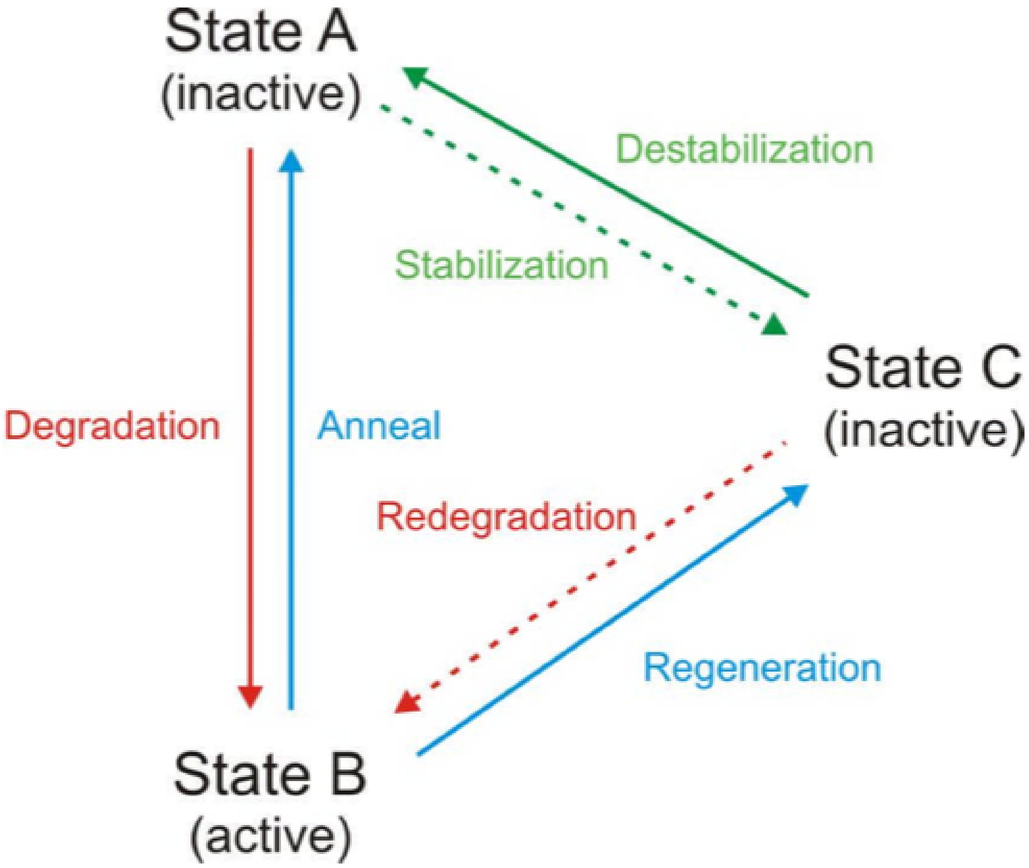

Figure 5.3: Three state model that describes the principle at the basis of Herguth's method: introduction of an intermediate state C which results less recombination active as state B and stable regarding a reaction to state A and B under the typical working conditions of the solar cell[30]

Particularly a transformation from state A to state B is caused by degradation, whereas the inverse process(from state B to state A) is achieved through an annealing step(paragraph 7.1.3). Degradation, as well as annealing, are therefore a representation of the two non-equilibrium states of the system. One way of limiting

degradation is to disturb this equilibrium by introducing a third state C, which is an intermediate state, i.e. less recombination active compared to state B. A scheme of the following process is shown in figure 5.3.
State C is reached through an annealing step at low temperature(120 °C) and exposure of the sample to the illumination.
A model has been proposed in order to explain the formation of the boron-oxygen complexes and their transformation into inactive recombination centers[30]. According to this model, a fast-diffusing oxygen dimer O_{2i} and an immobile substitutional boron atom B_s react giving rise to the following process

$$B_s + O_{2i} \longleftrightarrow B_sO_{2i} \tag{5.1}$$

Introducing a side defect reaction involving a complex XY of unknown composition, the model proposes that XY dissociates into its components X and Y and one of the components forms a recombination- inactive complex XO_{2i} with the highly mobile oxygen dimer, leading to the following reaction

$$X + O_{2i} \longleftrightarrow XO_{2i} \tag{5.2}$$

Since the concentration of free oxygen dimers is reduced, the equilibrium of reaction 5.1 requires that more B_sO_{2i} complexes dissociate, hence the number of recombination-active B_sO_{2i} complexes is reduced.

5.2.3 Charge deposition

The techniques that were described in the previous paragraphs allow the reduction of boron-oxygen defects, whereas they do not have any effect on those introduced by copper diffusion. In this section different approaches for the elimination of copper-introduced defects will be discussed. It is clear that many parameters can be varied in order to reduce the LID phenomenon: along with the reduction or the substitution of boron with other dopant materials, the passivation type or the charge deposition on the wafer surface play an important role on the LID process, since they allow the removal of copper defects from the bulk leading to the separation of the phenomena that contribute to the LID process.

5.2.3.1 Silicon dioxide passivation

Silicon dioxide is the simplest passivation type, as pure silicon atoms naturally react with oxygen molecules giving rise to SiO_2 layers. In order to enhance the chemical reaction, the wafers are introduced into specific furnaces where the temperatures can be up to 1000°C(see chapter 6). Silicon dioxide passivation does not contain any charge, therefore after the growth of the passivating layer the net charge of the wafer is substantially neutral. Since copper ions in the silicon bulk are positively charged, the deposition of surface negative charge allows the attraction of copper interstitial ions towards the surface leading to the separation of copper defects and boron-oxygen complexes, as depicted in figure 3.

(a) Neutral wafer (b) Negative charge deposition

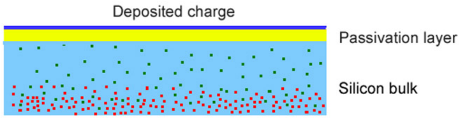

(c) Positive charge deposition

Figure 5.4: Effects of charge deposition (Red dots indicate copper interstitial defects, whereas green dots represent boron-oxygen complexes); the deposited negative charge attracts copper defects towards the surface, whereas the positive charge is expected to repel copper ions from the sample surface

On the other hand, the deposition of positive charges repel copper ions from the surface creating the accumulation of defects in the bulk. Thus according to these speculations, after the deposition of positive charge the degradation of the lifetime should result worsened as two different light-activated phenomena take place at the same time.

5.2.3.2 Aluminum oxide

A material that has recently gained interest for the passivation of silicon wafers is aluminum oxide(Al_2O_3) grown by ALD(atomic layer deposition) which provides an excellent level of surface passivation on p-type wafers. This type of passivation results particularly interesting for the reduction of the LID process because it contains some negative fixed charge which results particularly useful for the attraction of copper defects towards the surface, analogously to what has already been shown in figure 5.4b. The origin of these negative charges is most probably related to the presence of aluminum vacancies in the passivating layer; in practice the presence of inner defects in the lattice structure of the passivating layer creates an uncompensated negative charge which acts in the same way as the charge intentionally deposited by using charging machines(e.g. corona charging). Particularly these defects are substantially generated by oxygen vacancies that introduce some defect levels in the band gap occupied by electrons, so that the resulting net charge is negative[31]; in other words intrinsic defects in aluminum-oxide are stable in their fully ionized charge states. Although some other electronic defects may be induced in order to compensate defect charge imbalance, this phenomenon is usually considered negligible so that aluminum-oxide layers usually contain a considerable amount of negative charge. In chapter 7 experimental results concerning the LID-process of Al_2O_3-passivated samples will be presented so that the previous hypothesis regarding the presence of negative charge in the passivating layer will find an experimental proof.

Chapter 6

Samples preparation and measurement equipment

An accurate preparation of the samples is very important for the right evaluation of the experimental results. The repeatability of the experimental results is particularly important, since some random parasitic phenomena can deeply affect the results of a single experiment. In this work many samples were obtained from a single wafer and were passivated in the same chamber so that it can be assumed the all the samples have been prepared under the same conditions.
Before analysing the results concerning the LID process on monocrystalline silicon, a brief introduction to the equipment that has been used for preparation of the sample and the measurement set for the lifetime scanning is needed to give a further insight into the whole experimental work.

6.1 Cleaning

The starting material is represented by mono-crystalline silicon wafers with orientation <100>. This wafers had already been cut from the ingot and polished by the supplier, therefore the initial step for the preparation of the wafer is represented by a cleaning phase which is aimed at removing the raw material which is usually present along the wafer surface. The starting wafers, indeed, usually contain a high concentration of contaminants that strongly reduces the measured lifetime; in addition silicon usually reacts with oxygen giving rise to a native silicon dioxide layer. Before the growth of the passivating layer, both the raw material and the native oxide layer must be removed so that the recombination activity through defects introduced by contaminants can be sensibly reduced and a sufficiently thick oxydation layer can be grown on a pure substrate; figure 6.1 shows a

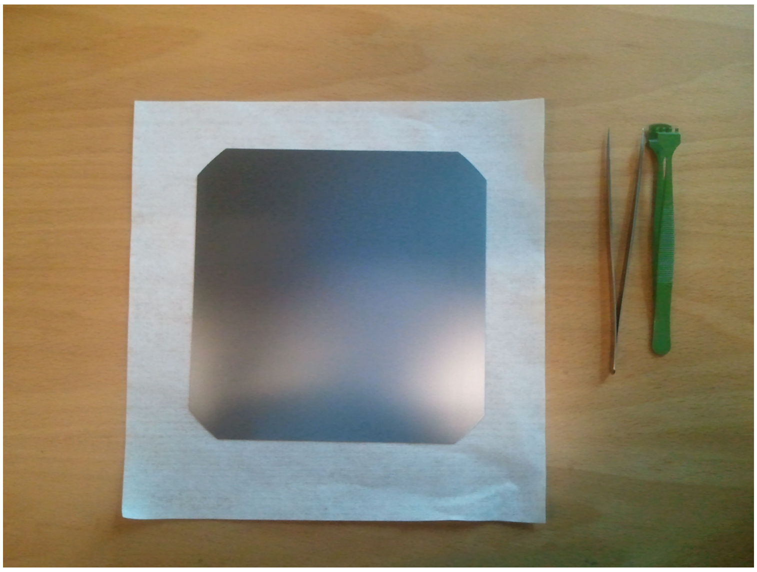

Figure 6.1: Raw wafer before etching

silicon wafer before the etching process. The cleaning was performed by RCA1 solution, 1:1:5 of NH_4OH (ammonium hydroxide) + H_2O_2 (hydrogen peroxide) + H_2O (water) at 80 °C, followed by HF dip for 2 minutes. The first step (called SC-1, where SC stands for Standard Clean) is performed with a 1:1:5 solution of NH_4OH (ammonium hydroxide) + H2O2 (hydrogen peroxide) + H2O (water) at 75° or 80°C. This treatment usually takes 10 minutes and results in the formation of a thin silicon dioxide layer on the silicon surface, containing a certain degree of metallic contamination (notably Iron) that shall be removed in subsequent steps. The final step is a short immersion in a 1:50 solution of HF + H_2O at 25 C, in order to remove the thin oxide layer and some fraction of ionic contaminants.

6.1.1 Etching

In some wafers after the cleaning process the lifetime of the samples resulted too low so that a new etching process was needed in order to remove a further layer of raw material that the previous cleaning process had not removed. The etching was performed using a solution made up of HNO_3, HF and CH_3COOH in the ratio of 75:8:17 at 25°C. The resulting etching rate is about 5μm/min and the etching process took 8 minutes, therefore the thickness of the etched layer resulted 40μm(20 μm each side)[33]

6.2 Growth of silicon-dioxide passivation layer

The passivation layer has been grown through an oxidation and annealing furnace which contains four programmable process tubes for diffusion and oxidation of silicon wafers. The maximum allowed diameter for each sample is 100 mm.

Figure 6.2: Oxidation furnace(clean room equipment)

The oxidation process is dry, i.e. it is obtained through the emission of gas flow containing oxygen molecules in a furnace whose temperature profile is summarised in the table below. After the oxidation, the sample were annealed in nitrogen at a higher temperature(950°C).

Load temp	Ramp up(10 min)	Oxidation (40 min)	Ramp up	Annealing temp	Ramp down
800°C	10°C/min	900°C	10°C/min	950°C	4°C/min

Table 6.1: Oxidation process: the process starts at 800°C and ends at the same temperature after a decreasing ramp temperature

At the end of the oxidation process the thickness of the oxide passivating layer results to be equal to 15 nm.

6.3 Growth of aluminum-oxide passivation layers

6.3.1 Operation principle of the reactor

A schematic view of the cross-section of a typical ALD reactor is presented in the picture below. The working principle can summarized in few steps:

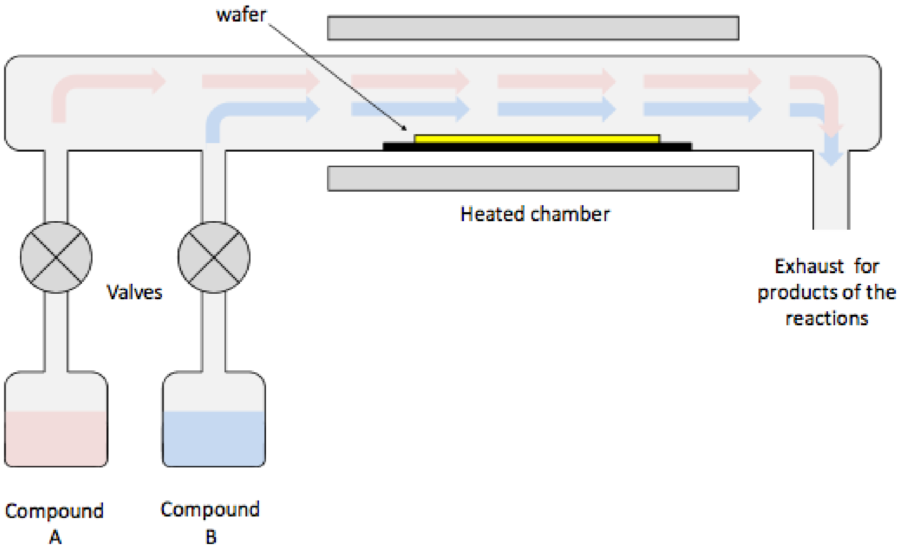

Figure 6.3: Cross section of a typical ALD reactor: the precursors are kept in two separate chambers and their flux is regulated by a specific valve; these precursors are pulled along the chamber by an inert gas. The sample is place on a hot plate in order to enhance the chemical reaction on its surface

- The precursors are kept in two separated chambers at controlled temperature;
- Each chamber is separated from the reaction chamber through a valve whose operation is controlled by an external electronic circuit;
- The wafer is placed in the middle of the chamber on a heated support. Note that the chamber is kept in vacuum, obtained by using an external pump; the chamber must be as small as possible in order to minimize the time needed for the production of high vacuum.
- An inert gas, that is used for the transport of the precursors, is injected and removed from the chamber through a pumping system. In order to stabilise the pressure of the chamber the pumping rate for the injection and the extraction of the gas are controlled by an external system.

The chemical reaction that takes place during the deposition is summarized in figure 6.4. The deposition process can be subdivided into several steps:

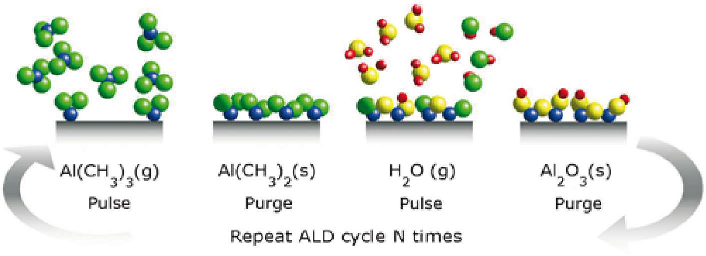

Figure 6.4: The process of atomic layer deposition can be summarized in 4 steps: injection of TrimethylAluminum into the chamber; bonding between TrimethylAluminum and the surface; water injection and extraction of the vapour products

- Injection of TrimethylAluminum, $Al(CH_3)3$, in the reaction chamber.
- A reaction involving TrimethylAluminum and the surface of the wafer takes place: the precursor chemically reacts and bonds to the surface without fully decomposing. The precursor also changes the dominant surface termination, leaving the surface ready to react with the co-reactant. The remaining vapour products are pumped or pushed out of the deposition zone using inert gas flow. The remaining vapor products are pumped or pushed out of the deposition zone using inert gas flow.
- Water vapour (H_2O) is injected in the reactor. A reaction with CH3-groups starts:

  $$2Al(CH_3)_3 + 3H_2O \rightarrow Al_2O_3 + 6CH_4$$
- The vapour products are flushed out. The starting hydroxylated surface is reproduced and the ALD cycle can start again.

The characteristic feature of an ALD process is that the half-reactions are self-limiting: once the precursor has reacted with sites prepared during the previous co-reactant exposure, the surface reaction stops, that is, the surface sites prepared by the precursor reaction are reactive to the co-reactant, but not the precursor itself. This means that during steady-state growth, the precursor will typically deposit only one monolayer during each half-reaction cycle, even when the surface is exposed to the reactant species for long periods of time.

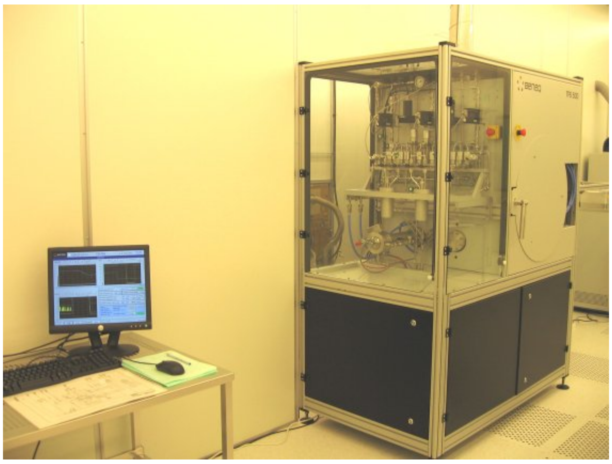

Figure 6.5: Atomic layer deposition equipment(clean room)

6.3.2 Layer Deposition

ALD deposition technique is operated through a reactor designed for oxide and nitride film deposition.
The reactor used for the preparation of aluminum-oxide passivated samples includes:

- Four liquid precursors: H_2O, TMA, $TiCl_4$ and $DEZn$
- Three precursor gases: NH_3, O_2 and O_3

The carrier gas for the transport of the precursors is represented by N_2 or Ar.

6.4 Corona charging

A Corona Charge Generator was used for the deposition of negative and positive ions on insulator materials. The built-in hot-chuck and air-cushion system makes possible 25-300 °C annealing of wafers. The main purpose of the equipment is to charge up oxidised silicon wafers of up to 8 inch diameter in an accurate and controlled way. Some of the characteristics of the corona charge generator are listed in the table below:

Needle voltage	Charge polarity	Charge amount	Accuracy
15kV	Positive/negative	1-99999 μC	0.1 μC

Table 6.2

After the charge deposition, the samples were kept in the dark for 24 hours so

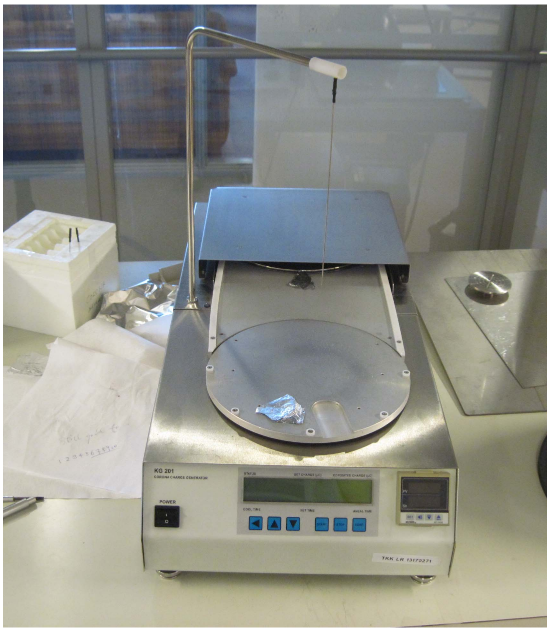

Figure 6.6: Corona charge generator: the charge is generated by the needle and deposited over the plate surface

that the copper ions can be attracted or repelled according to the polarity of the deposited charge.

6.5 Lifetime measurement

The technique used for the evaluation of the lifetime of the excited minority minority carriers has already been discussed in paragraph 4.2.1. The lifetime scanner used for the tracing of the lifetime maps that will be presented in the next chapter presents the following characteristics:

Microwave frequency	10.1-10.6 GHz
Irradiated power	40 mW
Laser	Pulsed InGaAs laser diode
Optical pulse width	200 nm
Wavelength	905 ±10 nm

Table 6.3: Technical specifications of the lifetime scanner

The maps were traced with a raster level of 1 mm: this means that the distance between one point and its neighbour is equal to 1 mm. This setting represents a compromise between measurement accuracy and its time duration: in practice the higher is the resolution and the longer the measurement takes to be completed.

Some measurements present some extra-points with a very high lifetime which lay outside the silicon surface of the samples. In order to evaluate the correct average lifetime on these samples, these “fake” points are subsequently discarded through the use of an apposite MATLAB script.

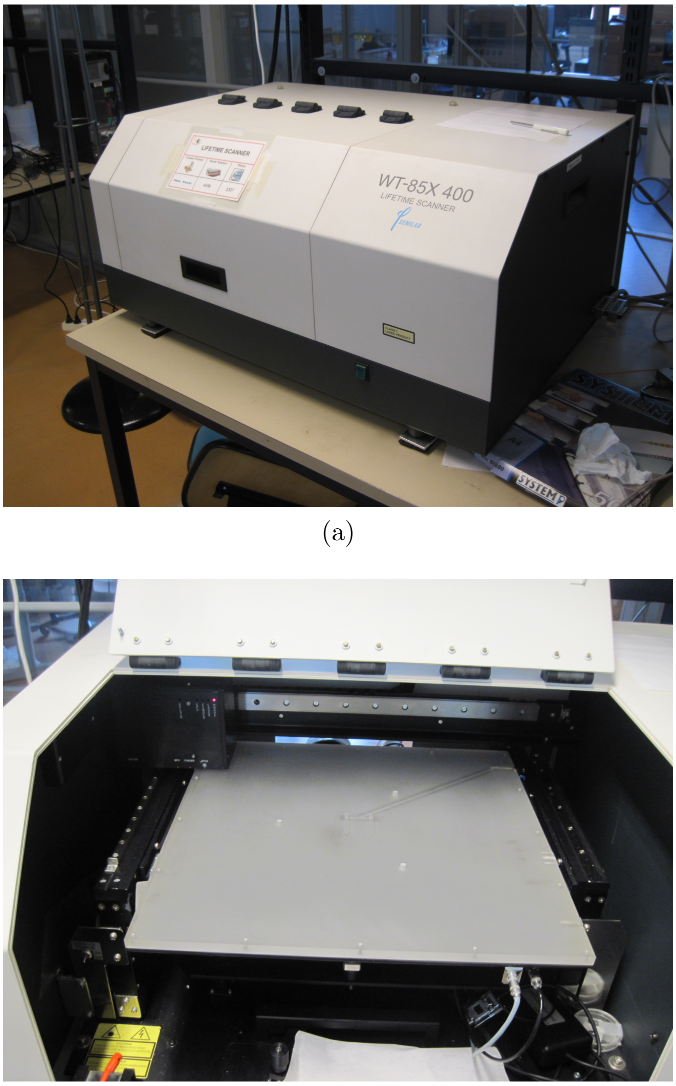

(a)

(b)

Figure 6.7: Lifetime scanner: the probe initially performs a *pre-scan* in order to identify the edges of the sample and subsequently it starts the point-by-point detection of the lifetime across the sample surface

Chapter 7

Experimental Results

This chapter will present the results concerning all the experiments that were carried out at Micronova laboratory. The experimental work has been divided into two parts: the former is related to the first experiments performed on samples provided by a supplier from Finland and the latter concerns the same experiments completed on other samples provided by a supplier from United States. All the experiments carried out on these samples can be grouped into three different categories:

- **LID experiments**: illumination of the samples at room temperature for at least 24 hours and measurement of the lifetime at constant time intervals;
- **Herguth method test**: illumination and annealing at 120 °C until the lifetime is stabilized, then illumination at room temperature
- **Recovery**: this experiment consists in a short annealing at 200 °C in order to enhance the lifetime of the silicon samples.

The material used for these experiments is monocrystalline silicon with a sufficiently high p-type doping level in order to enhance the conductivity. The resistivity of the first set of samples resulted to be included in the range from 2.2 to 2.8 $\Omega \cdot cm$ with a declared oxygen concentration of 15.3 ppma. For the second set the resistivity resulted to range from 1 to 2 $\Omega \cdot cm$ resulting slightly lower compared to the first experiment set, whereas there are no available information about the oxygen content.

For all these experiments there are some degrees of freedom that require an experimental investigation; for instance several parameters, such as the amount of deposited charge, the passivation layer and the copper contamination, must be varied in order to analyse their impact on the degradation process. Subsequently these results have been interpreted in accordance to the theoretical models that were introduced in chapter 5.

7.1 First experiment set

7.1.1 Impact of LID on lifetime

This paragraph is aimed at the evaluation of the effect of illumination on the effective lifetime of silicon wafers passivated with silicon dioxide. The degradation of the lifetime along the wafer surface is illustrated in figure 7.2. We can immediately notice that there is a steep decrease of the lifetime during the first hours of illumination due to the considerable degradation of the region which shows the highest lifetime(the blue region that appears in figure 7.2a) during the initial hours. This process progressively slows down until a saturation level is reached; in that region, in fact, after 17 hours the lifetime appeared to remain substantially stable. On the contrary, the regions along the edges suffer a longer degradation; the lifetime, indeed, resulted to be completely stabilised only after 24 hours of continuous illumination.

The trend described by the average lifetime is shown in figure 7.1.

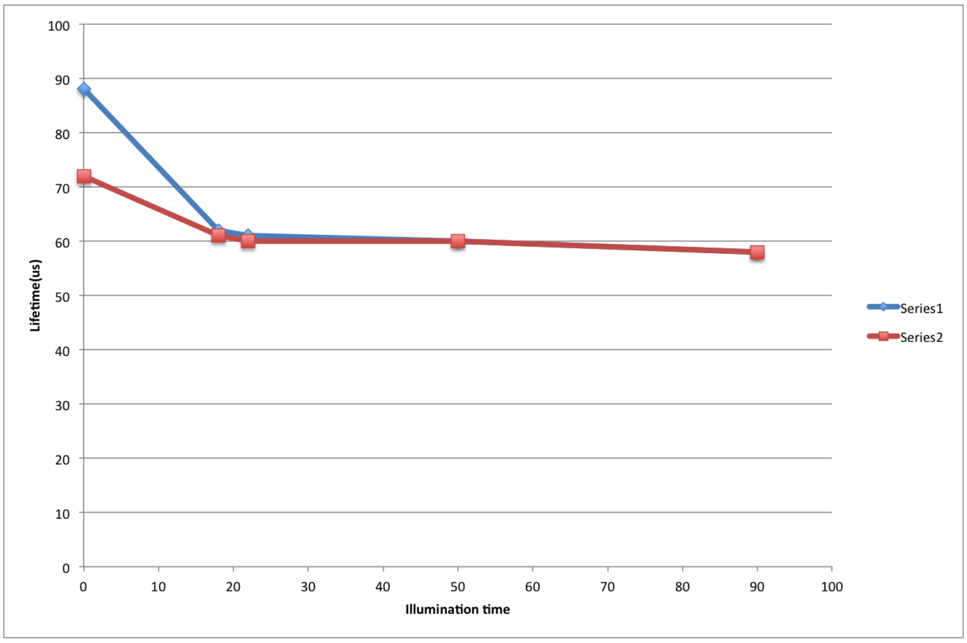

Figure 7.1: Degradation of the average lifetime: the measured value follows a steep decrease until a precise saturation level has been reached. It is possibile to demonstrate that the decay can be described through an exponential function(see picture 7.3) described by equations 7.1 and 7.3

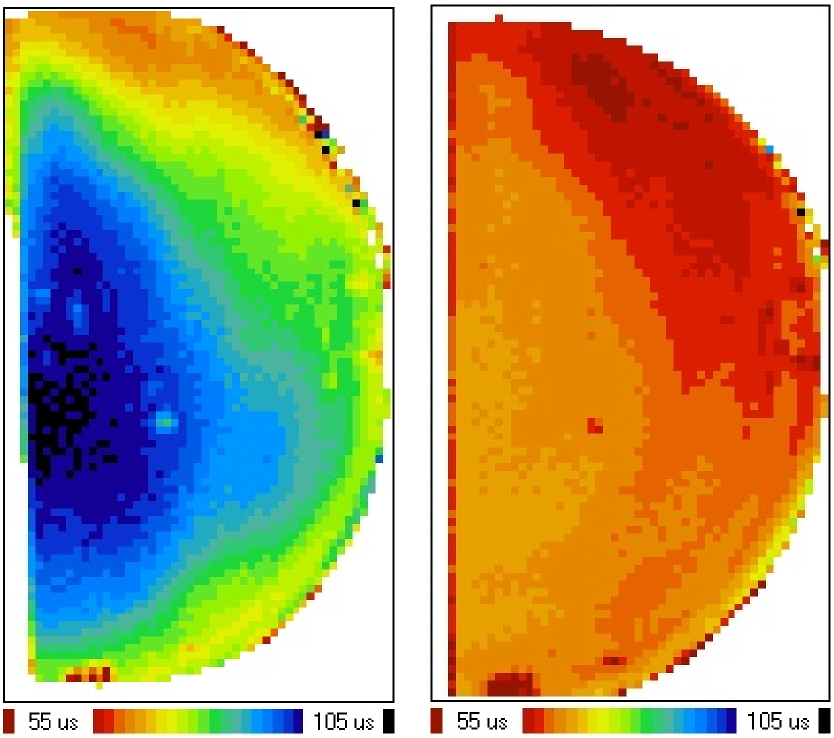

(a) 0h (b) 17h

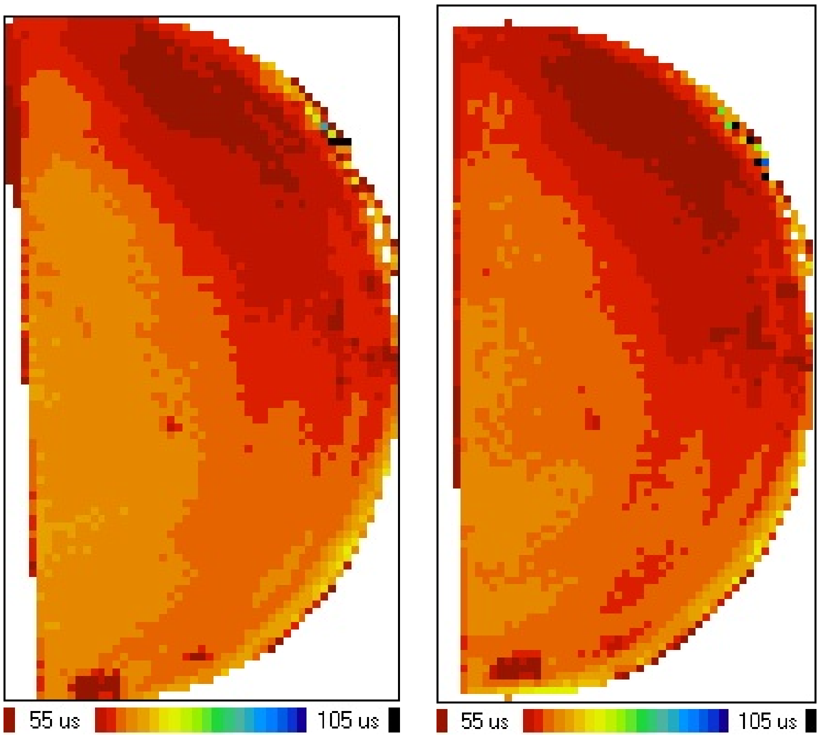

(c) 24h (d) 47h

Figure 7.2: Lifetime distribution maps of the samples whose average lifetime has been reported in figure 7.1; it is possible to notice that the degradation process is stronger in those regions where the initial lifetime resulted very high.

The lifetime measurements shown in figure 7.1 and figure 7.2 refer to two samples obtained from the same wafer and exposed to the same light spot.

Some models for the description of lifetime degradation induced by the formation of boron-oxygen complexes were presented in literature. One of the most interesting started from the assumption that that the light induced defects are totally activated under illumination and their initial concentration at the beginning of the LID process is negligible[26], so that the degradation of the lifetime follows an exponential decay described by the following equation[26]

$$\tau(t) = \frac{\tau_0}{1 - e^{-\frac{t}{\tau_c}}} \tag{7.1}$$

where

$$\lim_{t \to 0} \tau(t) = \infty \quad , \quad \lim_{t \to \infty} \tau(t) = \tau_0 \tag{7.2}$$

The assumption that there is no defect concentration at the beginning of the degradation process is never met in practice; indeed if the defect concentration were equal to 0, the initial lifetime would be very high, tending to infinite as demonstrated by equation 7.2. As can be noted from figure 7.1, the initial lifetime is the highest measured value but the order of magnitude is the same for all the measured lifetimes. Equation 7.1 thus can be modified by introducing a correction factor in the argument of the exponential function, i.e.

$$\tau(t) = \frac{\tau_0}{1 - e^{-\frac{t}{\tau_c} + \mu}} \tag{7.3}$$

so that

$$\lim_{t \to \infty} \frac{\tau_0}{1 - e^{-\frac{t}{\tau_c} + \mu}} = \tau_0 \quad , \quad \lim_{t \to 0} \frac{\tau_0}{1 - e^{-\frac{t}{\tau_c} + \mu}} = \frac{\tau_0}{1 - e^{\mu}} = \tau_i \tag{7.4}$$

where τ_i is the initial lifetime at the end of the degradation process. Using the non-linear fitting techniques some parameters, such as μ and τ_c have been extracted from the experimental results through the use of the fitting techniques. The results of the fitting are grouped in the table below.

Sample 1		Sample 2	
τ_c	18.2	τ_c	9
μ	1.5	μ	1.1

Table 7.1: Extrapolation of the parameters introduced in eq.7.3 through the use of fitting techniques. It is possible to notice that Sample 1 presents a decay which is twice faster than Sample 2. However the saturated lifetime resulted the same for both the two samples, as shown in figure 7.1

The fitted exponential curves are shown in figure 7.3. We can immediately notice that the degradation process is accurately fitted by the B-O degradation model at a rate determined by the paramater τ_0. Particularly we can notice that sample 1 showed a higher initial lifetime that saturated at the same lifetime as sample 2. The generation rate of the defects, therefore, results to be higher in sample 1, as it results clear from the values shown in table 7.1.

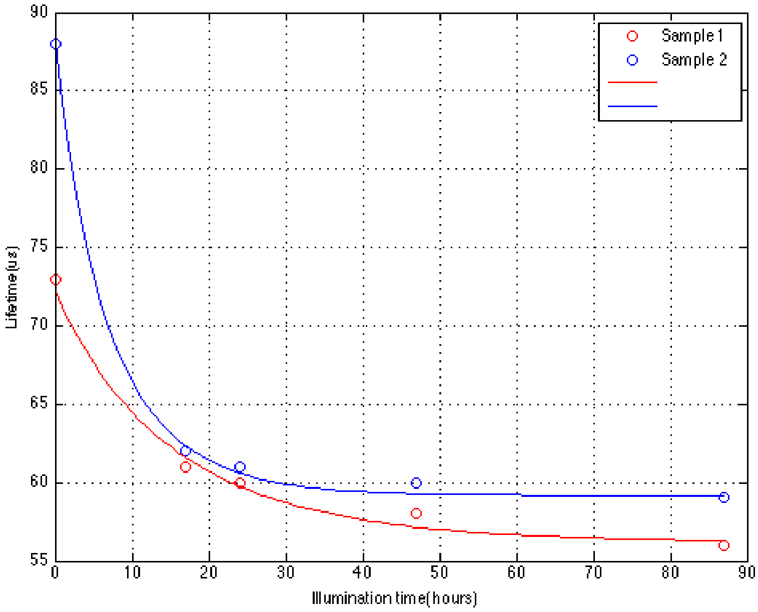

Figure 7.3: Graphical representation of the fitted curves; the overlapping between the fitted values and those predicted by the fitted curves substantially confirms the validity of equation 7.3

7.1.2 Effects of deposited charge on LID

In order to analyse the behaviour of the samples after charge deposition, two samples were charged with different amounts of charge(-900 μC and +300μC) and then exposed to the same light spot at room temperature. The results of this experiment are presented in figure 7.4.

As we can see from the figure, the deposited charge has no effects on the decay of the lifetime, confirming the hypothesis that on these samples the light-induced degradation process is mainly due to the formation of boron-oxygen complexes. This assumption is partly confirmed also by the results shown in the previous paragraph, since the exponential function describing the lifetime decay is related to the formation of defects generated by boron-oxygen complexes.

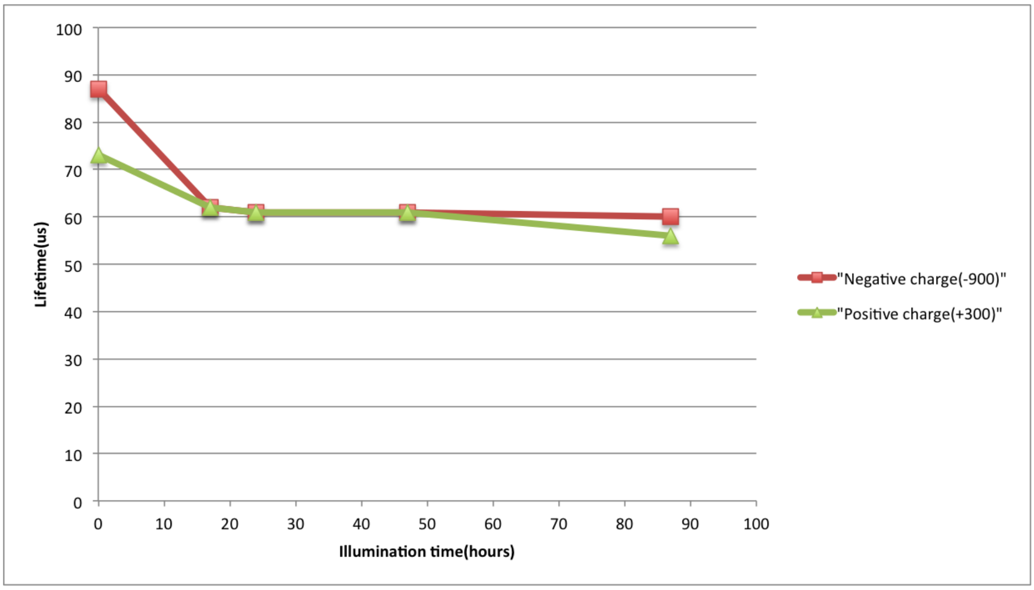

Figure 7.4: Degration of the average lifetime on charged samples: it is clear that the deposited charge has no effect on the degradation process confirming the hypothesis that the decay is dominated by the formation of boron-oxygen complexes rather than the copper-introduced defects

7.1.3 Lifetime recovery

Before illustrating the results of Herguth method, some experiments regarding the recovery of the lifetime will be presented as they represent one of the preliminary steps for Herguth method. As already mentioned in the previous chapters, the recovery process consists of a short annealing(15 minutes) at a low temperature(200°C) and produces a considerable enhancement of the lifetime in the areas where the initial lifetime is not too low. It has been reported [35] that annealing has a positive effect on the overall lifetime, as it causes the dissociation of the boron-oxygen complexes thus reducing the total concentration of the defects. However subsequent illumination at room temperature completely degrades the lifetime again, therefore this recovery process is used only to enhance the initial lifetime of the samples, without producing any effect on the degradation process.
The results of the recovery experiments are shown in table 7.2.

Recovery with no charge		
Initial lifetime(μs)	Final lifetime(μs)	Gain(μs)
37	102	65
54	132	78
39	102	63

Table 7.2: Measured average lifetime on neutral samples(no charge) before and after the recovery

The effects of charge deposition on the effectiveness of the recovery process have been analysed obtaining the results presented in table 7.3.

+300 μC surface charge deposition		
Initial lifetime(μs)	Final lifetime(μs)	Gain
68	120	52
64	117	53
54	101	47
13	35	22
34	60	26
+600 μC surface charge deposition		
64	93	29

Table 7.3: Measured average lifetime on positively charged samples(+300 and +600 μC) before and after the recovery; the lifetime gain remains comparable to the values grouped in the previous table

Clearly it results that positive charge does not affect significantly the enhancement of the lifetime. On the other hand, the negative charge produced the following results:

-300 μC surface charge deposition		
Initial lifetime(μs)	Final lifetime(μs)	Gain
64	45	-19
59	48	-11
-600 μC surface charge deposition		
49	37	-12
-900 μC surface charge deposition		
57	36	-21

Table 7.4: Measured average lifetime on positively charged samples(-300, -600 and -900 μC) before and after the recovery; the lifetime gain becomes negative, showing that the presence of negative charge produces an opposite effect on the effectiveness of the lifetime recovery

Quite surprisingly the negative charge resulted to has an opposite effect on the lifetime: while on neutral and positively charged samples this procedure produced a significant increase of the lifetime, negative charge produced a negative effect on the recovery , even causing a decrease of the lifetime after the recovery. A graphical overview of the results shown in the previous tables is presented in figure 7.5.
In order to deeply analyse the effect of recovery on the distribution of the lifetime as a function of the deposited charge, in the following figures some maps regarding the distribution of the lifetime in samples with a different deposited charges have been included.

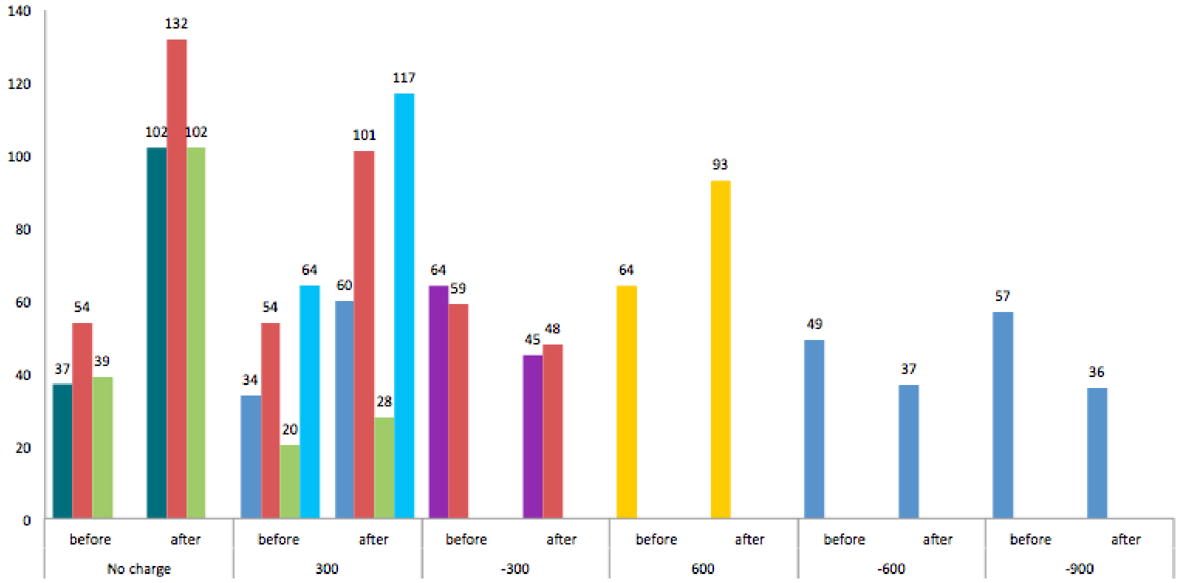

Figure 7.5: Graphical representation of the values shown in the previous tables; again it is possible to appreciate the detrimental effect of negative charge on the lifetime recovery

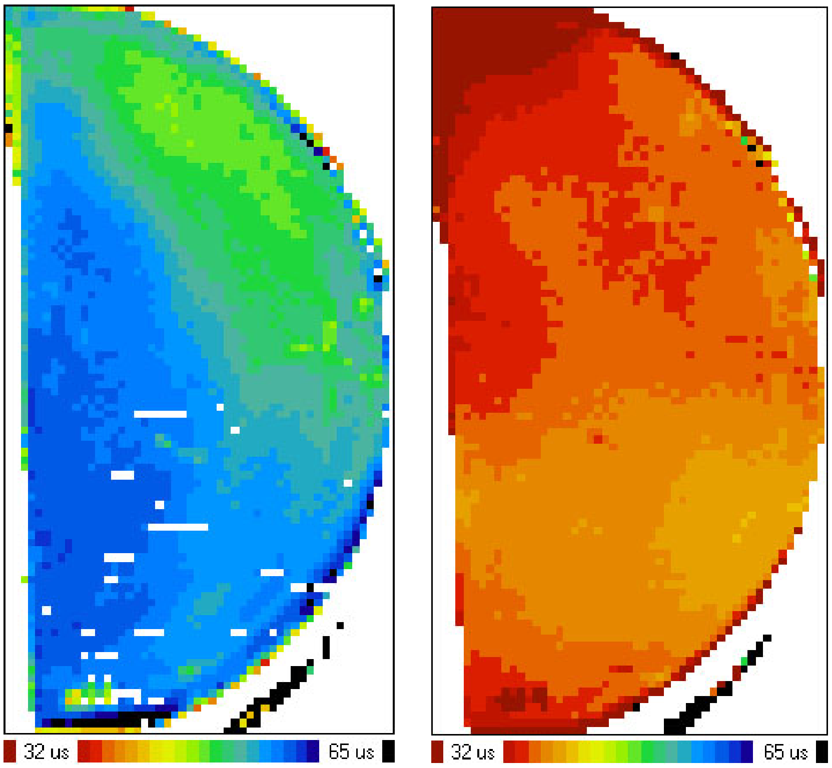

(a) Before recovery (b) After recovery

Figure 7.6: Lifetime distribution map on negatively charged samples before and after recovery; it is evident that the reduction of the lifetime involves the whole sample.

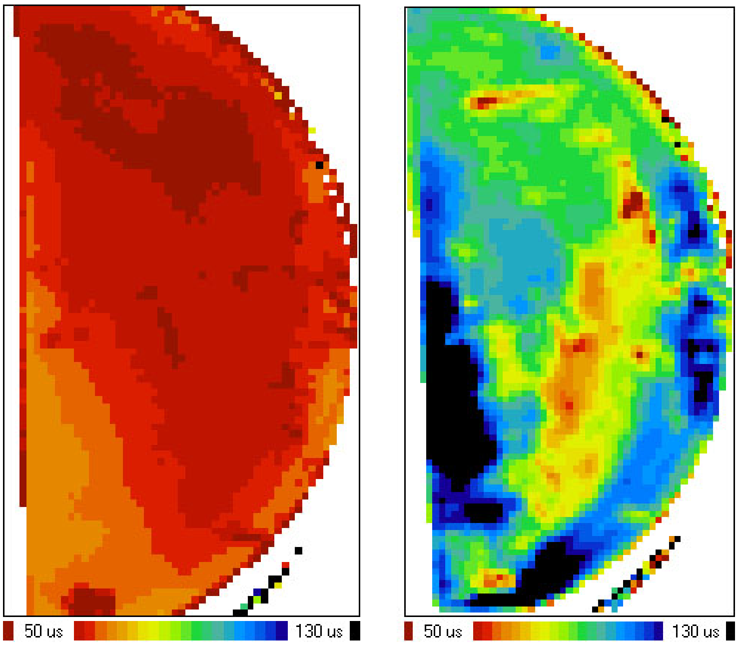

(a) Before recovery (b) After recovery

Figure 7.7: Lifetime distribution map on positively charged(+300 μC) samples before and after recovery; we can notice that the lifetime gain is rather uniform throughout the sample surface, thus those regions where the final lifetime resulted higher(marked with blue) correspond to the orange areas in figure 7.7a

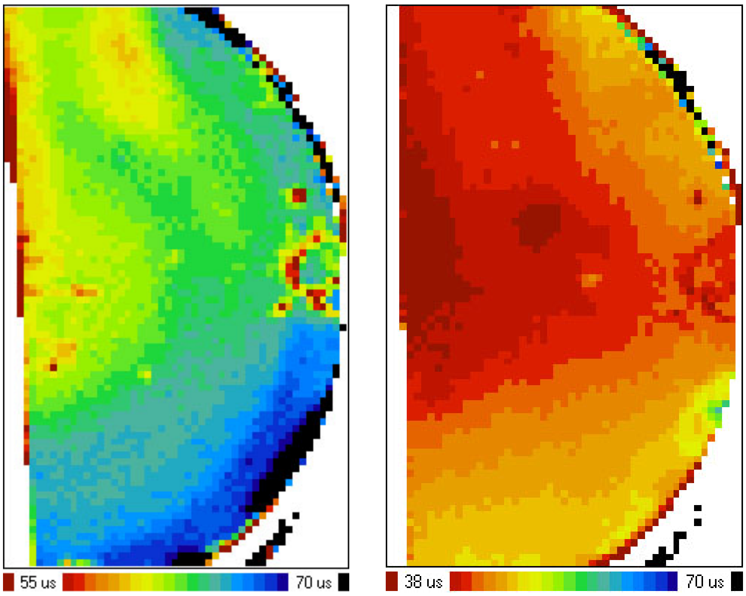

(a) Before recovery (b) After recovery

Figure 7.8: Lifetime distribution map on negatively charged(-900 μC) samples before and after recovery; again the lifetime gain appears to be rather uniform throughout the sample surface, even though the negative charge produced an opposite effect on the lifetime gain

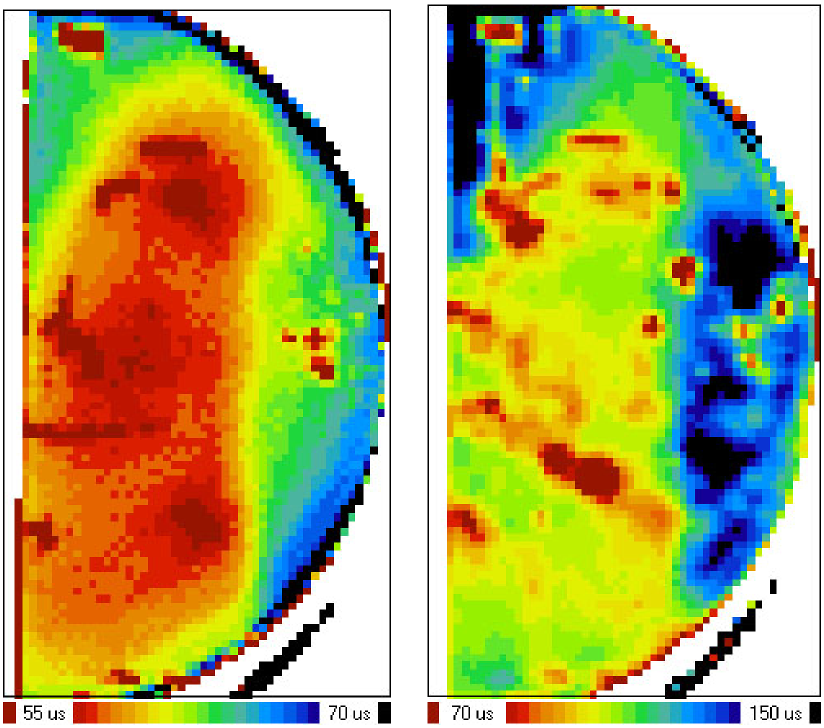

(a) Before recovery (b) After recovery

Figure 7.9: Lifetime distribution map on positively charged samples before and after recovery(+900 μC)

As we can notice from the previous maps, the enhancement of the lifetime is extremely strong in the areas with the highest lifetime. Particularly on the samples with positive charge the total lifetime effectively increased throughout the sample surface resulting nearly twice the initial value. The effect of negative charge, on the other hand, resulted to be an effective "lifetime killer", since the recovery process produced a sensible reduction of the lifetime. Moreover the variation of deposited charge did not produce significant effects on the final result: the enhancement of the lifetime resulted to be approximately the same, both with +300 μC and +900μC.

In order to give an hypothetical explanation of these experimental results, we can consider the model proposed by V.Voronkov and R.Falster[38]. According to this model, the defects are transformed from a LC state(low recombination activity state) to SRC(recombination active center) and viceversa. Within this scenario, the degradation starts from a latent complex(LC) $B_sO_{2i}^+$ that involves an interstitial boron atom B_i. During illumination the photogenerated carriers recharge the latent complexes into the neutral state which acts as a SRC defect. Eventually when the recovery process is completed, the SRC complexes are first reversed into the positive charged latent state($B_sO_{2i}^+$) and then recombined with the surface intentionally deposited negative charge giving rise again to neutral complexes B_sO_{2i}, which act as effective recombination centres.

7.1.4 Herguth's method

Since the lifetime degradation seemed to be caused by the formation of boron-oxygen complexes, Herguth's method appeared the best candidate for the reduction of LID. This method has been tested under different conditions, i.e. with different amounts of deposited charge and after a recovery/degradation cycle. The samples submitted to Herguth's method can be subdivided into two groups:

- **Clean samples**: absence of copper contamination;
- **Contaminated samples**: intentionally copper contaminated samples obtained by dipping the wafers in a solution containing 2 ppm copper concentration;

7.1.4.1 Clean samples with preliminary recovery and degradation step

On these samples Herguth's method was preceded by a recovery and degradation cycle, in which the lifetime was initially enhanced and subsequently reduced by exposing the samples to 1 Sun illumination. Unfortunately this method did not produce any significant result, as we can see from figure 7.10, since the illumination at room temperature produced a very strong degradation of the lifetime.

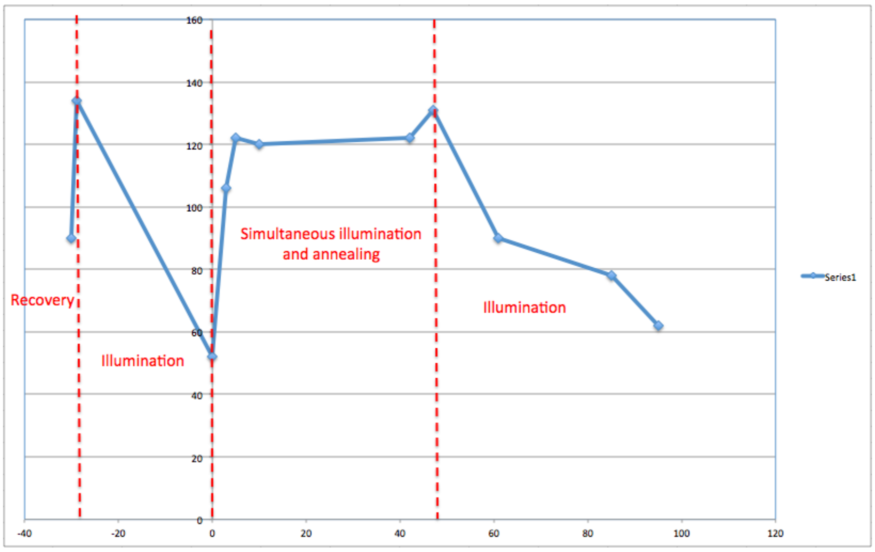

Figure 7.10: Herguth's method performed with a preliminary recovery and degradation cycle; the simultaneous illumination and annealing phase produces the stabilization of the lifetime but the subsequent degradation during the illumination at room temperature denotes a substantial failure of Herguth's method on this sample

The maps of the samples whose average lifetimes have been included in the previous picture, are shown below.

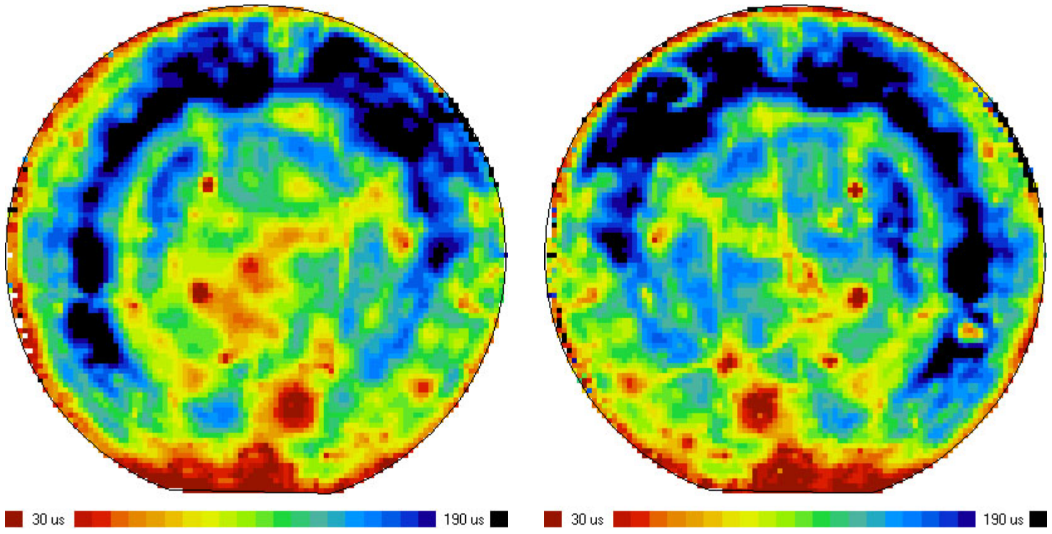

(a) Before Herguth's method (b) After Herguth's method

Figure 7.11: Lifetime distribution map

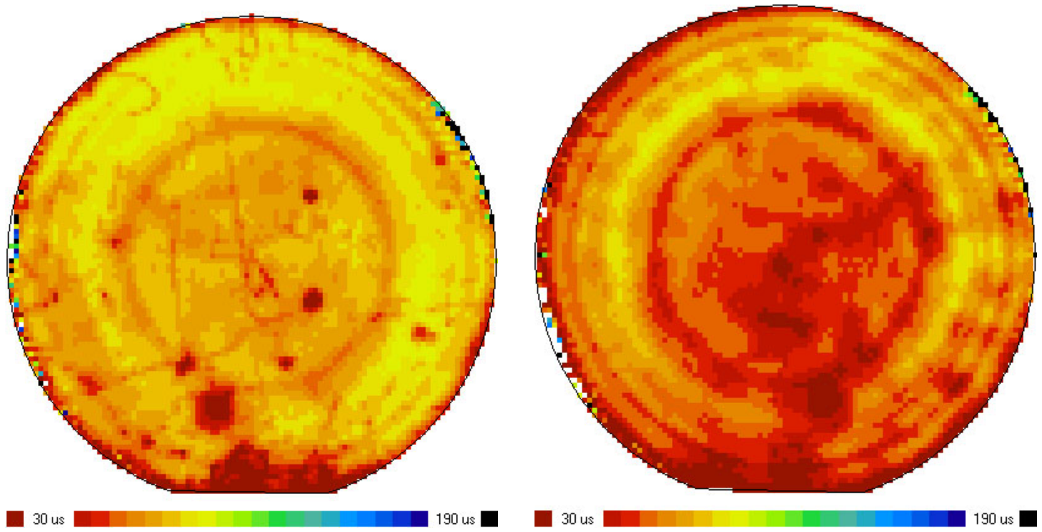

(a) After 20 hours (b) After 65 hours

Figure 7.12: Lifetime distribution map during illumination at room temperature: it is evident that the lifetime distribution across the surface is not stabilized; as we can see, the whole surface of the sample tends to saturate to the lowest lifetime value

As we can see from image 7.15, after Herguth's method and the illumination at room temperature, the lifetime distribution tends to come back to the initial value. The degradation is uniform throughout the measured surface; particularly we can notice a considerable increase of the lifetime during the annealing and illumination phase, which is considerably high in the areas with the highest initial lifetime. According to the data provided by the supplier, the material that constitutes these wafers can be considered extremely pure. Moreover these samples were not inten-

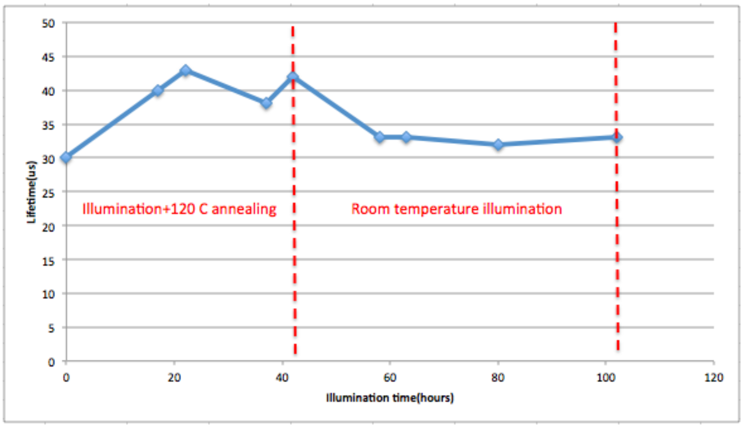

(a) Copper contaminated sample

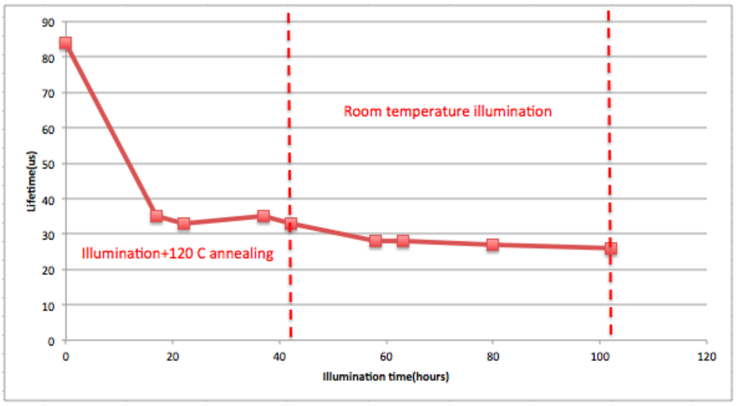

(b) Clean sample

Figure 7.13: Average measured lifetime of copper contaminated and clean samples. We can notice that on clean samples Herguth's method did not produce any effect, since the shape of the curve is decreasing monotonically until a saturation value; quite surprisingly on the copper contaminated sample Herguth's method produced an enhancement of the lifetime. Moreover the subsequent illumination phase caused a slight decrease of the lifetime and stabilization around a lifetime value which results higher than the initial one

tionally contaminated and no charge was deposited on the sample surface, hence the degradation during illumination at room temperature might be attributed to the formation of recombination active boron-oxygen complexes which were not successfully deactivated by Herguth's method.

7.1.4.2 Intentionally contaminated samples

In this paragraph some results obtained performing Herguth's method on copper contaminated wafers will be presented. In order to separate the effect of copper from the formation of boron-oxygen complexes, a certain amount of negative charge has been deposited on these samples. In practice these experiments are aimed at reproducing what has already been explained in paragraph 5.2.3.1. In order to analyse the behaviour of the copper contaminated samples, the experiment has been carried out using other clean samples so that their performance can be considered as a reference for the analysis of the behaviour of copper contaminated samples. However the two samples were treated with a negative charge deposition and the measured average lifetimes for these samples are shown in figure 7.13.

As we can see from the figure, in the clean wafers Herguth's method produces a steep decrease of the average lifetime during the first hours; when the samples are exposed to the illumination at room temperature, we can also notice that the lifetime suffers a further slight decrease during the illumination. On the other hand, on copper contaminated samples we can notice that Herguth's method produced an enhancement of the lifetime; that increase of lifetime is compensated by degradation induced by illumination at room temperature. Although Herguth's method did not produce the desired effects(in the clean sample the lifetime dropped during the annealing phase, in the copper contaminated sample the final lifetime corresponds to the initial one, although there was an enhancement during the illumination at 120°C), the behaviour of the copper contaminated wafer will be confirmed by other experiments carried out with a new experiment set.

In order to deeply investigate the behaviour of the copper contaminated samples, the maps regarding the lifetime distribution of the samples mentioned before are shown in the picture 7.14.

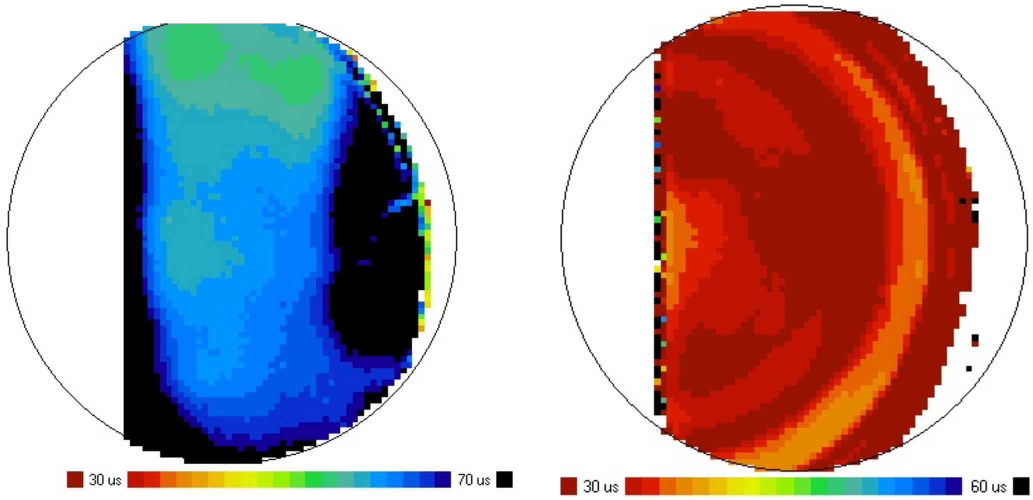

(a) Received sample(clean wafer)

(b) Received sample(contaminated wafer)

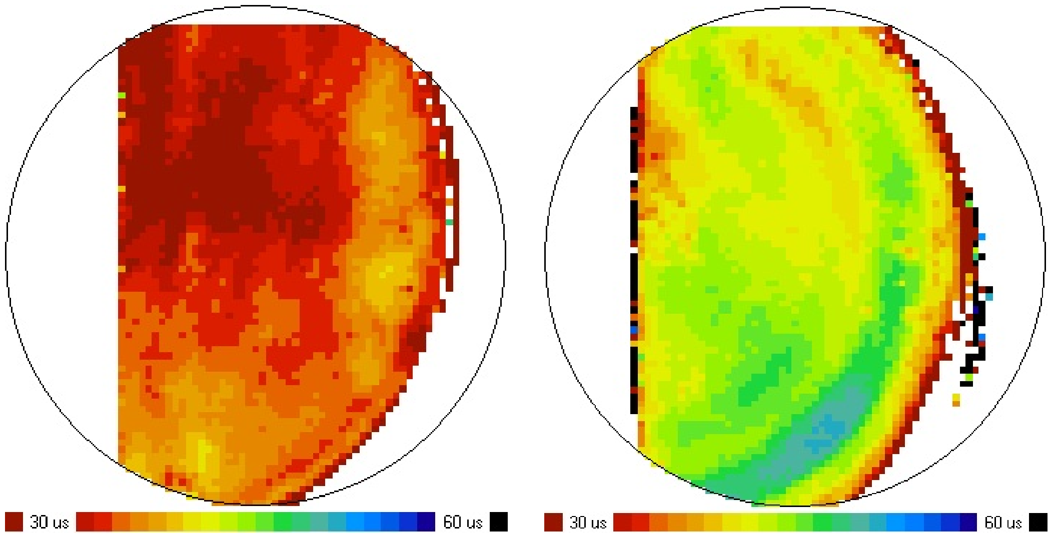

(c) 42 hours Herguth's method(clean wafer)

(d) 42 hours Herguth's method(contaminated wafer)

Figure 7.14: Comparison between the clean and the copper contaminated sample before and after Herguth's method: note the presence of some "rings" on the contaminated sample that remains evident across the sample surface also after Herguth's method

As we can see, Herguth's method produced a strong degradation on the clean sample which resulted to be uniform throughout the sample surface. On the copper contaminated sample, instead, the annealing and illumination phase produced a different distribution of the lifetime which resulted extremely dependant on the initial lifetime values. Particularly the areas where the lifetime was extremely low presented a slight enhancement of the lifetime during the illumination at 120°C, whereas the circular regions with a high initial lifetime showed a significant enhancement of the lifetime resulting particularly visible even after the annealing and illumination step. The maps of the lifetime distribution during illumination at room temperature are shown below.

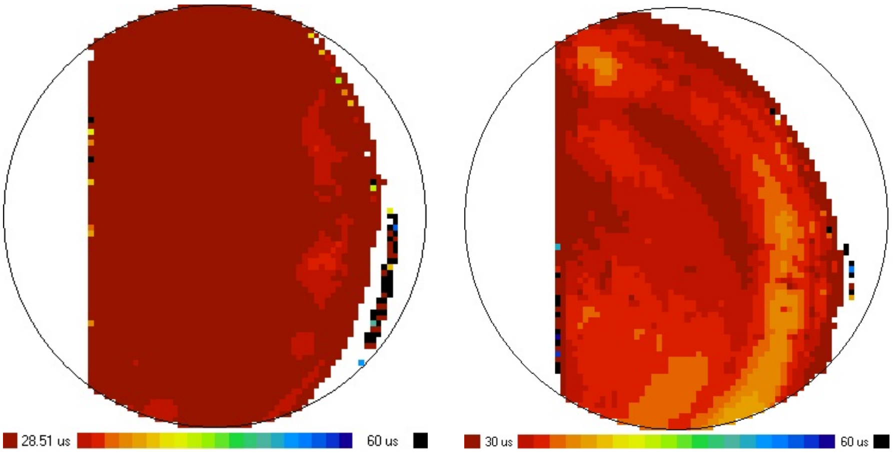

(a) 38 hours(clean sample)

(b) 38 hours(copper contaminated sample)

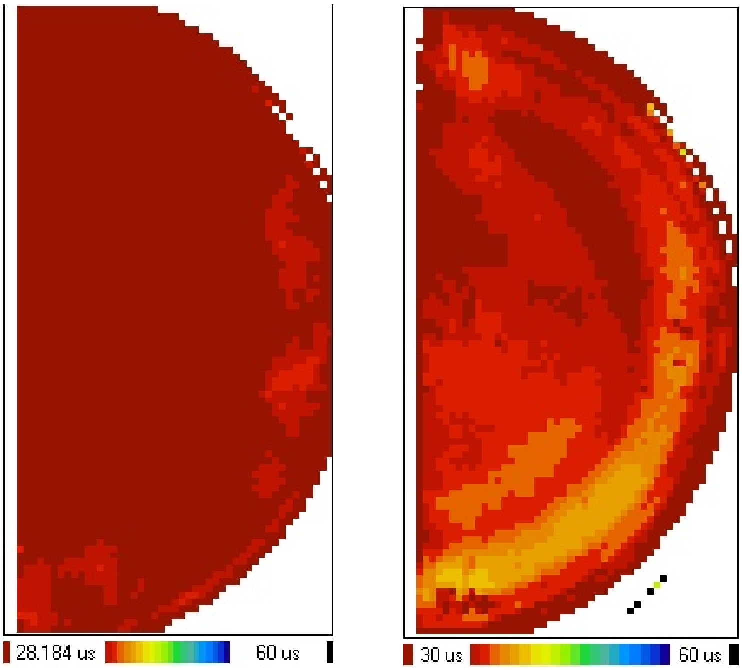

(c) 60 hours(clean sample)

(d) 60 hours(copper contaminated sample)

Figure 7.15: Lifetime distribution map during the illumination phase of the same samples shown in picture 7.14; again note the presence of the lifetime rings on the copper contaminated sample

Analogously to the previous step, the degradation phase on the clean sample resulted to be extremely uniform, confirming the fact that Herguth's method did not produce any positive effect on the reduction of the degradation. On the copper contaminated sample, instead, the circular areas with a higher lifetime were still visible after 60 hours of continuous illumination showing that Herguth's method produced some beneficial effects on the reduction of the lifetime decay. These results will be partly confirmed and improved by the second experiment set, where Herguth's method was performed with a different passivation layer and with different amounts of negative charge.

7.1.5 Conclusion

The results concerning this first experiment set showed that the lifetime decay on the previous samples is probably dominated by the formation of boron-oxygen complexes. In order to reduce the formation of these defects, Herguth's method was tested on samples that underwent different treatments(annealing and degradation step prior to Herguth's method, intentional copper contamination); most of these treatments did not produce any significant reduction of the degradation.

Finally the charge deposition resulted to strongly affect the effectiveness of the lifetime recovery procedure: the presence of negative charge, in fact, produced an opposite effect causing an evident reduction of the lifetime during the recovery, as opposed to neutral and positively charged samples where the recovery procedure produced a considerable enhancement of the lifetime.

7.2 Second experiment set

This section will show the experimental results obtained using monocrystalline silicon wafers provided by a different supplier; for these wafers the supplier reported the presence of some unintentional copper contamination. The samples used for these experiments can be divided into two categories:

- **S-wafers**: without emitter;
- **E-wafers**: with a thin n-doped emitter;

The emitter is an additional layer whose function is to reduce metallic impurities or other types of crystal defects through the diffusion-induced gettering of impurities. A gettering process consists of three steps, i.e. impurity release from its energetic binding, travel through the wafer by diffusion and finally capture of the impurity where the emitter acts as a sink. Thus wafers treated with an emitter layer should result cleaner than the counterparts without the emitter liner. Moreover the solar cell is based on a p-n junction, as illustrated in chapter 1, thus the emitter layer acts as the n- side of the junction becoming a fundamental element for the correct operation of the solar cell.

Different passivation layers have been tested: initially some samples were prepared with a silicon dioxide layer and the LID was studied varying the amount of deposited charge on the surface. Subsequently the performance of aluminum oxide passivated samples, with layers deposited using the ALD technique, was studied as a function of different amounts of deposited charge. Analogously to the previous section, the experiments will be subdivided into three categories(LID, Herguth's method and recovery) for both the two passivation types.

7.2.1 Silicon-dioxide passivation

7.2.1.1 LID experiments

LID experiments consisting of illumination at room temperature of the samples were carried out also on this experiment set obtaining the results shown in the picture. On these samples we can consider that two phenomena take place at the same time: the formation of recombination active boron-oxygen complexes and the degradation induced by the activation of copper defects. In these samples copper introduced defects seem to dominate over the boron oxygen complexes: in accordance to the results shown in the next paragraph, the presence of the surface charge leads to an evident suppression of the degradation phenomenon; if boron-oxygen complexes were dominating over copper introduced defects, no effect on the degradation process would be observed. We can also notice that the sample shown in figure 7.17 presented a pseudo-exponential decay, analogously to the behaviour observed in paragraph 7.1.2.

In order to estimate the amount of defects activated by the illumination an important parameter can be extracted from the measured lifetime. Indeed the number of defects is usually expressed as follows

$$N_t^* = \sigma_n v_{th} N_t \tag{7.5}$$

where σ is the capture cross section and N the concentration of the metastable and residual defects respectively and v_{th} indicates the thermal velocity. Thus it results that the amount of activated defects is given by the following equation

$$N_t^* = \frac{1}{\tau_d} - \frac{1}{\tau_0} = (\sigma_{res} v_{th} N_{res} + \sigma_n v_{th} N_t) - \sigma_{res} v_{th} N_{res} \tag{7.6}$$

where N_t^* represents the generation rate of the defect activated by illumination, whereas N_t and N_{res} indicate the concentrations of the metastable and residual defects respectively[35]. This parameter will result particularly useful in the next paragraph where the lifetime decay of some charged samples will be examined; indeed equation 7.6 shows the reduced amount of defects induced by the surface charge deposition.

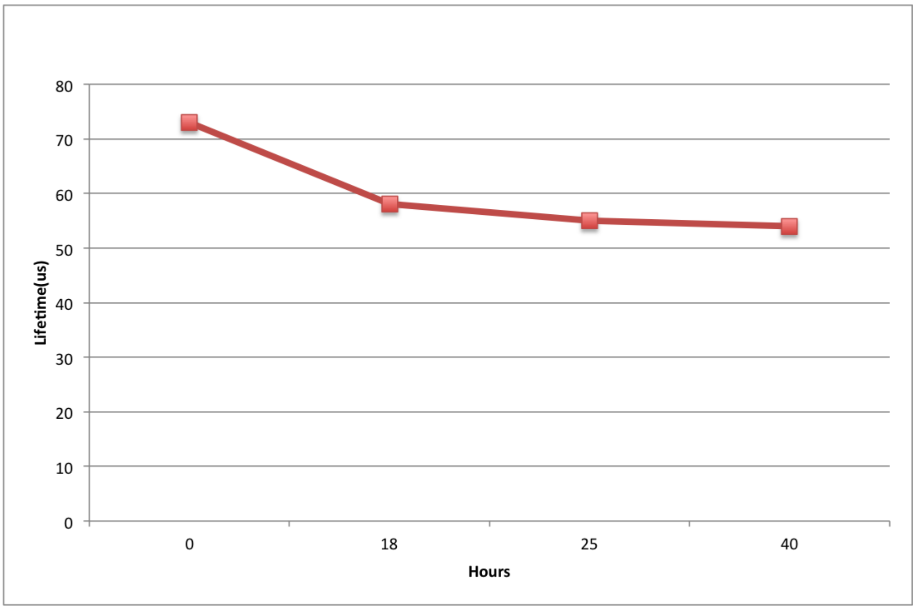

Figure 7.16: Lifetime decay during an LID experiment; note the pseudo-exponential trend of the curve in which the degradation process is more accentuated during the first 20 hours of illumination

7.2.1.2 Effects of surface charge on LID

In order to reduce the impact of copper defects on the lifetime, different amounts of surface charge were deposited. The previous samples demonstrated that in this experiment set the copper concentration is not negligible and may dominate the degradation process, making the charge deposition one of the best candidates for the reduction of the light-induced degradation phenomenon. Note that these samples were etched before the thermal oxidation; in particular a 20nm thick layer was removed because the lifetime of the received wafers resulted very low likely due to the presence of some contaminants on the surface region of the wafer. Thus we can consider that on these samples the emitter layer had been completely etched away along with the contaminated layer of the wafer.

Table 7.5 shows the final and initial lifetime after 24 hours of illumination at room temperature varying the amount of deposited charge and the wafer type. As we can see, the behaviour of these wafers appeared to be the same, regardless of the type so that we can conclude that the only parameter that plays a key-role on light induced degradation is the deposited charge. From the graph shown in figure 7.18, negative charge strongly reduces the lifetime degradation, especially with considerably high amounts of charge: indeed with -900 μC the LID phenomenon resulted to be completely suppressed. Moreover the increased amount of negative charge had a

0 μC surface charge deposition			
Wafer type	Initial lifetime(μs)	Final lifetime(μs)	Degradation $\tau_f - \tau_i$
E	94	57	37
E	59	40	19
S	73	54	19
-300 μC surface charge deposition			
S	53	52	1
E	52	50	2
-900 μC surface charge deposition			
S	73	72.5	0.5
+300 μC surface charge deposition			
E	45	30	15

Table 7.5: Effect of charge deposition on light-induced degradation(E-type wafers are with emitter, S-type without emitter); all the samples were passivated with a silicon dioxide layer. We can immediately notice that the presence of negative charge significantly reduces the LID phenomenon; this result is in accordance to the model introduced in chapter 5, in which positively charged copper ions are attracted towards the surface

positive impact on the stabilization of the lifetime. During the illumination, the lifetime on the samples with a smaller amount of negative charge had a peculiar behaviour, presenting a little increase during the first hours and then a stabilisation around the initial value. However the effect of the negative charge on the lifetime evolution is shown in the pictures below.

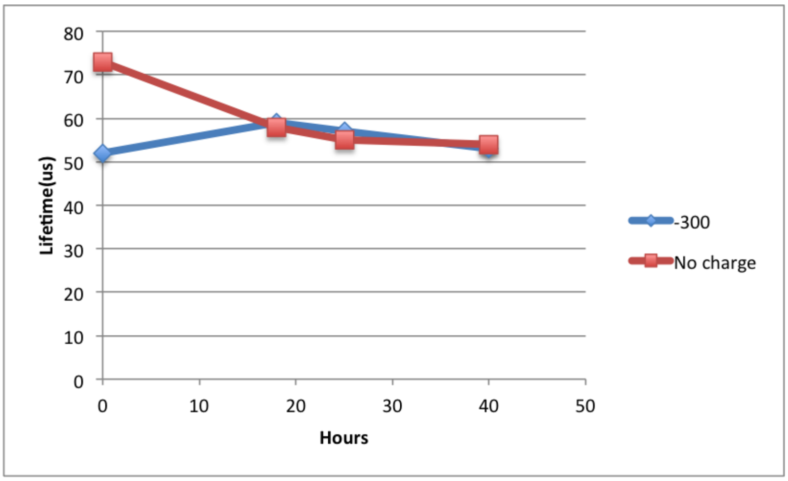

Figure 7.17: Comparison between the lifetime trend on a sample with no surface charge and another one with -300μC deposited charge; the presence of negative charge reduces considerably the degradation. Note also the enhancement of the lifetime during the initial hours.

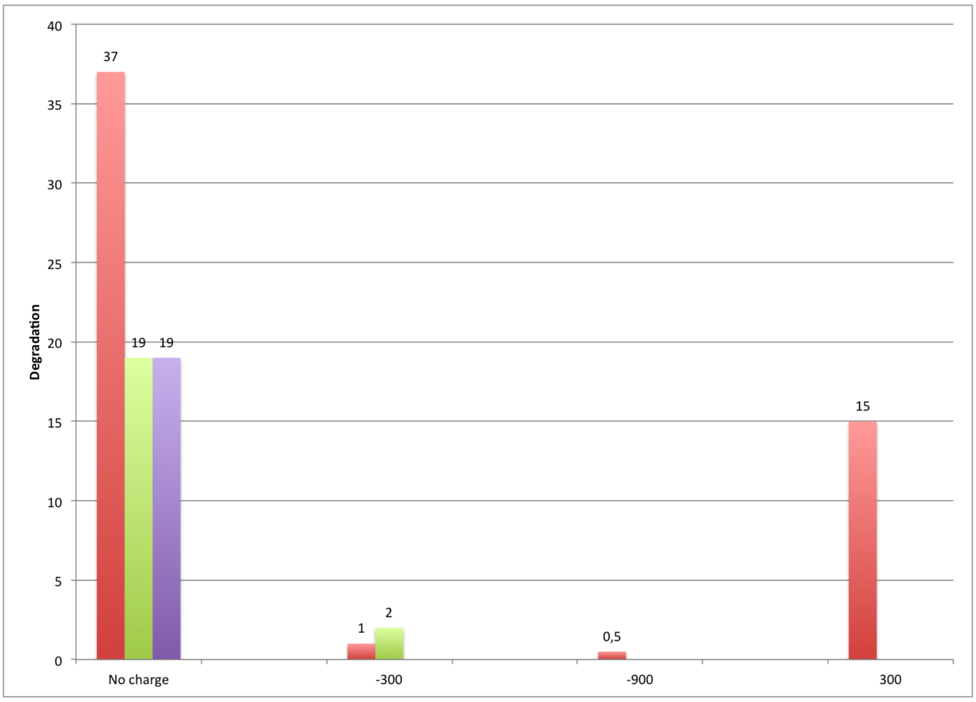

Figure 7.18: Graphical representation of the values shown in the previous tables; again it is possible to appreciate the reduction of LID thanks to the presence of negative charge

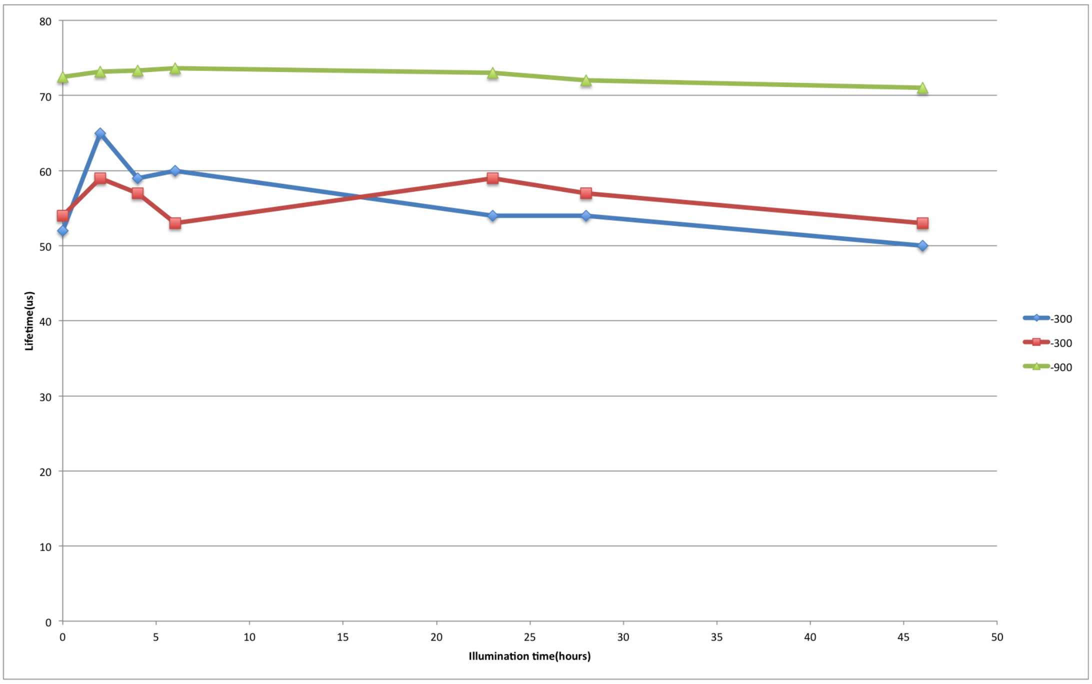

Figure 7.19: Effect of negative charge on the stabilization of lifetime in LID experiments: the graph clearly shows that the suppression of LID phenomenon is strongly dependent upon the amount of deposited charge; a complete stabilization of the lifetime is achieved with -900 μC

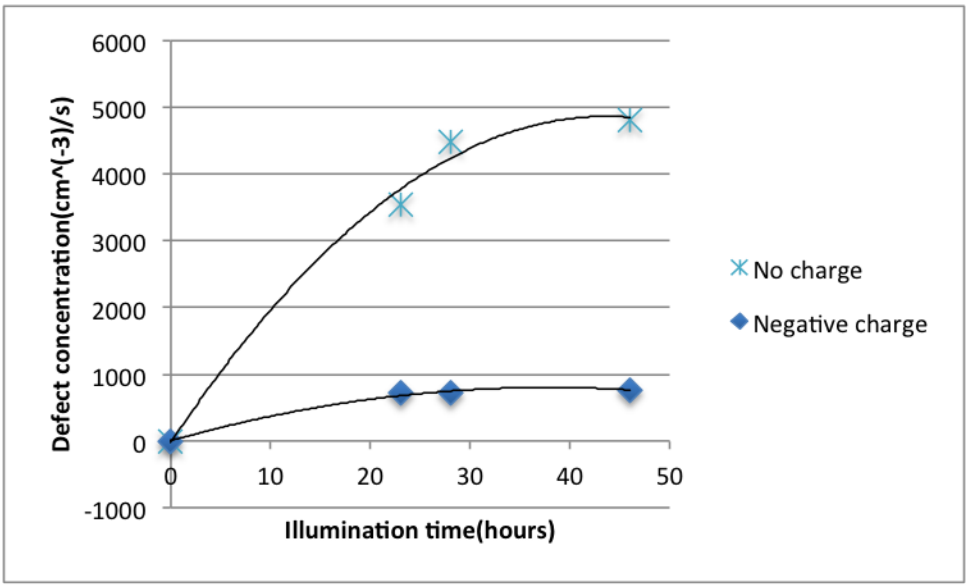

Figure 7.20: Variation of the defect concentration as a function of illumination time for samples with and without negative surface charge(see equation 7.6): negative charge reduces considerably the defect concentration confirming the hypothesis that these samples contain a non-negligible amount of unintentional copper contamination

We can also notice from figure 7.19 that a considerable amount of negative charge stabilises the lifetime making the line that describes the evolution of the lifetime extremely flat.

Exploiting the equation 7.6, it is also possible to evaluate the generation of defects activated by illumination; figure 7.20 shows the defect concentration as a function of time. We can see that the negative charge can reduce the generation rate up to one fifth of the initial concentration; moreover the graph clearly shows that with no charge the concentration of the generated amount of defects corresponds to nearly 5000 cm^{-3}/s, whereas after the deposition of negative charge the concentration is reduced below 1000 cm^{-3}/s.

7.2.1.3 Lifetime distribution maps

In the previous paragraph the average lifetime were presented, now we want to analyse the effects of LID on the lifetime distribution maps on the samples whose average lifetimes were reported previously.

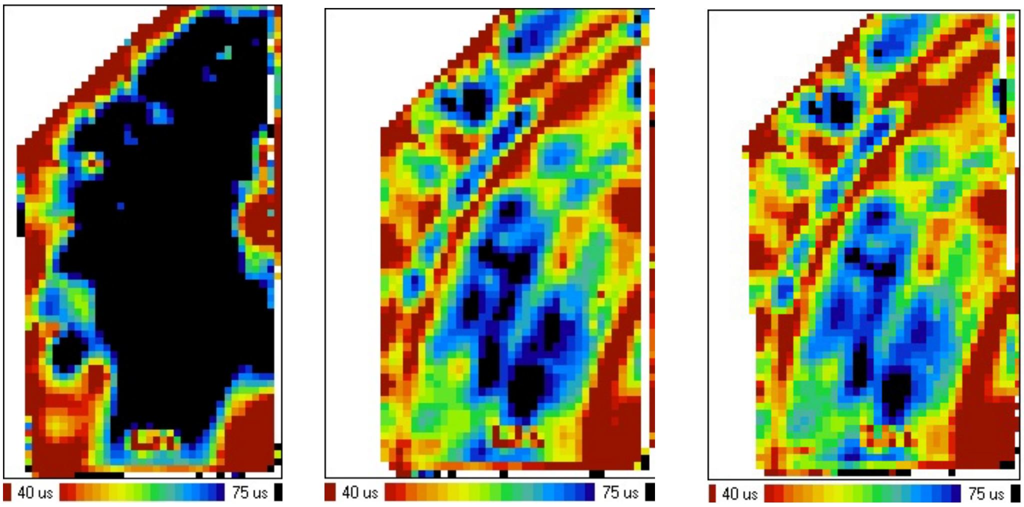

(a) as received sample (b) after 25h illumination (c) after 40h illumination

Figure 7.21: Lifetime distribution maps(S-type sample)

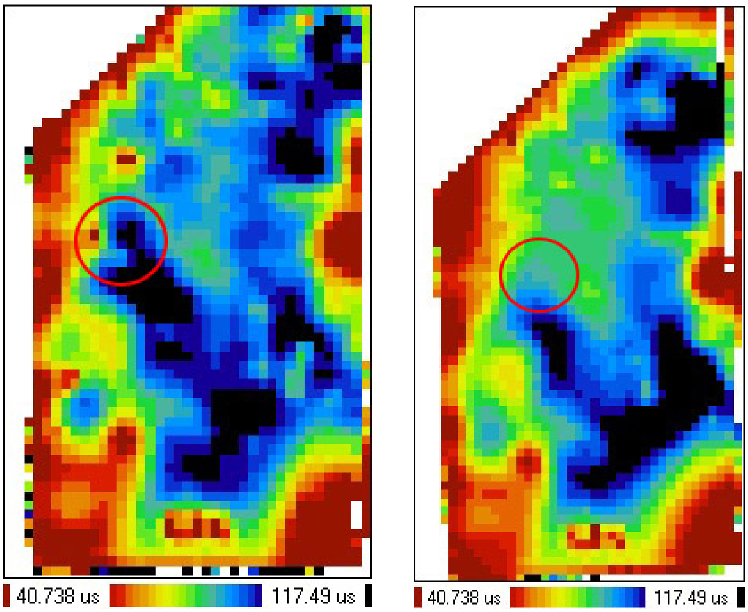

(a) Received-sample (b) After negative charging

Figure 7.22: Lifetime distribution map before and after deposition of negative charge: in the circle it is possible to observe that some areas with a very high lifetime suddenly disappear after the charge deposition. These images refer to an E-type sample.

We can notice that on these samples the lifetime is not homogeneous, since

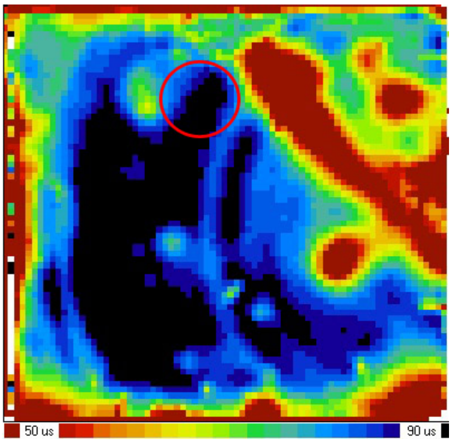

(a) 3h

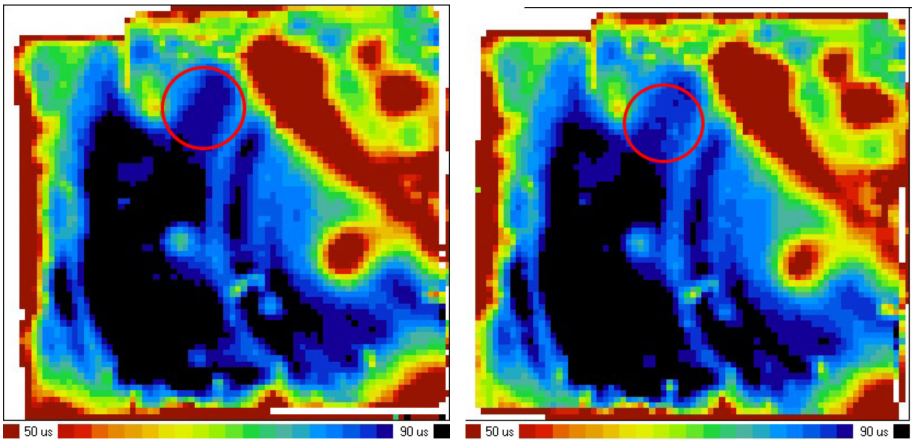

(b) 5h

(c) 7h

Figure 7.23: Lifetime distribution map during illumination on a S-type sample: in the circle it is possible to notice the presence of a slight lifetime degradation, that does not affect significantly the average value

there are some bad areas with a very low lifetime, and some others with a considerably high lifetime which are highly affected by the light-induced degradation. The presence of the bad areas might be attributed to two reasons: the former could be related to a possible unintentional contamination of the samples by metal impurities during the high temperature(900°C) thermal oxidation and the latter might be related to inhomogeneity of the passivation layer. In the bad areas, however, the lifetime is already at a very low saturation level, therefore they do not take part in the degradation process. On the other hand, the regions with a very high lifetime suffer a strong degradation, reducing considerably the average lifetime. After the charge deposition, two different behaviours were observed depending on the sign of the deposited charge: after the deposition of negative charge the lifetime resulted slightly reduced, whereas a slight enhancement of the lifetime was observed after the deposition of positive charge. With reference to figure 7.22 we can notice that some blue areas, which represent high lifetime regions, suddenly disappear after the charge deposition. This phenomenon is due to the fact that some holes are attracted by the negatively charged surface and thus increase the recombination activity of the surface causing a considerable reduction of the overall lifetime of the sample.

After the charge deposition, the copper defects are attracted towards the surface according to the mechanism explained in the figure 5.4. This phenomenon produces a reduction of the degradation, as demonstrated by the data presented in the previous paragraph and the lifetime maps shown in picture 7.23. As we can see, the charge deposition strongly reduces the lifetime degradation on the whole sample surface. In the red circle, we can still notice the presence of a slight degradation in some areas that do not affect significantly the average lifetime.

7.2.1.4 Lifetime recovery

In order to find a confirmation of the previous results concerning the effects of the deposited charge on the lifetime enhancement achieved through annealing at high temperature(180°) in the dark after 15 minutes, the recovery procedure was tested also for this experiment set. The results are summarised in the table below.

Recovery with negative charge(-900 μC)		
Initial lifetime(μs)	Final lifetime(μs)	Gain(μs)
125	67	-58
85	65	-20
58	21	-37
93	17	-76
Recovery with positive charge(+300 μC)		
72	86	14
Recovery with no charge		
74	98	24

Table 7.6: Effect of negative charge on the recovery process: again we have a confirmation that negative charge produces a decrease of the average lifetime after recovery

Again we can see that with negative charge the recovery procedure does not cause a strong reduction of the lifetime, whereas the best results in terms of lifetime gain are obtained with no charge. With positive charge, however, there was still an enhancement of the lifetime which resulted slightly lower than those samples containing no surface charge. This experiments substantially provided a confirmation of the results that were presented in paragraph 7.1.3, hence surface charge must be deposited after the recovery on all the samples that were recovered before Herguth's method, in order to achieve the highest possible lifetime.

7.2.1.5 Herguth's method

In this section the results regarding Herguth's method performed on both S-type and E-type wafers with a silicon-dioxide passivation layer will be presented. Unlike the samples used for the previous experiment, these wafers were not treated with any etching process before Herguth's method. The results are shown in the figure below.

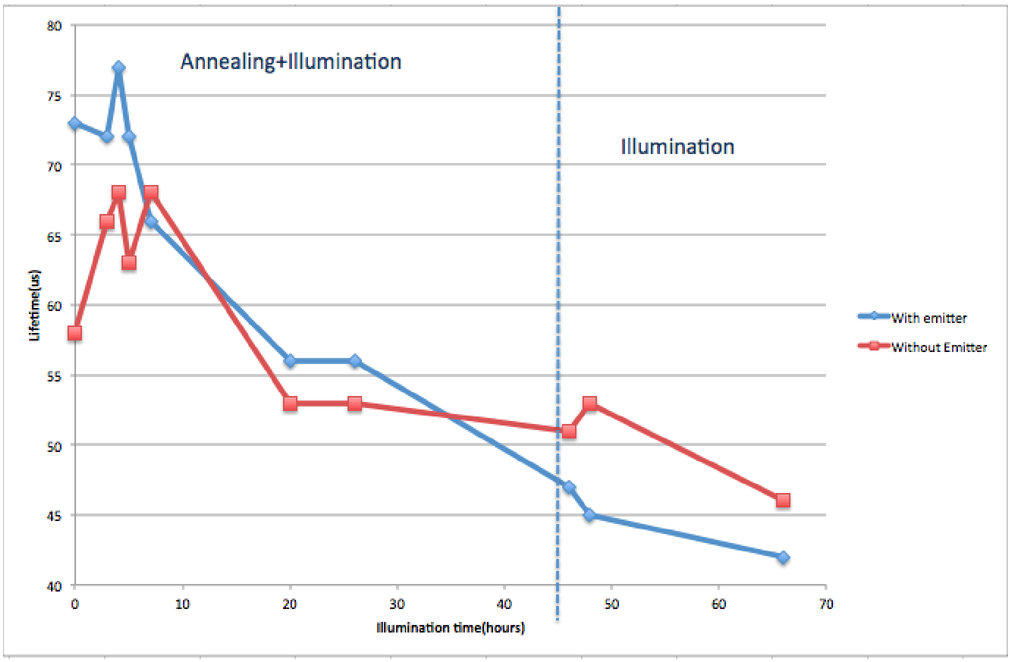

Figure 7.24: Herguth's method performed on aluminum-oxide passivated samples with no deposited charge: it seems the use of a different passivation layer does not produce a significant effect on the stabilization of the lifetime

As we can see from the picture, there was a decrease of lifetime during the annealing and illumination step, in accordance to the model introduced at paragraph 5.2.2. Unfortunately after the annealing step the trend of the lifetime did not appear to be stabilized, since the graph shows a further degradation during illumination at room temperature. Compared to the experiments presented in paragraph 7.1.4 two parameters have been varied:

- The material constituting the bulk;
- The presence of an emitter layer;

None of these parameters produced significant results on the suppression of light-induced degradation. There are still two parameters that can be changed:

- The passivating layer;
- The surface charge;

The effects of these parameters on the suppression of lifetime degradation will be discussed in the next paragraph.

7.2.2 Aluminum oxide passivation

As already stated in chapter 5, aluminum oxide passivation strongly reduces the surface recombination causing a considerable enhancement of the lifetime in respect of silicon-dioxide passivation. Moreover aluminum oxide liners naturally contain some negative charge which can attract the copper ions from the bulk. Two experiments were carried out with this passivation layer: LID experiments and Herguth's method. In these experiments the lifetime degradation was tested with two different thicknesses of the passivation layer. After the deposition of the passivation layer an annealing step(400°C for 30 minutes) was necessary to enhance the passivation and consequently the initial lifetime of the samples.

7.2.2.1 LID experiments with 20 nm thick passivation layers

The first experiments were carried out with a thin passivation layer and no deposited charge on the surface. The results including the enhancement of the lifetime due to the annealing step are shown in the figure 7.25.

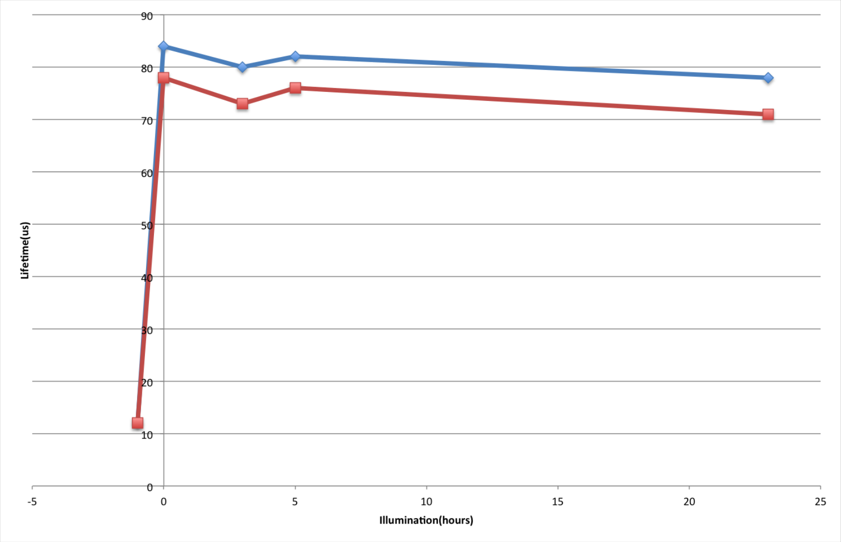

Figure 7.25: LID experiment on aluminum-oxide passivated samples(the negative x-axis shows a preliminary treatment obtained through an annealing step at 400°C for 30 minutes); the deposition of this passivation layer produces a good - although not complete - reduction of the lifetime. Note that the blue line shows the measured lifetime on a E-type sample whereas the red one refers to S-type

As we can see from picture, the lifetime was enhanced through the short annealing step and then it appeared rather stable during the illumination at room temperature. However the initial lifetime of the samples was expected to be higher than the values shown in graph. In fact it resulted to be around 80-90 μs, a value which results comparable to the measured lifetimes on silicon-dioxide passivated samples. This low lifetime might be attributed to the low quality of the wafers, since a further 20 nm etching step did not produce any relevant result.

7.2.2.2 LID experiments with 40 nm thick passivation layers

The results obtained with a 40 nm thick passivation layer are presented in the picture below. First of all we can notice that the initial lifetimes resulted considerably higher than those presented in the previous paragraph with a 20 nm thick passivating layer.

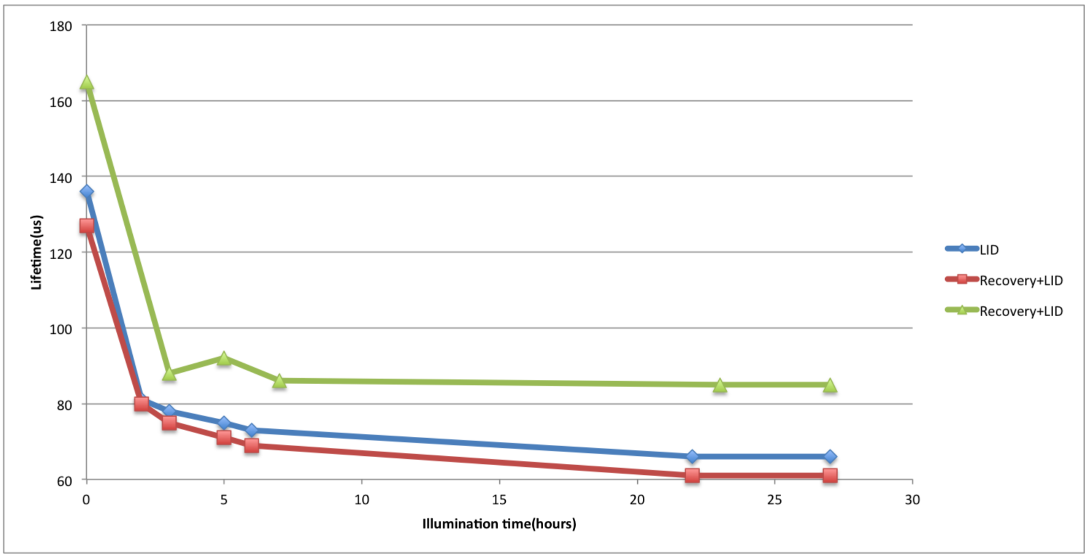

Figure 7.26: Comparison between S-type samples exposed directly to illumination and treated with a preliminary recovery before illumination

We can immediately notice that the lifetime decay follows an exponential trend showing an analogous behaviour compared to the results shown in paragraph 7.1.1. This result can be attributed to the fact that the passivation layer introduced some negative charge that can attract the copper defects towards the surface. In the bulk, therefore, the recombination centers are mainly created by the boron-oxygen complexes causing the exponential decay of the lifetime depicted in figure 7.26. Analogously to paragraph 7.1.1, it is possible to fit the curves, in order to estimate the parameters shown in the equations presented in the paragraph 7.1.1(see equation 7.3). The fitting of the lifetime measurements gives the results shown in table 7.7.

Comparing these results with those shown in paragraph 7.1.1, we can immediately notice that the values of the time constant τ_0 in this experiment set result to be

LID		Recovery+LID	
τ_0	2	τ_0	3.8
μ	0.66	μ	0.64

Table 7.7: Extrapolation of the parameters introduced in eq.7.3 through the use of fitting techniques. These fitting parameters have been extrapolated from the blue and red line shown in figure 7.26(which represent the degradation respectively with LID and Recovery+LID)

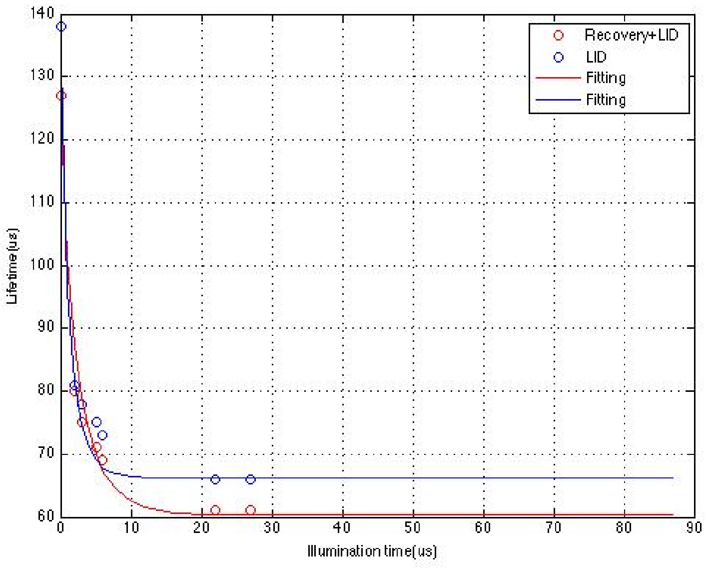

Figure 7.27: Graphical representation of the fitted curves; the overlapping between the fitted values and those predicted by the fitted curves substantially confirms the validity of equation 7.3

considerably lower than those shown previously. This means that the decay of the lifetime results much faster than before: as we can see from figure 7.27, indeed, the lifetime reduces up to one half of the initial value during the first illumination hours. This behaviour could be related to a higher oxygen concentration that speeds up the degradation process leading to a fast decay of the lifetime.

7.2.2.3 Herguth's method

Herguth's method was tested only on 40nm thick aluminum oxide liners, since with this type of passivation we want to stabilize the lifetime around relatively high values. Particularly in this section the impact of the passivation layer and the deposited charge on the evolution of the lifetime during Herguth's method was studied.

7.2.2.3.1 No deposited charge In this experiment Herguth's method was tested on some samples treated with a preliminary recovery step(15 minutes annealing at 200°C in addition to a previous annealing step at 400°C for 30 minutes). In order to compare the results obtained with a preliminary lifetime recovery, some samples, which were not treated with the annealing at 200°C, were exposed to the same conditions. The results concerning these samples are shown in figure 7.28.

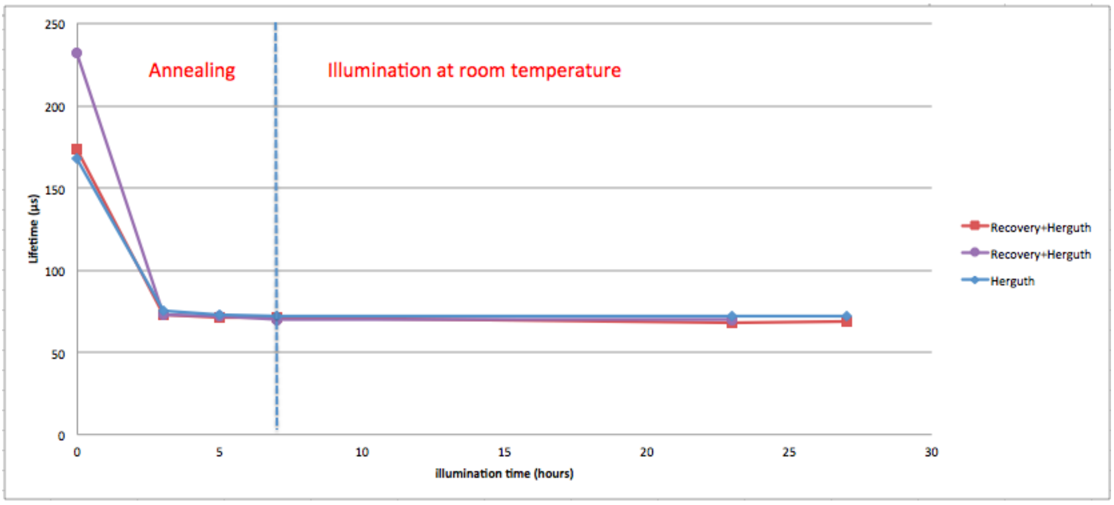

Figure 7.28: Herguth's method performed on S-type samples passivated with 40nm thick aluminum oxide layers and with no deposited charge; the preliminary recovery step seems not to produce any relevant result on the effectiveness of Herguth's method

We can notice that there was a steep degradation during the initial hours of the illumination at high temperature(120 °C)(in the figure that phase is marked with "annealing"). After the initial decay the curve becomes flat, indicating that effectively there was no degradation during the illumination at room temperature. Despite this achievement, lifetime stabilized between 70 and 85 μs resulting considerably lower than the initial lifetime. In these experiments the purpose of using 40 nm thick liners was to test the effect of passivation quality on Herguth's method. Nevertheless these samples still presented an evident decay of the lifetime; as a consequence, Herguth's method was tested varying a new parameter, i.e. the amount of deposited surface charge on the sample.

7.2.2.3.2 Herguth's method with surface charging In order to analyse the effect of the surface deposited charge on the lifetime during Herguth's method, different amounts of surface charge(+300 μC and -300 μC) were deposited by corona charging on two different samples. The graph in figure 7.29 shows a comparison between the positive charged sample and the counterpart with surface negative charge.

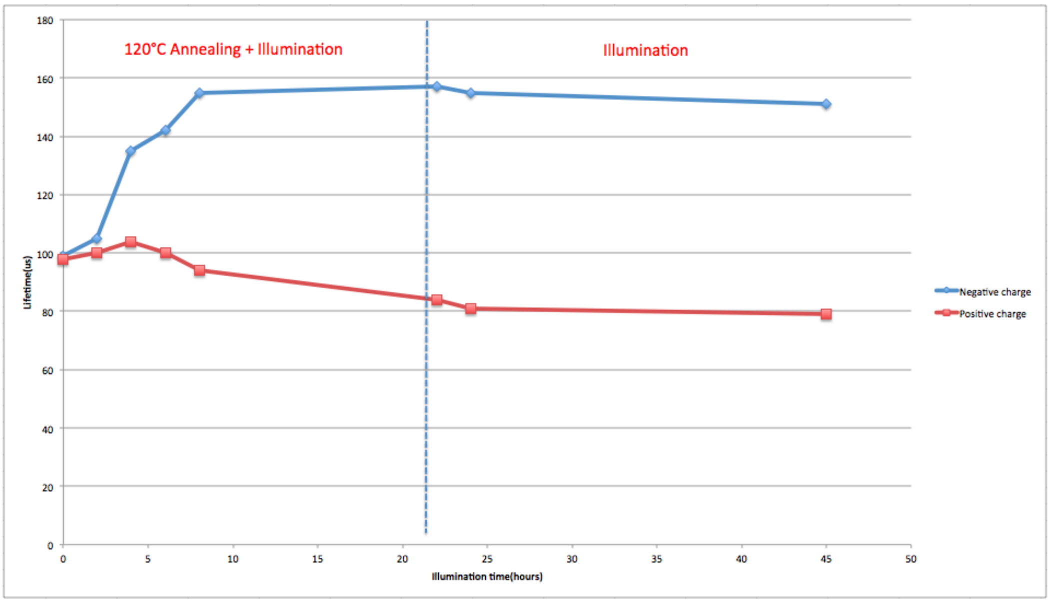

Figure 7.29: Herguth's method performed on S-type samples passivated by 40nm thick aluminum oxide layer with surface charge equal to +300μC(red line) and -300μC(blue line); the negatively charged sample showed an enhancement of the lifetime during the illumination and annealing step and a subsequent stabilization around a rather high lifetime value. A similar behaviour had been observed in figure 7.13 with intentionally copper contaminated samples

The graph shows that negative charge produces an opposite effect on the lifetime during the simultaneous illumination and annealing step: while in figure 7.28 the lifetime drastically dropped during the initial hours, on the sample with negative charge, instead, we can notice a considerable enhancement of the lifetime. This behaviour had already been observed in paragraph 7.1.4.2 where Herguth's method was tested on intentionally contaminated samples exposed to the same conditions(annealing at 120 °C and 1 Sun illumination). Although the lifetime of the copper contaminated samples resulted much lower than those passivated with aluminum-oxide liners, the trend of the lifetime resulted to be the same: considerable enhancement of the lifetime during the annealing step, a slight degradation during illumination at room temperature and then a stabilization around a relatively high lifetime value.

Unfortunately in literature the modelling of the phenomena that occur during Herguth's method is still incomplete and it does not provide a deep understanding of the results obtained varying some parameters, such as the passivation layer, the presence of a preliminary recovery step or a fixed amount of surface charge. Therefore the reason underlying the failure of the previous experiments with Herguth's method is still unknown. However the results shown in the previous figures provide at least an experimental proof of the effects that some parameters could have on the outcome of all the methods presented so far. With respect to Herguth's method, the reduction of the lifetime degradation was obtained with highly contaminated samples and a certain amount of negative surface charge.

For the sake of completeness, the lifetime map of the negatively charged sample that showed a strong reduction of the degradation is preseted in figure 7.30. As we can clearly notice, the enhancement of the lifetime observed during Herguth's method is mainly localized in the areas with a high initial lifetime. After 22 hours of illumination at high temperature we can consider that the good regions reach a saturation level, so that the phase consisting of the illumination at room temperature can be started. We can see that illumination causes a small degradation that slightly reduces the average value of the lifetime: if we compare the lifetime maps shown in the figures 7.30c and 7.30d we can notice that the blue regions keep approximately the same area, confirming the fact that Herguth's method produced a significant reduction of the light-induced degradation.

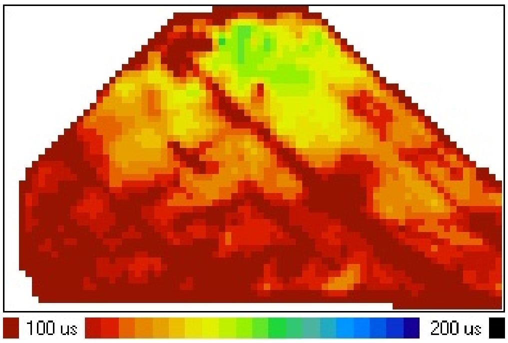

(a) Herguth 2h

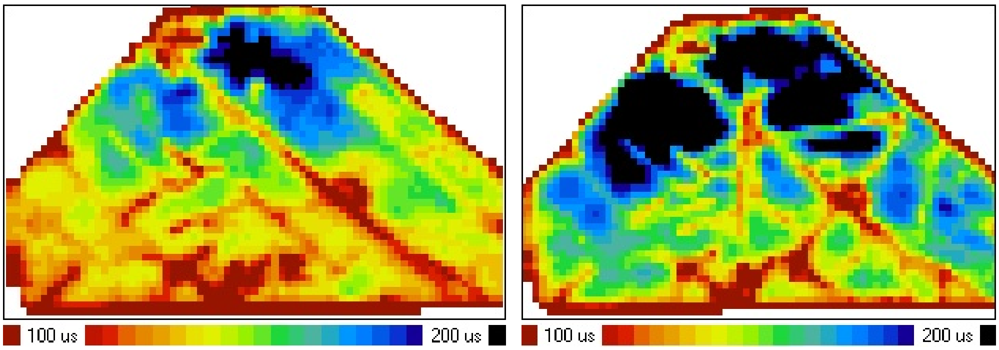

(b) Herguth 4h

(c) Herguth 22h

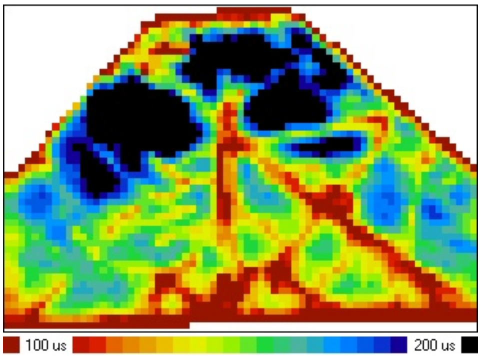

(d) Illumination 21h

Figure 7.30: Lifetime distribution map during the illumination and the simultaneous annealing step performed on a S-type negatively charged sample; it is possible to notice the enhancement of the measured lifetime during the annealing and simultaneous illumination phase

Chapter 8

Conclusions

Nowadays copper probably represents the most interesting material for the realization of metallic contacts. The employment of this material in the fabrication of integrated circuits is well-known, as well as the deposition of barriers that prevent the contamination of the bulk due to its high diffusivity in silicon. The use of copper for PV applications is still under investigation, and it is likely that it will replace silver in the near future. However an effective and reliable method for the reduction of its drawbacks still must be found.

This thesis work initially presented a brief dissertation regarding the behaviour of copper in silicon and the state-of-art of the copper barriers, including those materials whose characteristics are suitable both for VLSI and PV applications. Successively this thesis work focussed mainly on the light-induced degradation and the study of the roll of copper on this phenomenon. This part represent a fundamental background for the understanding of chapter 7, where several methods aimed at the reduction of LID have been tested on the basis of the experimental results.

In order to summarize all the experiments that have been presented previously, a scheme representing the whole experimental work is shown in figure 8.1.
The results of these experiments gave evidence of the following assumptions:

- The recovery procedure resulted successful only with positive charge. On the other hand, negative charge produces an an opposite effect.

- Deposition of negative charge produced a strong reduction of the light-induced degradation especially on those samples that presented a high copper concentration.

- Aluminum-oxide passivation layers provide a promising performance in terms of suppression of light-induced degradation.
- Herguth's method contributed to reduction of the lifetime degradation only with high copper concentrations and a high amount of surface negative charge.

Some of the achievements listed above find a precise explanation through the theoretical models discussed in the previous chapter. For instance, the reduction of the lifetime degradation after the negative charge deposition can be explained through the attraction between positive copper ions and the surface negative charge, as stated by J.Lindroos et al.[39]. Analogously the results obtained with aluminum oxide passivation confirm the presence of negative charge in the passivation layer, that creates similar effect as the charge deposited by corona charging. Although the purpose of this study was not to quantify the amount of negative charge provided by the passivation layer, the experimental results with this passivation type showed a significant reduction of the light-induced degradation that might be attributed to the presence of some native negative charge in the passivation layer; moreover the aluminum oxide passivation provided a better performance in terms of reduction of surface recombination. Indeed the minority carrier lifetime of the samples with this kind of passivation resulted to be notably improved in respect of silicon-dioxide passivation.

A plausible explanation of recovery procedure and the effect of negative charge was provided in paragraph 7.1.3 on the basis of the scarce information available in literature. Unfortunately most of the publications that were included in the bibliography mentioned the recovery procedure without providing a theoretical explanation of the process involved in this kind of experiments. Analogously the effectiveness of Herguth's method on the deactivation of boron-oxygen complexes is not clear yet: all the publications concerning Herguth's method reported some experimental results in which the degradation was effectively reduced. Nevertheless the authors did not provide any precise explanation of the process that should cause the reduction of light-induced degradation. In this work, Herguth's method was tested under different conditions and the experimental results showed that Herguth's method provided a reduction of the lifetime degradation only under particular conditions(deposition of negative charge and high copper concentration); unfortunately because of incompleteness of the information available in literature, it was not possible to provide a plausible theoretical explanation of these experimental results. For these reasons LID and the different approaches for its reduction still remain a challenging research topic; this thesis presented new experimental results obtained through the variation of some important parameters(passivation type, intentionally deposited charge, pureness of the starting material...), in the hope that the present work will result useful for a deeper understanding, as well as a more complete modelling of LID and its related phenomena.

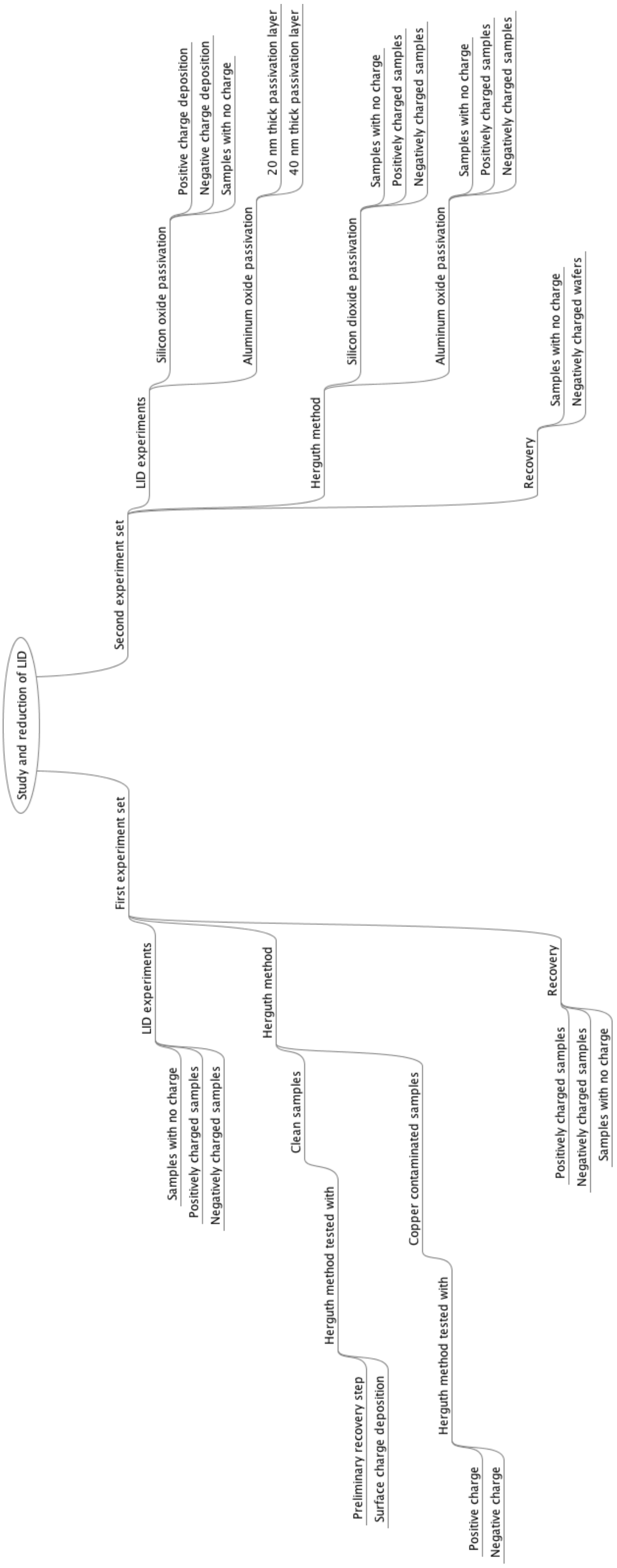

Figure 8.1: Overview of the experimental activity

Bibliography

[1] SCHOTT Solar AG, RENA GmbH, and CiS Forschungsinstitut, Las VeGaS project, 21st International Photovoltaic Science and Engineering Conference Fukuoka, Japan 2011

[2] Andreas Beneking *Innovazione di contatto*, Photon, Ed.Giugno 2012

[3] P.Wurfer *Physics of solar cells, from basic principles to advanced concepts*, pag.180 Wiley vch, 2009

[4] Kaneka and imec, 21st International Photovoltaic Science and Engineering Conference Fukuoka, Japan 2011

[5] M. Yamaguchi, Super-high-efficiency multi-junction solar cells, Progress in photovoltaics: Research and applications, Vol. 13, p. 125, 2005.

[6] A.A.Istratov, E.R.Weber *Physics of copper in Silicon, 2001, paragraph on the diffusivity of Cu*

[7] R.N.Hall and J.H.Racette, *Journal of Applied Physics*, 35, 379 , 1964

[8] L.Wen, G.Mon, E.Jetter, R.Ross jr. *Electromigration in thin film photovoltaic module metallization systems*, Photovoltaic Specialists Conference, 1988., Conference Record of the Twentieth IEEE

[9] A.E.Kaloyeros and E.Eisenbraun *Ultrathin diffusion barriers/Liners for gigascale copper metallization*,2000

[10] Von Seefeld, H. Cheung, N.W. Maenpaa, M.Nicolet *Investigation of titanium-nitride layers for solar-cell contacts*, Electron Devices, IEEE Transactions on, Volume 27, Issue 4

[11] Holloway K, Fryer PM, Cabral C, Harper JM, Bailey PJ, Kelleher K.H., 1992, J.Appl.Physics 71(11):5433-43

[12] Uh CK, Chang S, Lewis JE. 1986 IEEE VMIC Proc.1986:181

[13] H.Lu, S.Ding, G.Ru, Y.Jiang, X.Qu *Investigation of Co/TaN bilayer as Cu diffusion barrier*

[14] H.Yan, Y.Y.Tay, Y.Jiang, N.Yantara, J.Pan, M.H.Liang, Z.Chen *Copper diffusion barrier performance of amorphous Ta-Ni thin films*, Applied Surface Science, 258(2012) 3158-3162

[15] C.Lee, T.Huang, S.Lu *Diffusion barrier properties of electroless Ni for electroless Cu using Cu plating employing hypophosphite as a reduction agent*, Journal of material science:materials in electronics 9(1998) 337-346

[16] Q.Xie, Y.Jiang, C.Detarvienier, R.L. Van Maierhaeghe, S.Qu *Tungsten carbides as a diffusion barrier for Cu metallization*

[17] D.Deduytsche, C.Detavernier, R.L.Van Meirhaeghe, J.Appl.Phys. 98(3)033526(2005)

[18] H.Yan, Y.Y.Tay, Y.Jiang, N.Yantara, J.Pan M.H.Liang Z.Chen *Copper diffusion barrier performance of amorphous Ta-Ni thin films*, 2011

[19] B.Zhao, K. Sun, Z. Song, J. Yang *Ultrathin Mo/MoN bilayer nanostructure for diffusion barrier application of advanced Cu metallization*, 2010

[20] E.Fred Schubert *Light Emitting Diodes, Chapter 2*, 2003

[21] M.Yli-Koski *Optical activation of copper in silicon studied by carrier lifetime measurements*, 2004

[22] F.P.Giles, R.J. Schwartz *Computational separation of bulk and surface recombination using contactless photoconductive decay*, 1996

[23] T.Roth, *Analysis of electrically active defects in silicon for solar cells*, Doctoral thesis, 2008

[24] S.W. Glunz, S.Rein, J.Y.Lee and W.Warta *Minority carrier lifetime degradation in boron-doped Czochralski silicon*, 2001

[25] B.Lim, K.Bothe, J.Schmidt *Deactivation of the boron-oxygen recombination center in silicon by illumination at elevated temperature*, 2008

[26] H.Savin, M.Yli-Koski, A.Haarahiltunen *Role of copper in light induced minority-carrier lifetime degradation of silicon*, Helsinki University of technology, Appl.Phys.Lett. 95, 152111, 2009

[27] M.Yli-Koski, V.Vainola, A.Haarahiltunen, J.Storgards, E.Saarnilehto and J.Sinkkonen *Light activated copper defects in p-type silicon studied by PCD*, 2003

[28] R.Sachdeva, A.A.Istratov, E.R.Weber *Recombination activity of copper in silicon*, 2001

[29] J.Schmidt and R.Hezel *Light-induced degradation in Cz silicon solar cells: fundamental understanding and strategies for its avoidance*, 2002

[30] A.Herguth, G.Schubert, M.Kaes, G.Hahn *A new approach to prevent the negative impact of the metastable defect in boron doped Cz silicon solar cells*, 2006

[31] K.Matsunaga, T.Tamaka, T.Yamamoto *First-principles calculations of intrinsic defects in* Al_2O_3, 2003

[32] B.Hoex, J.Schmidt, M.C.M.van de Sanden, W.M.M. Kessels *Crystalline silicon surface passivation by the negative-charge dielectric* Al_2O_3, 2006

[33] K.R.Williams *book chapter: Silicon Wet Isotropic Etch Rates page 813, book: Proprieties of Crystalline silicon*, 1998

[34] B.Hoex,J.J.H.Gielis, M.C.M.van de Sanden and W.M.M. Kessels *On the c-Si surface passivation mechanism by the negative-charge-dielectric* Al_2O_3, J. Appl.Phys. 104, 112703, 2008

[35] T.Saitoh, H.Hashigami, S.Rein, S.Glunz *Overview of light induced degradation reasearch on crystalline silicon solar cells*, 2000

[36] Sinton RA, Cuevas A *Contactless determination of currentvoltage characteristics and minority carrier lifetimes in semiconductors from quasi steady-state photoconductance data*, Appl Phys Lett 0885 58 1409D 1401, 2003

[37] R.S.Muller, T.I.Kamins *Device electronics for integrated circuits*, John Wiley & Sons, chapters 1 and 5, 2010

[38] V.V.Voronkov, R.Falster *Latent complexes of interstitial boron and oxygen dimers as a reason for degradation of silicon-based solar cells*, 2010

[39] J. Lindroos, M. Yli-Koski, A. Haarahiltunen, and H. Savin *Room-temperature method for minimizing light-induced degradation in crystalline silicon*, *Applied physics letters*, 2012